FACULTY
OF MATHEMATICS
AND PHYSICS
Charles University

DOCTORAL THESIS

Miroslav Kettner

Reactivity of transition metals – influence of the degree of oxidation of active substrate

Department of Surface and Plasma Science

Supervisor of the doctoral thesis: doc. RNDr. Václav Nehasil, Dr.

Study programme: Physics

Specialization: Physics of Surfaces and Interfaces

Prague 2017

I declare that I carried out this doctoral thesis independently, and only with the cited sources, literature and other professional sources.

I understand that my work relates to the rights and obligations under the Act No. 121/2000 Coll., the Copyright Act, as amended, in particular the fact that the Charles University has the right to conclude a license agreement on the use of this work as a school work pursuant to Section 60 paragraph 1 of the Copyright Act.

In Prague .....

Miroslav Kettner

Acknowledgement

First and foremost, I would like to thank my supervisor, doc. RNDr. Václav Nehasil, Dr. for his guidance, support, help, and his friendship. You have always been at hand whenever I needed it, you have provided me with a counsel whenever I asked for one, and you have offered me enough independence to freely develop my other skills. Thank you.

I would also like to thank to my colleagues RNDr. Tomáš Duchoň, PhD. for being the unattainable idol, Mgr. Klára Ševčíková, PhD. for our endless disputations, Mgr. Peter Kúš for being a tower of strength during the exams, and Mgr. Zdeněk Rafaj, Mgr. Tatiana Kolářová PhD., and Mgr. Petr Homola for creating the friendly and helpful atmosphere in the laboratory. Many thanks also belong to all the other staff and students at the Department of Surface and Plasma Science for their companionship and making our department a stimulating place.

I would like to give my thanks to the experimental staff at the Material Science Beamline at Elettra synchrotron in Trieste, RNDr. Ing. Tomáš Skála, PhD., and Ing. Nataliya Tsud, PhD., and the staff at NAP-XPS in Prague, RNDr. Břetislav Šmíd, PhD., and Mykhailo Vorokhta, PhD. for their enthusiastic help with the measurements.

Special thanks go to Dr. Matthew Wolf and Dr. Jolla Kullgren at the Uppsala University in Sweden for their DFT calculations and for their hospitality during my visit of Uppsala.

Finally, my deepest gratitude is devoted to my family, my wife and my daughter for their support material, physical, and psychical, their patience, and their tolerance.

The work was supported by the Charles University, project GA UK No. 897316.

Název: Vliv oxidačního stupně aktivní podložky na reaktivitu přechodových kovů.

Autor: Miroslav Kettner

Katedra / Ústav: Katedra fyziky povrchů a plazmatu

Vedoucí doktorské práce: doc. RNDr. Václav Nehasil, Dr., Katedra fyziky povrchů a plazmatu

Abstrakt: V práci jsou použity experimentální metody povrchové analýzy ke studiu vlivu fluoru na vlastnosti oxidu ceru. Vrstvy oxidu ceru a fluorem dopovaného oxidu ceru jsou připraveny epitaxním růstem na monokrystalech rhodia. Jejich vlastnosti jsou porovnávány v konfiguraci inverzního katalyzátoru a v neinvertované konfiguraci. Navíc byla popsána metoda umožňující epitaxní růst oxidu ceru (110) na Rh(110). Změny tvaru spektra Ce 3*d* vlivem přítomnosti fluoru ve vrstvě jsou v práci detailně popsány, vysvětleny a je navržen postup pro dekonvoluci změřených spekter. Speciální pozornost je věnována stabilitě fluoru ve vrstvě oxidu ceru. Data ukazují, že obsah fluoru je stabilní při tlaku řádově 100 Pa až do 200°C. Fluor ale způsobuje redukci oxidu ceru, zvětšení mřížové konstanty a tudíž i morfologické změny při růstu oxidu ceru. U čtyř typů vzorků byly popsány rozdíly v kyslíkové kapacitě vrstvy a ve schopnosti oxidovat vodík. Zároveň je v práci popsáno dvojí působení kyslíku. Část fluoru je vlivem kyslíkové expozice vypuzena směrem od povrchu, zatímco zbylá část je vypuzena do adsorpčních pozic na povrchu. Fluor v těchto pozicích má změněnou energetickou strukturu a je náchylný k reakci s atomárním vodíkem. Tato reakce je pravděpodobně zodpovědná za mizení fluoru z vrstvy oxidu ceru.

Klíčová slova: Oxid ceru, rhodium, fluor, kapacita pro uložení kyslíku, odstranění fluoru.

Title: Reactivity of transition metals – influence of the degree of oxidation of active substrate

Author: Miroslav Kettner

Department / Institute: Department of Surface and Plasma Science

Supervisor of the doctoral thesis: doc. RNDr. Václav Nehasil, Dr., Department of Surface and Plasma Science

Abstract: The impacts of fluorine doping of ceria are studied by means of surface science experimental methods. Fluorine-doped and fluorine-free ceria layers are epitaxially grown on rhodium single crystals and their properties are compared in regular and inverse catalyst configurations. A procedure for epitaxial growth of CeO_2(110) and CeOxFy(110) layers on Rh(110) single crystal is developed and described in detail. Shape alterations of Ce 3*d* spectrum brought about by fluorine doping are explained and a suitable deconvolution method is proposed. Special attention is focused towards stability of fluorine in ceria. Presented data show that fluorine incorporation in ceria lattice causes stable reduction of ceria, which withstands up to 200°C in near-ambient pressure conditions. Morphological changes are observed due to elongation of surface lattice constant of reduced ceria. Oxygen storage capacities and hydrogen oxidation reaction rates of four different studied systems are compared and discussed. The twofold nature of oxygen exposure of fluorinated ceria is discovered and explained. Oxygen repels fluorine from the surface, while the remaining part of fluorine is expelled to adsorbate positions, where its electronic state is altered. Moreover, such fluorine is prone to interact with atomic hydrogen. This reaction is put forward as the main fluorine removal mechanism.

Keywords: Ceria, Rhodium, Fluorine, Oxygen Storage Capacity, Fluorine removal

Contents

1. Introduction

1.1. Catalysis of Exhaust Gases

Catalysis in general accompanies mankind for the dominant span of its documented existence. The oldest known usage of a substance which enters a chemical process but is not consumed during the transformation is probably the production of alcohol from sugar – fermentation. The first recorded use of inorganic catalysis from 1552 describes the conversion of alcohol to ether with the help of sulfuric acid [1], [2]. Systematic investigation of the known observations and their classification as catalysis was done by Jöns Jacob Berzelius in 1835. Probably the most important achievement of catalysis is the Haber-Bosch synthesis of ammonia from hydrogen and nitrogen developed in the beginning of 20th century, which serves today mainly for manufacturing of fertilizers.

The following steps in development of catalysis were dominated by the petrochemical industry which implemented the steam reforming reaction and catalytic cracking. With the boom of urbanization and mass expansion of public transportation and vehicular traffic, the need for effective cleaning of exhaust gases became eminent. The situation reached its climax in events like The Great Smog of London, when in winter 1952 the inverse character of weather in combination with heating with low quality coal and a new diesel engine public transportation buses created conditions which caused death of up to 12 thousand people and many others became ill with respiratory problems [3]. Not only lead the smoke to health problems but it also hampered citizen's everyday life. The visibility was around 10 meters, and the smoke penetrated even into buildings; as a result, theater performances were canceled because the spectators could not see the actors on the stage.

To fight the harmful effects of exhaust gases, first steps were made in 1952 in USA, where Eugene J. Houdry submitted the patent for a catalytic converter [4]. Nevertheless, widespread adoption of catalytic converters did not occur until more stringent emission control regulations forced the removal of the anti-knock agent – tetraethyllead from gasoline because lead inactivated the converter by forming a coating on the catalyst's surface [5]. The pioneer in developing of motor vehicle emission standards was California. The established regulations were then adopted at the U.S. federal level, and, later on, taken over also in Europe [6]. Up to these days, stricter regulations are passed every few years, and the whole segment is forced to introduction of zero emission vehicles.

1.2. Cerium Oxide and Rhodium in Catalytic Converters

Soon after the catalytic converters were established in use, it became apparent that the base metals, such as Ni, Cu, Co or Mn, lack the necessary reactivity and durability. The most effective and stable catalysts showed to be the noble metals, Rh, Pt, and Pd [7]. First in use were the so-called dual bed converters, where, in the first bed, the NOx oxides are reduced, and, in the second bed, the hydrocarbons and CO are oxidized. However, the stricter regulations for the NOx content forced the development of a single bed catalyst, which would catalyze all the reactions simultaneously. This so-called three-way catalyst needed also a feedback control system that would stabilize the air-to-fuel ratio. In order to reduce the air-fuel ratio

perturbations, cerium oxide, also known as ceria, was found to be an ideal substrate which is able to provide or store oxygen in dependence on the outer oxygen lean or rich conditions, respectively. This phenomenon or its degree is known under the term oxygen storage capacity (OSC). Cerium oxide should also increase thermal stability of the support and promote noble metal dispersion [8], [9].

Decrease in OSC of catalytic converters is often connected with the term ageing, which describes detrimental effects caused mainly by thermal instability, sintering of active metals and the oxide support, and porosity loses [8], [10]. Further improvement of commercially used catalytic converters was achieved by mixing ceria substrates with other oxides, such as ZrO_2 [8], [11], La_2O_3 [12], [13], or Al_2O_3 [10], [12], [14], which create irregularities in the structure of ceria, and thus increase its OSC and improve its thermal stability. The most advanced catalytic converters contain also traces of BaO, NiO, PrOx or TiO_2 which help to maintain the catalytic activity for a longer time and enhance the NOx removal [12], [15]–[17].

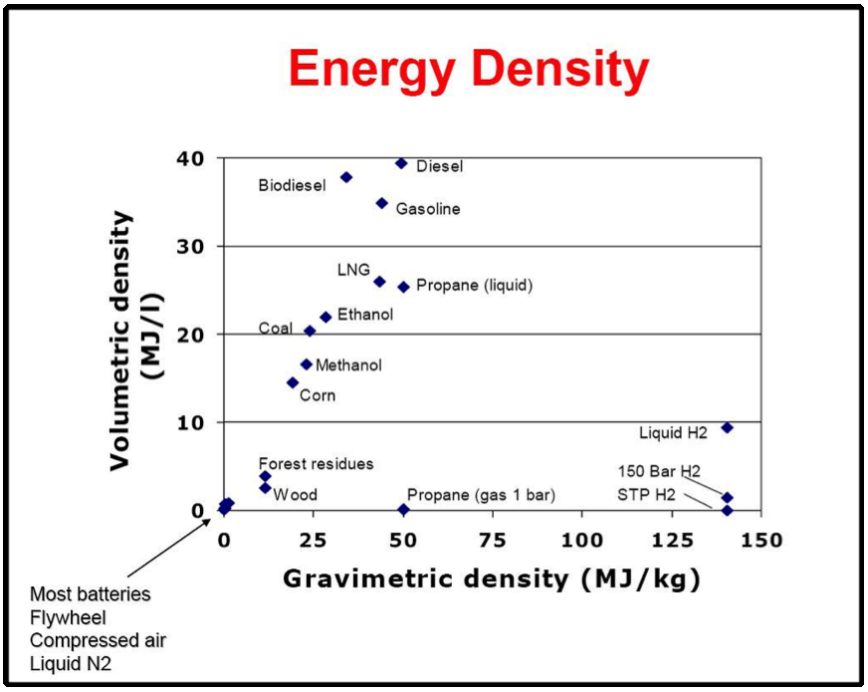

Figure 1: Energy density in different energy storage materials. Taken from [18].

It is clear that even with the recent rapid development in design of catalytic converters, Rh and ceria still remain the basic functional components. Even though alternative power sources for vehicular transportation such as fuel cells or batteries are being investigated, such technologies still lack the needed power storage efficiency (see Figure 1). For this reason, gasoline and diesel still remain the most commonly used fuels for vehicular transportation, and, especially in the poorer countries, these propellants will not be replaced for decades. Therefore, the understanding of the basic mechanisms of oxygen spillover and oxidation reactions on the interface of rhodium and ceria still remains a point of interest.

1.3. Cerium Oxide and Rhodium in Model Catalysis

Rhodium and its interaction with gases, such as oxygen or carbon monoxide has been widely studied in the past [19], [20]. CO on Rh(111) adsorbs first into the more

stable on top positions [21]. At room temperature and full saturation, CO occupies as 0.75 ML (2 × 2)-3CO two different positions – top and 3-fold hollow, which could be easily differentiated in O 1*s* and C 1*s* spectra in X-ray Photoelectron Spectroscopy (XPS) [22], [23]. On the other hand, O_2 dissociates upon interaction with Rh(111) [24] and, at room temperature, creates a stable (2 × 1) 0.5 ML coverage, in which the oxygen resides only in the 3-fold hollow sites [25], [26]. It is then clear that during the oxidation reaction of CO on Rh(111), at least a part of the 3-fold hollow adsorption positions must remain free of CO, in order to O_2 was able to dissociate [24].

In the case of Rh(110), CO forms a 0.5 ML p2mg(2 × 1)-2CO layer [27]. Similar 0.5 ML p2mg(2 × 1)-2O structure is formed by dissociated oxygen upon oxygen exposure of Rh(110) [28], [29].

Disputations have been lead about the extent of CO dissociation on Rh [24], [30], [31]. Nevertheless, it has been shown that the activation barrier for CO dissociation is structural, as well as size sensitive [32]. Especially for deposited Rh particles, CO dissociation should be present to some extent due to the large number of defects at the particles.

The attributes of ceria were also thoroughly examined in the past, especially with focus on the OSC capabilities and peculiar shapes of its XPS spectra. The basic working principle behind the OSC of ceria is its reduction to Ce^{3+} and facile reoxidation to Ce^{4+} [33], [34]. This ability of ceria seems to be also structurally and size sensitive [35]–[37]. In the case of (111) ordered ceria layers, the emerged oxygen vacancies tend to order into regular patterns with ($\sqrt{7} \times \sqrt{7}$)R19.1°, (3 × 3), and (4 × 4) structures [38], [39].

There were many attempts to describe and explain the obscure shapes of the reported XPS spectra of Ce. For the characterization purposes, the distinct shapes of Ce 3*d* attracted more interest, and therefore, more effort was put into elucidation of its multiplet appearance. The earliest explanation by Kotani et al. used the semi-empirical model which was largely accepted and adopted throughout the spectroscopic community [40], [41]. Unfortunately, this method used over-simplified charge transfer model, which was based on the principle of mixed valence initial state and adjusted to fit to the experimental results [42]. Only recently this semi-empirical approach was challenged by Bagus et al., who used rigorous *ab initio* theoretical treatment [43], [44]. Besides that, the theory of mixed valence initial state for CeO_2 was doubted and substituted by covalent bonding theory whereby Ce^{4+} has no electrons at the 4*f* level in its ground state [45], [46].

The behavior of ceria in combination with transition metals could be studied either from the perspective of so-called inverse catalyst, or in the form of noninverted layout setup. The inverted approach offers more detailed studies of epitaxial growth of ceria on different single crystals, such as Cu(111) [47]–[50], Cu(110) [51], or Rh(111) [52]. Such studies aim for preparation of new defined model surfaces [53]–[55], basic understanding of the interaction between the materials, either from the morphological, or physicochemical point of view. Moreover, the inverse setup involves both materials mainly in the ordered forms, which allows for model studies of orientation specific reactions [56]. Such studies can also exploit and describe the unique properties of the interfacial sites [57], [58], or defect sites, which remain uncovered by any deposited material [59], [60].

One of the most interesting aspects studied with noninverted samples is the strong metal support interaction. Even though the phenomenon standing behind the

decrease in reactivity was explained by encapsulation of deposited material by ceria support [61], [62], the thesis of an electronic effect influencing the reactivity of the metal particles remained in the surface science community under the term electronic metal support interaction (EMSI). EMSI was found responsible for influencing of the reactivity of deposited metal particles by charge transfer between the particles and the support [63]–[66].

Other works studied the basic principles of the OSC and beneficial effects of combining platinum group metals with ceria. New term 'spillover' emerged standing for oxygen migration from the particles into the support [67], and its counterpart, back-spillover or reverse spillover, which stand for oxygen migration from the oxygen support onto the metal particles [68], [69]. These phenomena are considered responsible for the enhanced catalytic activity of combined rare metal-ceria systems, and reverse spillover was even found to be influenced by the ordering of the oxide support [70].

1.4. Fluorine in Ceria

Fluorine contamination of ceria is quite a common phenomenon. In literature, there are described cases of contaminated ceria single crystals by fluorine [71], [72]. Especially, the surface layers were found to have the highest fluorine concentration. This was ascribed to facile fluorine migration in ceria, which is thermally activated [73], [74]. Therefore, small fluorine contamination of the source material will be most noticeable at the surface of the single crystal, which is the critical part for any surface science studies. This could be also the reason, why ceria single crystals were not available for buying in the last few years. Since the cerium element is obtained from fluorine containing minerals, which have to be separated from fluorine [75], [76], the minimal amount of residual fluorine will tend to migrate through the crystal to its surface [71], [72].

Nevertheless, fluorine can contaminate ceria from outer sources, too. In our case, some of the improperly stored cerium source material has been contaminated most probably from the Teflon sealing of scroll pump, which, during the scroll pump's operation, are being abraded and penetrate even into the pumped area. Other sources could be the fluorine containing support [73], [74], [77] or fluorine gas [78]. Due to its high electronegativity, fluorine promptly reacts with ceria substituting for oxygen in the fcc lattice. The cubic crystal structure is reported even for CeOF, which is a stable compound in a wide range of fluorine concentrations [79], [80]. However, fluorine concentration too high leads to structural change to hexagonal lattice [78]. Upon exposure of CeF_3 with anhydrous HF, it is even possible to create CeF_4 compound [81].

From the application point of view, the ability of ceria to bond with fluorine is employed for fluorine removal from wastewater [82]. Other promotional aspects of fluorine are described by Zhang et al., who report improved reduction of NO caused by presence of fluorine in CeO_2-TiO_2 catalyst [83]. Ceria was also successfully employed in proton exchange membrane fuel cell (PEMFC) technology [77], [84], [85]; however, fluorine contamination from the Nafion membrane is not a rare event [77], [86].

Even though there are some reports about the interaction of fluorine with ceria, very little is known about the potential beneficial or detrimental effects of fluorine doping of ceria on three-way catalysis (TWC) reactions or hydrogen splitting reactions in PEMFC. Focused research of this topic is therefore of interest.

1.5. The Scope

The aim of this work is to explore the means of fluorine doping of ceria as a tool for permanent change of its oxidation state, investigate the consequences and changes induced by controlled fluorine doping, and compare the reactivity of prepared samples in dependence on the oxidation state of the substrate, which is altered by the presence of fluorine. The goal is to understand the mechanisms of fluorine incorporation in ceria and describe the electronic, chemical, and morphological changes caused by fluorine presence in cerium oxide. Moreover, the objective is also to study the stability of fluorine in ceria at various conditions. The ultimate target is to analyze the reactivity of transition metals (such as Rh, Pt, or Pd) in dependence on fluorine content in ceria substrate and describe any potential differences in reaction mechanisms.

2. Experimental

2.1. X-ray Photoelectron Spectroscopy (XPS)

X-ray Photoelectron Spectroscopy, also known as Electron Spectroscopy for Chemical Analysis (ESCA), is a basic characterization method in surface science. Its function principle is based on photoemission effect described by A. Einstein in 1905 [87], for which he was awarded a Nobel prize in 1921 [88].

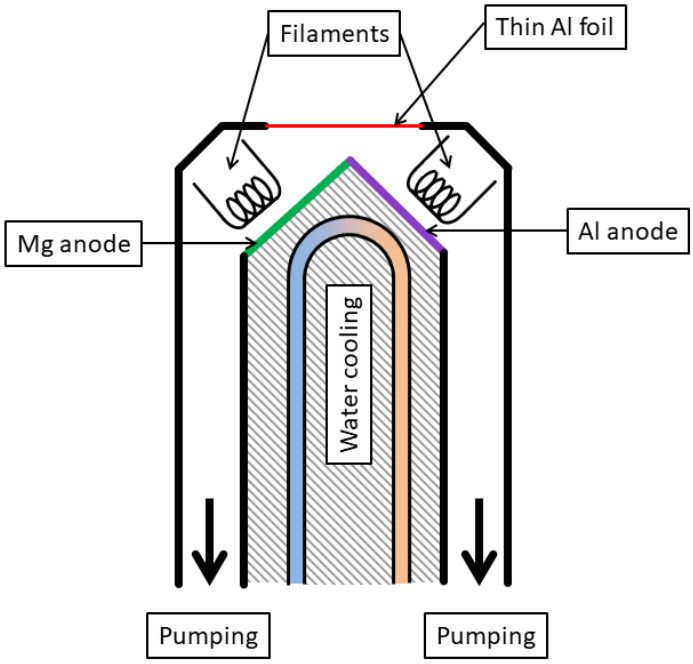

Figure 2: Schematic of a dual Mg/Al X-ray source.

The method consists of three critical components, the X-ray source, the electron energy analyzer, and the detector with appropriate signal counting electronics. The draft of a common laboratory Mg/Al X-ray source is in Figure 2. Filaments emit electrons which are accelerated towards their respective anodes. The impact of 10-15 keV electrons brings about emission of X-rays. The choice of the anode material should reflect the use for surface science analysis. Moreover, the material should be metallic and have a reasonably high melting point because 12 kV and 20 mA of emission current create 240 W of heat applied on approximately 1 cm^2. The frequency f of the emitted light in dependence on anode material is described by Moseley's law:

$$\sqrt{f} = k_1(Z - k_2), \tag{1}$$

where Z is the atomic number of the anode element, and k_1 and k_2 are constants which depend on the transition in the material. For the most energetic K_α line, we get $k_2 = 1$ and:

$$k_1 = \frac{R}{(1+\frac{m_e}{M})}\left(\frac{1}{1^2} - \frac{1}{2^2}\right), \tag{2}$$

where R is the Rydberg constant, m_e is the electron mass, and M is the total mass of the nucleus. It is clear that the frequency of the emitted light depends mainly on Z^2. For this reason, the most common anode materials are Mg and Al, and then also Zr, Ag, Ti, or Cr; however, the Zr and Ag anodes use the L_α transition. In order to suppress the intensities of other lines, the setup contains the thin Al window, which

effectively filters the generated X-rays of the additional $K_{\alpha 3,4,5,6}$ and K_{β} lines. The relative intensities and the energy separations of the most important satellite lines for the Al and Mg anodes are listed in Table 1.

Line	Energy (FWHM) [eV]	Energy separation [eV]	Relative intensity
Mg $K\alpha_{1,2}$	1253.6 (0.7)	-	100
Mg $K\alpha'$	1249.1	4.5	1.0
Mg $K\alpha_3$	1245.2	8.4	9.2
Mg $K\alpha_4$	1243.6	10.0	5.1
Mg $K\alpha_5$	1236.3	17.3	0.8
Mg $K\alpha_6$	1233.1	20.5	0.5
Mg $K\beta$	1205.6	48.0	2.0
Al $K\alpha_{1,2}$	1486.6 (0.85)	-	100
Al $K\alpha'$	1481	5.6	1.0
Al $K\alpha_3$	1477	9.6	7.8
Al $K\alpha_4$	1475.1	11.5	3.3
Al $K\alpha_5$	1466.8	19.8	0.4
Al $K\alpha_6$	1463.2	23.4	0.3
Al $K\beta$	1416.6	70.0	2.0

Table 1: Energies, full widths at half maximum (FWHM), energy separations, and relative intensities of the Mg and Al X-ray anodes and their most important satellite lines [89].

The second substantial component of the XPS system setup is the electron energy analyzer. The electrons emitted from the sample have to be differentiated according to their kinetic energies. Schematic of a hemispherical analyzer is shown in Figure 3. In order to filter other electron energies than E_0, the hemispheres are charged to maintain a potential difference:

$$V_1 - V_2 = \frac{E_0}{e}\left(\frac{R_2}{R_1} - \frac{R_1}{R_2}\right), \tag{3}$$

where E_0 is the electron pass energy, e is the elementary charge, R_1 and R_2 are the radii of the inner and outer hemispheres, respectively, and V_1 and V_2 are the potentials applied to the inner and the outer hemisphere. The analyzer allows two modes of measurement. The Fixed Retard Ratio (FRR) also known as Constant Retard Ratio (CRR) mode keeps the ratio E_k / E_0 constant, where E_k is the kinetic energy of the measured electron. The other and in praxis dominantly used mode is the Fixed Analyzer Transition (FAT) or Constant Analyzer Energy (CAE) mode. In this mode, all the electrons are retarded to the same pass energy. While the first mode is typically used for Auger electron spectroscopy because it reduces the high background at low kinetic energies, the CAE mode is generally used for XPS because the resolution is maintained in this way for all detected spectra.

The third necessary part of XPS is the detector. The signal detection system consists of two parts, a multiplier and a detector itself. Multipliers are made of materials with a high coefficient of secondary emission. They are attached to high voltage source, which generates an accelerating potential along the path of the multiplier. Multipliers can have form of single channels usually stacked next to each other to improve the signal/noise output by registering also the electrons with energies $E \pm \Delta E$, or it can have form of a plate with many microscopic channels. Typically, the gain of a multiplier is between 10^6 and 10^8. When the electron spray hits the detector, it induces a detectable current, which is registered by the detector.

One of the important parameters of the detection system is its death time, which is the minimum time between two separate counts to be detected. For count rates too high, the detector could be exposed to continuous stream of electron, which will be registered as a one count.

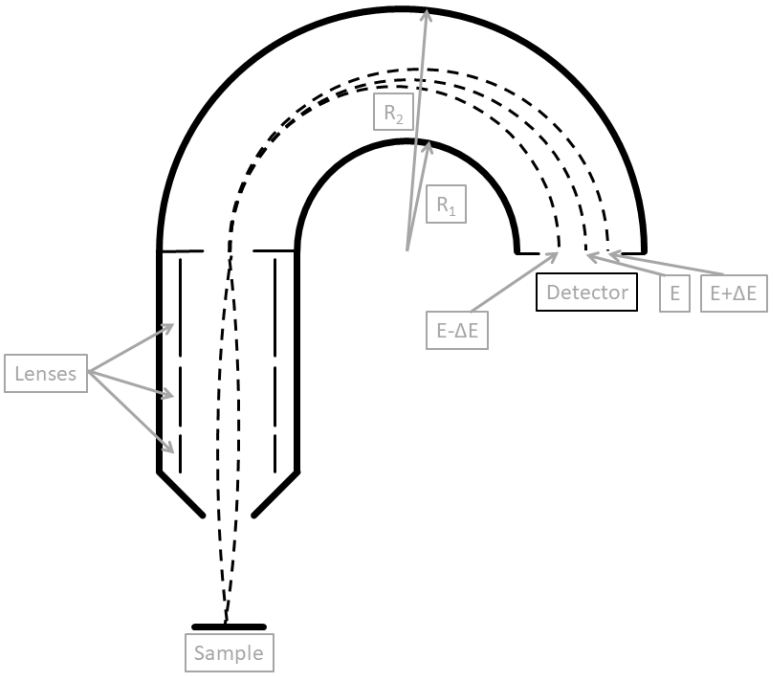

Figure 3: Schematics of hemispherical electron energy analyzer.

The energy of the detected electron could be then traced back to retrieve the kinetic energy of the incident electrons. With knowledge of the energy of the X-ray line, we are able to calculate the electron's respective binding energy E_b according to:

$$E_b = h\nu - E_k - W_A, \tag{4}$$

where $h\nu$ is the energy of the incident light, and W_A is the work function of material of the analyzer. Although the kinetic energy of the electron in vacuum could be described as:

$$E_{k-el} = h\nu - E_b - W, \tag{5}$$

where W is the work function of the sample, due to the fact that both, the sample and the analyzer, are grounded, the contact potential between the two metals accelerates or decelerates the electron, so that $E_k - W_A = E_{k\text{-}el} - W$ in the end.

One of the aspects why XPS is so valued is its capability to determine not only the element composition in the sample, but also the chemical state (oxidation state) of the given element. This follows from the fact that the binding energy could be separated into its components:

$$E_b = -\varepsilon_k - \Delta\varepsilon_R - \Delta\varepsilon_{corr} - \Delta\varepsilon_{rel}, \tag{6}$$

where ε_k is the orbital energy of the electron, $\Delta\varepsilon_R$ is the relaxation energy, $\Delta\varepsilon_{corr}$ is correlation energy, and $\Delta\varepsilon_{rel}$ is the relativistic correction. It is the change in relaxation energy, which causes the energy shifts in dependence on the oxidation state of the given element.

Now it is possible to explain the most common things one can observe during measurement of the photoelectron spectra. The position of a selected photoelectron line depends on the oxidation state of the element. However, especially for the oxide samples, the condition for having the sample grounded may not be met. Then, the so-called charge shift of the peaks is observed. At lower binding energies of a peak,

there are the satellite peaks caused by irradiation with the non-monochromatic source. Actually, one can observe also the presence of the 'ghost peaks', which are brought about by the imperfections in construction of the X-ray source. These peaks come either from electrons emitted by one filament hitting the surface of the other anode (for instance the Mg filament electrons hitting the Al anode – see Figure 2 for clarity), or from oxidation or degradation of the anode surface. So, there could be peaks emerging by excitation with energy 524.9 eV – O K_α or 929.7 eV – Cu L_α. Next kind of peaks is the so-called Auger peaks, which emerge from the situation, when an inner level hole is refilled by an electron from the outer level. This energy is then used for emission of another electron from the outer energy level. In addition, one can notice the background growth at higher binding energies of each excited level, and, especially after some intense peaks, there are peaks coming from specific plasmon loses. Both these phenomena are caused by electrons, which suffered an energetic loss during their travel from the measured material to vacuum.

The surface sensitivity of the XPS is therefore enforced by the inability of the electrons from deeper layer to pass through the material to vacuum. The intensity of a signal which had to travel through the material of thickness d is then:

$$I_d = I_0 \cdot e^{-d \cdot cos\theta / \lambda(E_k)}, \tag{7}$$

where I_0 is the initial intensity of excited electrons, θ is the detection angle with respect to the sample normal, and λ is the Inelastic Mean Free Path (IMFP). The IMFP depends on the kinetic energy of the electron, so it is possible to choose the target scanning depth by proper choice of energy of primary light. The harder the X-rays are, the deeper the signal can arise. The second possibility is tilting the sample, so as to increase the detection angle. The IMFP is usually calculated by the TPP-2M equation [90]. When the IMFP in a material is known, equation (7) can be used for determination of thickness of the deposited layer.

In examination of the obtained spectra, qualitative analysis is usually done by comparing the measured photoelectron lines with reference, such as Handbook of X-ray Photoelectron Spectroscopy [91]. Concerning the quantitative analysis in XPS, there are several different methods. The most common method makes use of the empirically derived sensitivity factors, which evaluate the relative intensities of the most intensive photoelectron lines of the detected elements [92]. The concentration of a given element X in a homogenous sample is then:

$$C_X = \frac{I_X/S_X}{\sum I/S}, \tag{8}$$

where I_X is the intensity of the element X, S_X is the sensitivity factor for the measured line of the element X, and $\sum I/S$ is the sum of normalized intensities of all the detected elements.

For appropriate determination of the intensity from the spectrum, the background should be subtracted from the spectrum. There are several background removal methods which are compared in ref. [93]. Even though the Tougaard's background subtraction is found as the most precise, its necessity to measure broad spectra windows makes the other background removal methods – linear or Shirley's – prevailing.

2.2. Synchrotron Radiation Photoelectron Spectroscopy (SRPES)

Synchrotron Radiation Photoelectron Spectroscopy (SRPES) needs for its function a large synchrotron facility which provides a beamline with light with energies ranging from ~ 10 eV to ~ 1000 eV. However, the light is not

monochromatic, so the experimental setup has to involve a monochromator and a pair of slits to restrict the size of the incident beam. Because the intensity of the incident beam depends on the energy stored in the main ring, which may not be stable, it is an advantage to have the beamline equipped with a device measuring the intensity of the incident light.

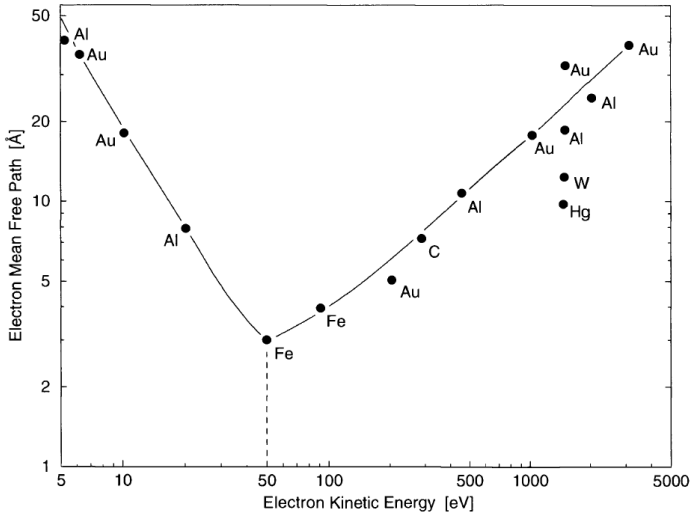

Figure 4: Electron mean free path as a function of their energy in various metals. Taken from [94].

The advantage of measuring with SRPES is its tunability, i.e. ability to choose the frequency of the photons. In this way, it is possible to obtain the most surface sensitive data in combination with high photoionization cross-section [95]. The dependence of IMFP on kinetic energy of an electron in several metals is plotted in Figure 4. The minimal IMFP is usually obtained for energies 50-100 eV [96]. The signal from deeper layers of the sample could be obtained, according to Figure 4, either by using lower or higher kinetic energies than ≈ 50 eV. Nevertheless, by tuning the source to energy a few tens electronvolts above the measured line, we can observe variations in peak intensity caused by the structure of unoccupied levels in which we excite the electrons into. Thus, in order to obtain signal from deeper layers, higher kinetic energies are usually used.

Second advantage of synchrotron sources is its high photon flux in comparison with laboratory X-ray sources. In combination with highly focused spot, polarization of the photons, and ability to produce extremely short pulses, it makes SRPES highly popular and coveted method.

2.3. Resonant Photoelectron Spectroscopy (RPES)

Resonant Photoelectron Spectroscopy (RPES) is a technique, which allows increasing intensity of a peak by resonance enhancement of the direct photoemission with Auger emission channel. The method is usually applied to enhance intensity of weak photoelectron lines in valence band which correspond to incompletely filled electron levels. By tuning the light source to resonant energy, the population of the investigated level is increased by filling the empty states with excited electrons from deeper electron level. Moreover, when the hole is refilled by deexcitation process involving electron from the investigated level, the signal intensity is increased by interfering with the Auger CVV emission channel [94].

The method was frequently used for precise evaluation of the oxidation state of ceria. In Figure 5, there are the principal mechanisms for the Ce 4*d* → Ce 4*f* RPES enhancement of signal from Ce^{3+} and Ce^{4+}. It is obvious that the mechanism of Ce^{4+} enhancement in ceria involves also the O 2*p* levels. It has been shown that such signal amplification is likely to be influenced by perturbations in the lattice, and that such enhancement is much more sensitive to polarization of the incident light [45]. Still, this method can provide unique results inaccessible by other spectroscopic techniques.

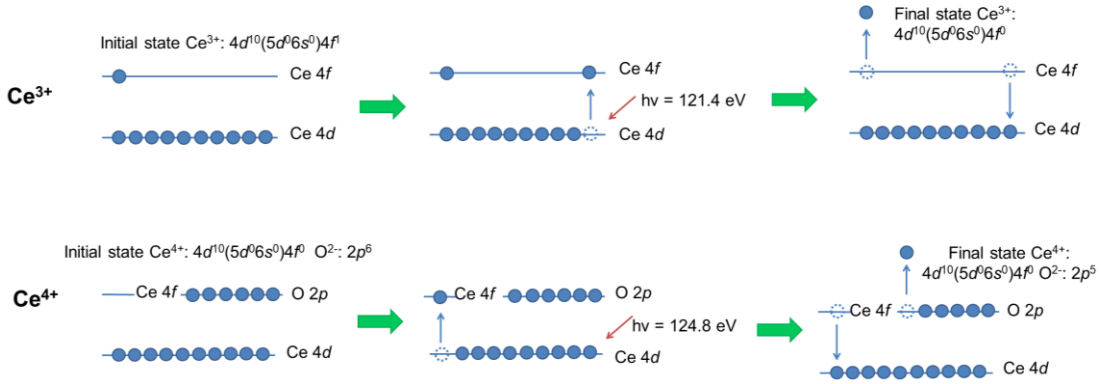

Figure 5: Ce 4*d* → Ce 4*f* RPES mechanisms for Ce^{3+} and Ce^{4+} in ceria.

2.4. Near-Ambient Pressure XPS (NAP-XPS)

The Near-Ambient Pressure XPS (NAP-XPS) method is designed to partially overcome the so-called pressure gap in surface science. The pressure gap refers to the fact that whereas heterogeneous catalysis usually takes place in pressure ranges 1-200 bars, the surface science experiments are performed in ultrahigh vacuum (UHV) conditions. In NAP-XPS system, the sample is exposed to high pressures in the order of millibars, while it is placed very close to a massively pumped nozzle which brings photoelectrons quickly to UHV environment, where they are separated and detected by differentially pumped XPS. Such system has to be also equipped with a special glass window, which allows the outer-generated soft X-ray through into the high pressure section.

In NAP-XPS spectra, we can observe new peaks emerging from the gas-phase. Moreover, it allows us to observe the catalysts in in vivo conditions (during the chemical reactions) by XPS, which is by its nature chemically sensitive. So, unlike the ordinary XPS, NAP-XPS allows the studies of dynamics of catalytic reactions.

2.5. Low Energy Electron Diffraction (LEED)

Low Energy Electron Diffraction (LEED) is commonly used in surface science to check the ordering of single crystal substrates or epitaxially grown model systems. The method is also employed to determine adsorbate reconstructions, or to investigate the exact positions of the adsorbed atoms.

The experimental setup for this method is displayed in Figure 6. The electron gun generates collimated stream of electrons with tunable energies in range 15 – 500 eV. According to wave-particle duality concept, such electrons possess the wavelength λ, which could be (omitting the relativistic correction) expressed from their kinetic energy as:

$$\lambda = \frac{h}{\sqrt{2m_e E_k}}, \tag{9}$$

where m_e is the electron mass. For an electron with energy 100 eV, the wavelength is approximately 1.2 Å, which is of the same order as the interatomic distance. Therefore, the elastically diffracted electrons scatter according to:

$$\sin\theta = \frac{n\lambda}{a}, \tag{10}$$

where θ is the scattering angle, n is the order of diffraction, and a is the lattice constant. The diffracted electrons travel from the grounded sample to the first grid which is also grounded. The second grid, which is sometimes doubled, is adjusted to the potential approximately equal to the energy of the primary electrons. This procedure screens out the inelastically scattered electrons and removes the background from the observed diffractograms. The third grid is grounded and screens out the potential applied on the fluorescent screen. The fluorescent screen is positively charged by 2-6 kV in order to accelerate the electrons and evoke photoluminescence upon their impact. The diffractogram is usually registered by a CCD camera, which is placed either from the sample side – as in Figure 6, or from the backside, behind the fluorescent screen. In either case, the diffractogram is partially obstructed by the sample or by the electron gun.

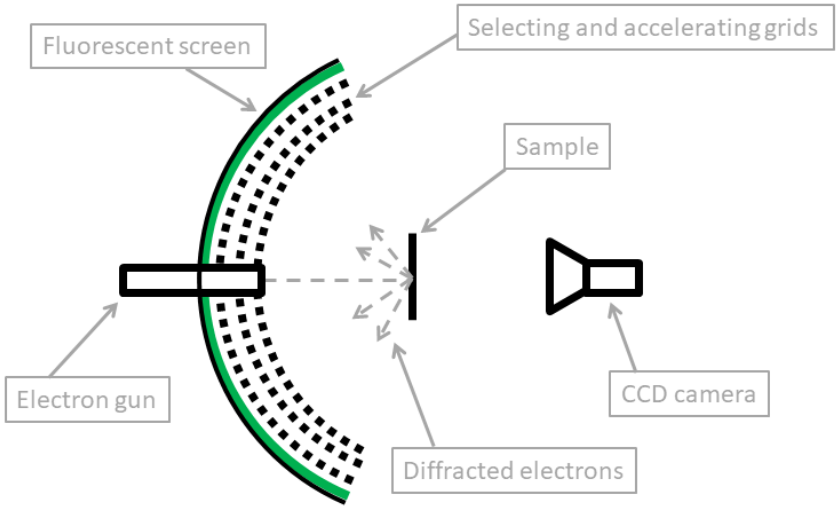

Figure 6: Schematic of LEED system setup.

On the fluorescent screen, the diffracted electrons create a reciprocal pattern, which is related to the direct lattice by equation:

$$\overrightarrow{a^*} = \frac{\vec{b}\times\vec{c}}{\vec{a}\cdot(\vec{b}\times\vec{c})}, \tag{11}$$

where $\overrightarrow{a^*}$ is a vector of the reciprocal lattice, and $\vec{a}$, $\vec{b}$, and $\vec{c}$ are the vectors of the direct lattice. In praxis, the identification of observed pattern is made with a help of programs such as LEEDpat [97].

As follows from the measurement principles, LEED method needs for its functioning good UHV conditions and ordered samples. Its surface sensitivity comes from the range of used electron energies, which have very low IMFP in the studied materials. The useful signal thus comes from the first 1-2 monolayers (ML).

A more sophisticated version, the so-called I-V LEED, is then able to fully determine the atomic surface structure including information about terraces and steps, structure of deeper layers, or presence of contaminants. Such approach needs however comparison with sophisticated calculations which include the dynamic LEED theory.

2.6. Temperature Programmed Reaction (TPR)

The Temperature Programmed Reaction (TPR) method consists in basic of three parts, the Molecular Beams (MB), the temperature-programmable sample holder, and the differentially pumped mass spectrometer. The molecular beams expose the sample with gas molecules, which are either reflected or stick to the surface of the sample. The reflected molecules as well as molecules desorbed from the sample are then separated and detected in mass spectrometer.

The adsorption can be divided to physisorption and chemisorption. While physisorption is present mainly at low temperatures near or below the condensation temperature of the gas, and does not involve chemical bonding with substrate, chemisorption is the main process occurring during the catalytic reactions. The probability of a molecule hitting the surface to stick to the surface is described by a sticking coefficient *s*, which can be calculated from the obtained data as:

$$s(t,T) = \frac{I_m - I(t,T)}{I_m} = \frac{d\theta(t)/dt}{I_m}, \tag{12}$$

where *I(t,T)* is the observed intensity of the molecules in mass spectrometer in time *t*, and I_m is the maximal intensity reached after saturation of the surface, while sample is kept at constant temperature *T*. The sticking probability is dependent on the coverage θ, which changes with continuing adsorption. Naturally, the rate of adsorption r_{ads} depends on the sticking probability according to equation:

$$r_{ads} = s \cdot F = f(\theta) \cdot \exp(-E_{ads}(\theta)/RT) \cdot \frac{p}{\sqrt{2\pi mkT}}, \tag{13}$$

where *F* is the flux of incident molecules, *f(θ)* is some function of the coverage, E_{ads} is the activation energy for adsorption, *R* is molar gas constant, *p* is the partial pressure of the incoming molecules, *m* is the mass of the incoming molecules, and *k* is the Boltzmann constant [98].

The TPR allows also measurements of desorption spectra by linear annealing of the preadsorbed sample in front of the mass spectrometer. This method is called Thermal Desorption Spectroscopy (TDS) or Temperature Programmed Desorption (TPD), and allows the determination of the activation energy of desorption E_{des}, or visualization of different adsorption positions on the surface. As the sample is linearly annealed according to:

$$T(t) = T_0 + \beta t \tag{14}$$

with β being the coefficient of temperature increase with time, the desorption occurs according to Polanyi-Wiener equation:

$$r_{des} = \nu N^x \exp(-E_{des}/RT), \tag{15}$$

where *v* is the preexponential factor, *N* is the surface concentration of adsorbed species, and *x* is the kinetic order of desorption. In order to obtain the preexponential factor and the activation energy of desorption from the experimental data, there are several methods which can be used. Probably the most common and the easiest method to use is the Redhead method [99], whereby, for first order of desorption, the E_{des} is calculated from the temperature of desorption maxima T_m from formula:

$$E_{des} = RT_m \cdot \left(\ln\left(\nu T_m/\beta\right) - 3.46\right) \tag{16}$$

However, this method depends on a guessed preexponential factor, usually chosen as 10^{-13} s^{-1}.

In comparison with other methods [100], the most reliable method should be the Habenschaden-Küppers or also the so-called leading edge method [101]. The activation energy of desorption should be determined from an equation:

$$\frac{d\ln(I(t))}{d(1/T)} = -\frac{E_{des}}{R}, \tag{17}$$

as long as variations of ν and N with T and/or θ may be neglected. Thus, the calculation should be done from high quality data at the leading edge of the desorption peak. The preexponential factor can be estimated from the formula:

$$\nu = \beta({}^{E_{des}}/_{RT})^2 \exp({}^{E_{des}}/_{RT}), \tag{18}$$

which is reliable in case that neither E_{des} nor ν are depended on θ. The best way to ascertain the order of desorption is the 'Arrhenius plot', in which the spectrum is plotted as $ln(I(t)/\theta^x)$ against $1/T$ for various values of x. The plot corresponding to the correct order should be close to a straight line.

In general, the rate of reaction r_{rea} depends on the concentration of both reactants as well as on the activation energy for that reaction E_{rea}:

$$r_{rea} = \nu \cdot \exp({}^{-E_{rea}}/_{RT})[A]^x[B]^y \tag{19}$$

$[A]$ is the concentration of reactant A, $[B]$ is the concentration of reactant B, and x and y are the reaction orders. For the reaction measurements by TPR, there are two approaches. The steady-state reaction, in which the partial pressure of both reactants is kept constant, and we observe changes in production in dependence on the changing temperature. On the other hand, the transition-state reaction method exposes the surface which is preadsorbed with reactant A with the reactant B at stable reaction temperature.

TPR can be also used for other types of measurement. In order to check the continuity of a prepared film, we can expose the sample with an adsorbent, which is able to adsorb at the substrate but which does not interact with the prepared overlayer. The following TDS measurement will reveal discontinuous films or cracked films by showing an observable desorption peak. Other possible utilization of TPR is in measurements of OSC. By integration of the area under the curves, we can calculate all oxygen leaving the surface of the sample, and, in this way, compare the OSC of dissimilar samples.

2.7. Atomic Force Microscopy (AFM)

Atomic Force Microscopy (AFM) is a powerful tool for 3D imaging of surface morphology. Usually, the vertical resolution is below 1 Å, while the lateral resolution reaches approximately 5 nm; however, there are systems capable of obtaining atomic resolution.

The method consists of four crucial components, a laser, a tip on a flexible cantilever, a piezo driven sample holder, and a sectioned photodiode. The principle of operation is as follows. The laser beam is directed to the cantilever, where it reflects. The reflected beam is then detected by a four-sectioned photodiode, which is able to detect the intensity of the beam in every quadrant. As the tip moves on the sample surface, the cantilever tilts, and the laser beam is deflected from the center of the photodiode. The signal on the segments of the photodiode is detected by software which provides a feedback for the piezo elements in the sample holder. In this way, the distance between the sample and the tip is adjusted. Scanning of the morphology proceeds by shifting the sample in x and y directions.

The measurement can be carried out in four different modes, the contact mode, the non-contact mode, the semi-contact mode called also tapping mode, and the peak-force mode.

In contact mode, which can be used only for very flat samples, the z axis or the bend of the cantilever is kept constant. In the first case, the bend of the cantilever provides information about the morphology of the surface; in the second case, the feedback is directly coupled with the change in vertical force applied on the cantilever.

In the non-contact mode, the tip is kept oscillating dozens of nanometers away from the surface, in the attraction force region. The surface morphology is then calculated from the shifts in the resonant frequency of the cantilever, which are caused by a sample-tip interaction.

In the tapping mode, the oscillations of the tip are dozens to hundreds of nanometers, so that it covers both the regions of attractive and repulsive forces between the tip and the surface. The information about morphology then comes from the changes in oscillation amplitude and phase.

The last detection method is the so-called peak-force mode, in which the cantilever is operated well below the resonance frequency with high oscillation amplitudes. Unlike in tapping mode, the z axis movement is done by the sample holder until the desired repulsive force is reached. The morphology is thus gained by following the changes in the z axis movement needed for reaching the repulsive force setpoint.

2.8. Experimental systems

2.8.1. XPS/TPR/LEED Experimental System

The XPS/TPR/LEED experimental system in Prague consists of three separable UHV chambers – the main chamber, the preparation chamber, and a load lock chamber for fast sample exchange. The system reaches a base pressure in range 10^{-8} Pa. The main chamber is pumped with titanium ion pump, which is supported with Ti sublimation pump. The preparation chamber and the load lock chamber are then pumped with turbomolecular pumps, which are pre-pumped with a scroll pump.

The apparatus is further equipped with an Ar^+ sputtering gun, several micro electron bombardment evaporation sources (MEBES) for sample preparation, and a sample holder which allows programmable heating of samples with rate ≈ 1 °C/s up to 700°C or cooling with liquid nitrogen up to -120°C.

The XPS method consists of dual Mg/Al X-Ray source and hemispherical analyzer Omicron EA125 with a five-channel detector. The LEED method is situated in the preparation chamber and consists of PHI 10-120 optics controlled by Perkin-Elmer PHI Model 11 – 020 LEED Electronics System. The diffraction picture is recorded by XC-6AMF camera with Sony Super-HAD II CCD. The TPR method is made up of two separate pipelines which are directed towards the sample. Before exposing the sample, the gases have to pass through two small apertures creating primitive molecular beams. The gas flow is adjusted by precision leak valves and monitored by a Bayard-Alpert ionization gauge in the main chamber. The reflected and desorbed molecules leaving the sample are measured by a differentially pumped quadrupole mass spectrometer (QMS) Leybold Inficon 2000. The experimental configuration of TPR in the XPS/TPR/LEED system is shown in Figure 7. Actual configuration of TPR allows combining up to five different gaseous or two different

liquid substances. On top of that, the method was upgraded by permanent attachment of three isotopically labeled gases, $^{13}C^{16}O$, $^{13}C^{18}O$, and $^{18}O_2$.

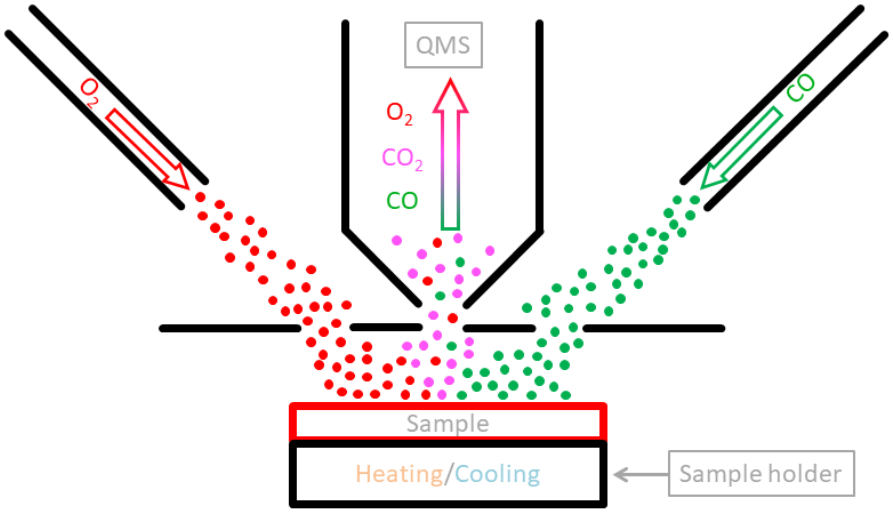

Figure 7: Experimental setup of the TPR method in the XPS/TPR/LEED apparatus.

The XPS/TPR/LEED system was used for a substantial part of the measurements. It has found its use for reference measurements, played an irreplaceable role in UHV reactivity measurements, and served for preparation of samples for the AFM/NAP-XPS measurements.

2.8.2. Material Science Beamline (MSB)

Material science beamline is a part of the synchrotron Elettra facility in Trieste (Italy). The beamline is supplied with radiation from a bending magnet, which provides mostly linearly polarized light in a wide spectrum of spectral lengths. The light is monochromatized in a plane grating monochromator based on a SX-700 design concept [102], which is able to tune continuously in range 22-1000 eV; however, its resolving power as well as intensity are better at lower energies. The normalized photon flux is in range 10^{10} photons/s per 300 mA of accumulated current in the ring for most of the tuned energies. The incoming photocurrent is measured by a gold mesh placed before the UHV chamber.

The end station is made up of two chambers and a fast load lock entry. The UHV system is pumped with turbomolecular pumps, which are supported by a Ti sublimation pump, so the base pressure of the system is around 10^{-8} Pa. The equipment includes a dual Mg/Al X-ray source, hemispherical analyzer Specs Phoibos 150, several MEBES type evaporators, gas inlets with precision leak valves, and a Ar^+ gun. The used manipulator allows azimuthal and polar rotations of the sample, annealing of samples to temperatures higher than 1000 °C or cooling with liquid nitrogen to temperatures as low as -100 °C. This configuration permits measurements of Angle Resolved Ultraviolet Photoelectron Spectroscopy (ARUPS), X-ray Photoelectron Diffraction (XPD), Resonant Photoelectron Spectroscopy (RPES), valence band mappings, or Near Edge X-ray Absorption Fine Structure (NEXAFS). Along with usual XPS, LEED, and SRPES measurement, these methods make MSB beamline highly versatile and practical.

In this work, MSB was used mainly for detailed monitoring of fluorine induced changes in valence band by RPES. We have also made use of the high quality LEED.

2.8.3. Near-Ambient Pressure XPS Experimental System

Near-Ambient Pressure XPS system in Prague is a part of the Ceric research infrastructure. The apparatus is composed of five chambers, load lock chamber, buffer chamber, preparation chamber, analysis chamber, and separable Near-Ambient Pressure (NAP) chamber. The whole system is pumped with several turbomolecular pumps which are pre-pumped with scroll pumps. The schematic of the NAP-XPS apparatus is showed in Figure 8.

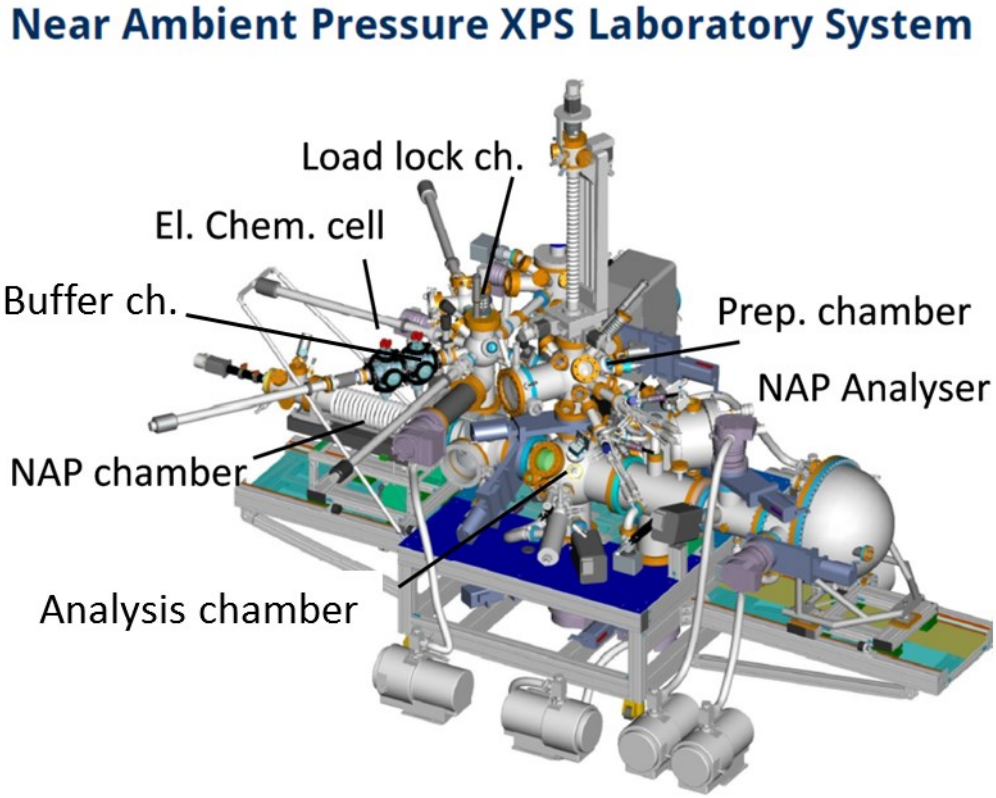

Figure 8: Schematic of the NAP-XPS experimental system. Taken from [103].

The preparation chamber is equipped with LEED, two electron-beam evaporators, gas inlet with a variable leak valve, Ar^+ sputtering gun and a four-axis manipulator, which serves also for transfer of samples into the NAP cell and into the analysis chamber. The manipulator allows also heating or liquid nitrogen cooling in temperature range -170 – 750 °C.

The analysis chamber is equipped with a Al K_α X-ray source with a monochromator, a differentially pumped electron energy analyzer, quadrupole mass spectrometer, and high resolution CCD camera which serves for precision docking and sample positioning in the NAP cell.

The NAP measurements are conducted in the NAP cell which has an Al coated Si_3N_4 window allowing the X-rays in. In the NAP cell, the sample is mounted on a sample holder which allows x,y, and z axes movement and heating/cooling in range -70 – 500 °C. The gases are introduced via two separate tubes. The configuration is able to reach sensible signal intensities up to pressures in low 10^3 Pa range. The flow of the gases can be monitored either automatically via flow meters, or manually via leak valves. During the measurements, the sample is situated very close to the nozzle which allows the photoelectrons through into the analyzer system. The molecules passing through the nozzle orifice are detected by QMS, which is placed behind the

nozzle, near the analyzer. A more detailed description of the NAP-XPS apparatus can be found elsewhere [103].

The NAP-XPS system was used for comparative reactive measurements of model, fluorine-doped and fluorine-free ceria samples. The gas composition was monitored during the measurements and, additionally, reference Rh foil and Al_2O_3 (0001) samples were checked for comparison and calibration of the QMS signal.

3. Results and Discussion

This chapter is sectioned into subsections according to the dealt topic. Each subsection consists of a preface and a main body. Preface provides necessary motivations, goals, and additional information and explains our decisions for the following research. Main body is, in the case of the early work, in the form of a journal article; however, in the case of the latest work, main body is made up of a manuscript or still unpublished results. Due to the chosen form, some, especially technical, details are repeatedly described so as to provide the reader with complete set of information to every subject.

3.1. Influence of Fluorine Dopants on the Shape of Ce 3*d* Spectrum

3.1.1. Preface

The issue of contamination of samples and focused research into properties of such materials can be considered as very sensitive, especially to some research groups. In our group, more or less serious contaminations of ceria with fluorine were repeatedly observed in different UHV systems. Similarly, reports from other groups were published in literature describing various means of contamination. Fluorine can readily migrate into ceria from any fluorine-containing support [73], or, as in the case of ceria single crystals, be an inevitable impurity of the base material, which, unfortunately, tends to accumulate in the surface [71], [72].

Our previous observations suggested that presence of fluorine in ceria manifests itself in the change of shape of the Ce 3*d* spectrum. Even though the complex nature of the Ce 3*d* structure, the individual variations of the shape for undoped ceria are well described [38], [42]. For this reason, the identification of any additional peaks or peculiarities in the shape of ceria is not too daunting or unverifiable task.

The following paper [104], which creates main body of this chapter, shows also a way, in which any Ce 3*d* spectrum of fluorine-doped ceria could be decomposed into its components. This information can be useful for further work with fluorine-doped ceria or for other experimental teams who need to characterize the level of fluorine contamination in ceria. It also gives clear evidence that the nature of a Ce^{3+} atom next to a fluorine dopant and a Ce^{3+} atom next to an oxygen vacancy is completely different.

The last thing tackled in the following lines is the observation of vanishing of fluorine as a result of CO and O_2 gas treatments of the discontinuous samples. In this letter, the diminishing of fluorine was used to confirm the correlation between fluorine in ceria and the emerged Ce-F peaks in Ce 3*d*. However, for any future application of fluorine-doped ceria in industry, the stability of these anion dopants is of interest. Therefore, such question will be more pronounced in further chapters of this thesis.

3.1.2. Introduction

Cerium oxide is well known for its ability to store and release oxygen, which is accompanied by the change of the oxidation state of cerium. This ability is utilized predominantly in catalysis, especially in catalytic converters. Recently, cerium oxide was employed in proton exchange membrane (PEM) fuel cells technology as a

support for active platinum due to its high activity and excellent CO tolerance [77], [85]. The Nafion serves as the proton exchange membrane in these systems. The common aging procedure of the fuel cell includes the loss of fluorine in Nafion, which interacts with the gas. Fluorine is transported towards the outlet, where it accumulates [86]. Fluorine then interacts with cerium oxide and creates cerium oxyfluoride with changed electronic structure and chemical properties compared to pure cerium oxide [73]. These changes are induced by the incorporation of fluorine into the cerium oxide lattice and by the substitution of oxygen atoms in CeO_2 [78]. Further cases of the fluorine contamination of ceria have been recently reported in works of Kullgren et al. and Pieper et al. [71], [72]. They detected the accumulation of fluorine near the surface of the ceria single crystal. Fluorine influenced the chemical properties of the material and hindered the surface oxygen vacancy formation.

In this work, we present the photoelectron study of model thin films of fluorine-doped cerium oxide deposited in discontinuous layers on the Rh (111) substrate. We investigated the influence of fluorine on the Ce 3*d* electron level of cerium. We focus on the characteristic changes in Ce 3*d* spectra originating from the interaction of fluorine and cerium atoms. Used fitting procedure allowed us to distinguish the individual contributions to the final shape of the Ce 3*d* spectrum, and vice versa, we can estimate the influence of fluorine on the shape of the Ce 3*d* spectrum.

3.1.3. Experimental Section

We prepared three CeOxFy/Rh (111) samples, which differ in the thickness of the deposited layer. The samples were prepared by evaporating fluorine-doped cerium in reactive atmosphere of $5 \cdot 10^{-5}$ Pa of O_2 onto the Rh(111) substrate. The Rh(111) single crystal was cleaned by ion sputtering and annealing cycles and, according to XPS, did not contain any carbon contaminants. Prior to insertion into the evaporator, cerium was exposed for 60 minutes to vapors of 20% HF which was annealed to 90°C. Initial fluorine concentration of the prepared, discontinuous CeOxFy layers was estimated using the XPS sensitivity factor analysis [105] to ca. 26%, which corresponds to stoichiometry $CeO_{0.3}F_{0.5}$. The samples were subsequently exposed to small doses of CO and O_2 gases (~ 5 L, 1 Langmuir = 10^{-6} Torr × s) at 150°C and 250°C, respectively, and heated to 500°C. Every step was followed by XPS measurement. Prior to deconvolution of the Ce 3*d* spectra, the satellite peaks were removed by using the Satellite Removal function of the CasaXPS program.

Additionally, we measured the CeF_3 powder (Aldrich Chemistry; 99,99% purity) and several CeO_X/Rh (111) samples, which were prepared as a reference. The oxidized (CeO_2) and reduced (Ce_2O_3) samples were prepared similarly to [52] by evaporating cerium in reactive oxygen atmosphere and under ultrahigh vacuum conditions (10^{-7} Pa), respectively. The thickness of prepared layers was evaluated by combining the Low Energy Electron Diffraction (LEED), Temperature Programmed Desorption (TPD) and X-ray photoelectron spectroscopy (XPS) methods. We define 1 monolayer equivalent (MLE) as the amount of material, at which the LEED pattern from Rh(111) completely disappears and no CO adsorption or desorption can be observed (note that CO adsorbs on Rh but we verified that it does not adsorb on thick CeOxFy or CeOx layers). At depositions lower than 1 MLE, we observe both, the remnants of the Rh(111) LEED pattern and the CO adsorption. The experiments were performed in an UHV, XPS/TPR/LEED apparatus described in detail in section 2.8.1.

3.1.4. Results

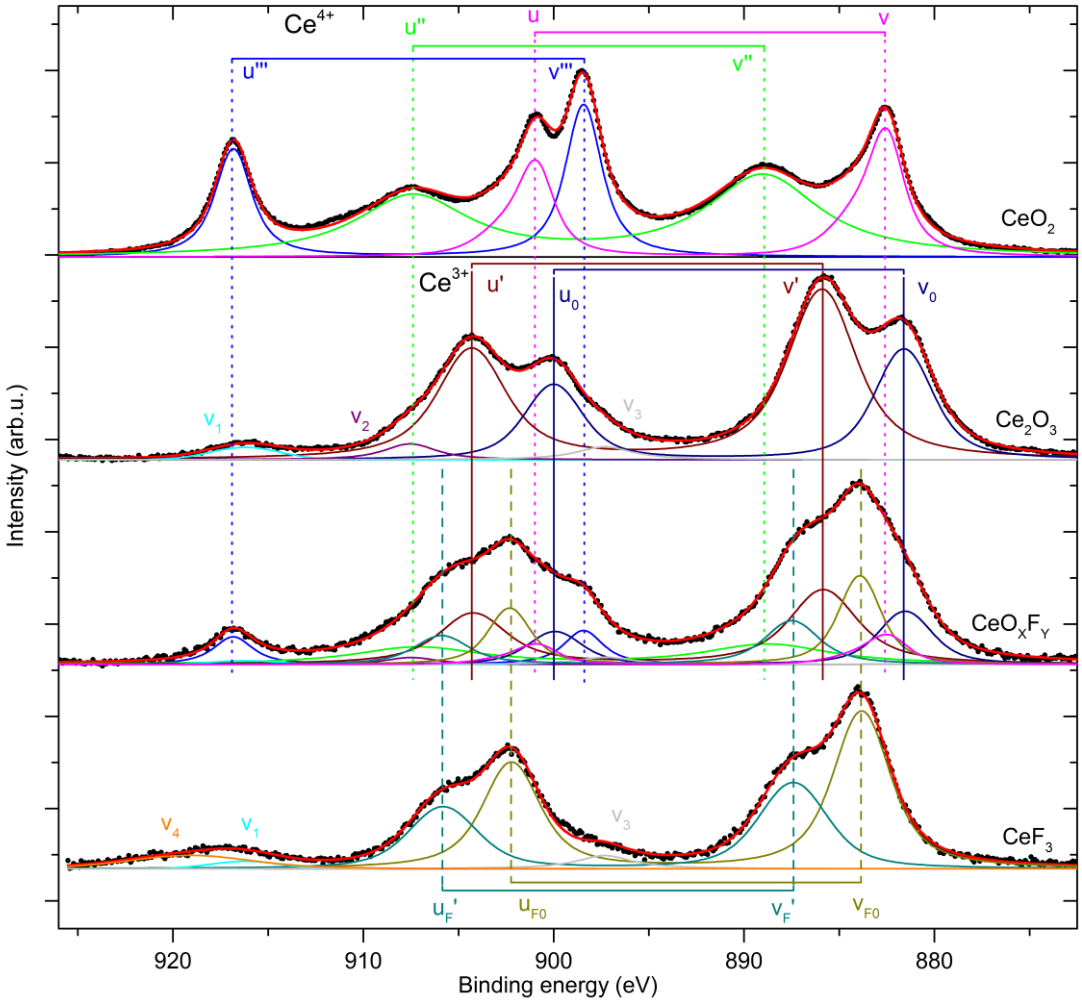

Figure 9: Ce 3*d* spectra of various samples fitted by Voight doublets. From top to bottom – reference CeO_2 spectrum, reference Ce_2O_3 spectrum, fluorine doped CeOxFy spectrum, reference CeF_3 spectrum. The fluorine-free spectra are fitted only by u'''-v''', u''-v'', u-v doublets (CeO_2 spectrum); u'-v', u_0-v_0 doublets and v_1, v_2 and v_3 singlet peaks (Ce_2O_3 spectrum), whereas for a proper fit of the CeOxFy spectrum, we must add the u_{F0}-v_{F0} and u_F'-v_F' doublets. These doublets correspond to the doublets in reference CeF_3 spectrum. The u-v doublet asymmetry is modeled by another u_a-v_a Voight doublet, fixed to former u-v doublet (cf. Table 2). v_4 singlet is probably caused by negligible charging effects of the CeF_3 powder.

Fitting the Ce 3*d* spectra is often used to characterize the state of the sample. The measured spectra are decomposed into individual peaks or doublets according to their origin. To describe the features of the spectra, we use the notation established in [42], where U and V refer to the $3d_{3/2}$ and $3d_{5/2}$ contributions, respectively. Even though the latest theoretical results show that the shape of the Ce 3*d* spectrum is formed by a covalent character of the Ce-O bonding [43], [44], the semi-empirical approach is still very popular [48], [106]. This semi-empirical fitting is based on a simplified charge transfer model proposed by Kotani et al. [40], [107] which suggests a core-hole screening by transfer of 0-2 electrons from ligands to Ce 4*f* states. In the fitting process, the model CeO_2 spectrum is characterized by three

doublets u-v, u''-v'' and u'''-v''', while the model spectrum of Ce_2O_3 is characterized by two doublets, u_0-v_0 and u'-v' (see Figure 9 – CeO_2 and Ce_2O_3 spectra). Both components of the u-v doublet are asymmetric and must be fitted with 2 Voight doublets [108]. The parameters of one of these doublets (further referred as u_a-v_a) are fixed to the parameters of another one (referred as u-v in Table 2).

In the case of CeOx layers, all the Ce 3*d* states with cerium/oxygen ratio 1.5 - 2 can be satisfactorily fitted as a combination of the six mentioned Voight doublets. However, the fit of CeOxFy samples requires the usage of another reference CeF_3 sample. In any case, fitting must obey few rules, which emerge from the natural shapes of the CeO_2 and Ce_2O_3 spectra and eventually from the presence of the fluorine dopant:

(1) Binding energies of the four Ce^{4+} doublets have to be bound together and their splitting must be around 18.4 eV. Identical rules are applied to the two Ce^{3+} doublets.

(2) It's essential to use reference CeO_2 and Ce_2O_3 spectra measured with the same experimental equipment to find the correct binding parameters for the doublets and determine limiting values for other fit parameters, such as Gaussian or Lorentzian widths or Branching ratio. These parameters can differ for various signal intensities or for different samples due to diverse chemical environment. The Gaussian broadening is caused mainly due to incoming X-ray radiation, detection processes and diverse chemical environment of the measured material. The Gaussian width of the constituting doublets thus should not differ significantly within one measurement but can strongly differ on changing the chemical vicinity and signal intensity of measured atoms. On the contrary, the Lorentzian contribution arises from the limited lifetime of the core hole state [109], so the values should be almost constant during the alterations of the chemical composition but its value for the individual doublets can largely differ (compare u''-v'' and u'''-v''' in Table 2). Similarly, the branching ratio parameter should be mainly determined by the value measured in the reference spectrum.

(3) Amplitudes of all three Ce^{4+} doublets as well as amplitudes of the two Ce^{3+} doublets and three singlets have to be kept in a constant ratio. The v_1 and v_3 singlet peaks are present also in the CeF_3 reference sample fit. Their amplitude thus must be unrestricted in case of high Ce-F intensity.

(4) For the background subtraction, the combination of Shirley and linear background is most convenient. Additionally, the measured Ce 3*d* window should be wide enough to fit the background appropriately.

(5) The Ce_2O_3 spectrum has, besides the two u_0-v_0 and u'-v' doublets, three small additional peaks that have to be taken into account. The origin of these peaks (in Table 2 referred as v_1, v_2 and v_3) cannot be satisfactorily explained in terms of the charge transfer fitting model. On the other hand, the v_4 peak observed in CeF_3 reference samples was obviously not present in fits of the thin CeOxFy samples prepared on Rh(111) (see Figure 9 – CeOxFy). Its occurrence could relate to the charging effects of the used CeF_3 reference powder. Therefore, we excluded the v_4 peak from our CeOxFy/Rh (111) fits in order to achieve a better background subtraction.

The measured spectra were fitted according to these principles. In order to obtain the limit values listed in Table 2, we fitted the reference CeO_2, Ce_2O_3 and CeF_3 spectra without any fixing of parameters. The CeOxFy spectra were subsequently fitted with those values and limitations summarized in Table 2. The Ce^{4+} peaks are strictly bound to the u'''-v''' doublet amplitude. Therefore, the u''' peak amplitude

determines the total Ce^{4+} area. This is convenient because during the $CeO_2 \leftrightarrow Ce_2O_3$ transformation, the most distinctive change in spectra shape occurs at the binding energy of 917 eV [38]. That is because the u''' peak does not overlap with any prominent Ce^{3+} peak. Similarly for Ce^{3+} peaks and doublets, their positions and amplitudes are fixed to u'-v' doublet that has the smallest overlap with the Ce^{4+} peaks. The available variations in Lorentzian and Gaussian widths, peak positions and branching ratio parameters were obtained by using the reference spectra for CeO_2, Ce_2O_3, as well as CeF_3. Because the CeOx reference spectra consist mostly of either Ce^{4+} atoms (in case of nearly stoichiometric CeO_2 material) or Ce^{3+} atoms (in case of the most reduced, nearly stoichiometric Ce_2O_3), we fitted the CeOx/Rh(111) reference spectra only with Ce^{4+} or Ce^{3+} peaks, as it is depicted in Figure 9. Similarly, the CeF_3 reference spectrum was fitted with two doublets and all four singlets $v_1 - v_4$. We signed these fluorine doublets as u_{F0}-v_{F0} and u_F'-v_F' to resemble the labeling used in literature [110] and to stress the different origin which comes from the Ce^{3+}-F interaction. According to the fit, the peak v_2 is not present in the CeF_3 spectrum (see Figure 9 – CeF_3) but the other two peaks v_1 and v_3 are distinguishable. Taking into account the covalent bonding character [44] and fact that the u_{F0}-v_{F0} and u_F' v_F' doublets have different binding energies, energy spacing, intensity ratio and Lorentzian widths, we must conclude that these doublet peaks are not related to the u_0-v_0 and u'-v' doublets. Therefore we regard the labeling used in [110] as misleading.

	Ce^{4+}				**Ce-F**	
	u'''-v'''	**u-v**	**u_a-v_a**	**u''-v''**	**u_{F0}-v_{F0}**	**u_F'-v_F'**
Binding energy $3d_{5/2}$ (eV)	898.1-898.6[a]	(u'''-v''')-15.99[b]	(u-v)+1.3 [b]	(u'''-v''')-9.68[b]	883.92-884.52[a]	(u_{F0}-v_{F0})+3.57[b]
Amplitude	free parameter	(u'''-v''')/1.42[b]	(u-v)/2 [b]	(u'''-v''')/0.51[b]	free parameter	(u_{F0}-v_{F0})/1.54[b]
Lorentzian width (eV)	1.62-2.02[a]	1.51-1.91[a]	(u-v)/1.15 [b]	6.8-7.2[a]	1.69-2.09[a]	2.05-2.45[a]
Gaussian width (eV)	1-3[a]	(u'''-v''')/0.65[b]	(u-v)/0.48 [b]	(u'''-v''')/0.44[b]	2.58; 0-5[c]	(u_{F0}-v_{F0})/0.85[b]
Branching ratio	1.23-1.53[a]	1.16-1.46[a]	u-v [b]	1.17-1.47[a]	1.39-1.69[a]	1.22-1.52[a]

	Ce^{3+}					**Ce-F***
	u'-v'	**u_0-v_0**	**v_1**	**v_2**	**v_3**	**v_4***
Binding energy $3d_{5/2}$ (eV)	885.6; 885.3-885.9[c]	(u'-v')-4.3[b]	(u'-v')+30.32[b]	(u'-v')+21.64[b]	(u'-v')+11.43[b]	920-925[a]*
Amplitude	free parameter	(u'-v')/1.94[b]	(u'-v')/18.1[c]	(u'-v')/13.48	(u'-v')/14.38[c]	free parameter*
Lorentzian width (eV)	3.01-3.41[a]	1.89-2.29[a]	0	2.79	3.54	2.77*
Gaussian width (eV)	2.13; 0-6.1[d]	(u'-v')/0.91[b]	4.36	1.23	0	6.13*
Branching ratio	1.39-1.69[a]	1.32-1.62[a]	-	-	-	-

[a]Parameters with values limited to certain range.
[b]Parameter fixed to another parameter.
[c]Parameter value fixed, at first, and then released for more precise fitting. Applied only in case of high Ce-F intensity.
[d]Parameter value fixed, at first, and then partially released (setting a limit to the value range). Applied only in case of high Ce^{3+} intensity.
*Peak observed only on reference CeF_3 powder; Discarded for spectra fits on Rh (111) substrate.

Table 2: The parameters used for the fitting procedure of Ce 3*d* spectra. All doublets have fixed spin-orbit splitting parameter to 18.4 eV.

The degree of CeOx reduction can be estimated by fitting the Ce 3*d* spectrum. The x value in CeOx is calculated using the areas of the fit components according to the equation:

$$x = (Area\ Ce^{4+} / Total\ Ce\ 3d\ area) \cdot 0.5 + 1.5 \quad (20)$$

The wide application of this charge transfer fitting approach lies in its simplicity and in possibility to compare the stoichiometry of different samples. In fact, the percentage amount of Ce^{3+} ions is directly related to the amount of oxygen vacancies in CeOx [38].

The fitting approach which uses only CeO_2 and Ce_2O_3 peaks and doublets to determine the stoichiometry of the samples is insufficient in the case of the CeOxFy spectra. An additional feature at binding energies of 884 eV and 903 eV (see Figure 9 – CeOxFy) can be clearly recognized in all the Ce 3*d* spectra of CeOxFy with high fluorine concentration. Another contribution seems to appear at binding energies 888 eV and 906 eV. Therefore, we added the doublets u_{F0}-v_{F0} and u_F'-v_F' along with a strict boundary conditions to our CeOxFy fits. Even though the boundary conditions are as precise, strict and logically related as possible, the fitting of spectrum with eight doublet and three singlet peaks is a very precarious thing. Nevertheless, we believe that with proper limitations (cf. Table 2), the fitted spectra show a good quality and may serve as the insight into the chemical evolution of the cerium layer.

We emphasize that these u_{F0}-v_{F0} and u_F'-v_F' doublets are characteristic for fluorine-doped samples (no u_{F0}-v_{F0}, u_F'-v_F' doublets were observed on fluorine-free CeOx samples). This Ce 3*d* spectral feature arises from the cerium-fluorine bond and does not seem to be influenced by the cerium-oxygen bonds. The sum of u_{F0}-v_{F0} and u_F'-v_F' areas thus corresponds to the amount of fluorine bonded to cerium atoms in the CeOxFy layer. Actually, this approach is quite similar to Ce^{4+} and Ce^{3+} area comparison, which indicate the number of oxygen vacancies in CeOx [108]. In order to verify the relation of the u_{F0}-v_{F0} and u_F'-v_F' doublets to the concentration of fluorine in the sample, we compared these Ce-F doublet areas with the concentration of fluorine. The concentration was evaluated by the XPS sensitivity factor analysis from the F 1*s* and O 1*s* areas. The Ce-F doublets area and the fluorine concentration for the 0.15 MLE, 0.55 MLE and 0.75 MLE CeOxFy samples are plotted in Figure 10. It is clear that Ce-F doublets area and the fluorine concentration are quantitatively related. In total, we performed over 25 XPS measurements from each sample which determined the fluorine concentration after the preceding sample treatment (gas exposure). We also monitored the changes in Ce 3*d* spectra features, in particular the u_{F0}-v_{F0} and u_F'-v_F' areas. From a statistical evaluation of these more than 80 measurements, we obtained the Pearson's correlation coefficient 0.84. It confirms that the Ce-F doublets correspond to the amount of fluorine in the layer.

The fluctuations of the u_{F0}-v_{F0} and u_F'-v_F' doublets area in Figure 10 (black squares) has two possible explanations. In the first one, we can assign the u_{F0}-v_{F0}, u_F'-v_F' doublets to the Ce-F bonds and the u'-v', u_0-v_0 doublets to Ce^{3+}-O^{2-} bonds. The fluctuations then could be caused by CO and O_2 gas exposures at elevated temperatures which influenced the amount of fluorine atoms substituting oxygen in CeOxFy. According to [78], fluorine can be interstitial in the lattice. Therefore, the fluctuations can correspond to changes in the amount of Ce-F bonds. Under oxygen-rich conditions (after O_2 gas exposure), fluorine will be displaced by oxygen to interstitial position and, under oxygen-lean conditions (after CO gas exposure), fluorine will substitute for oxygen.

Another explanation assigns the u_{F0}-v_{F0}, u_F'-v_F' doublets to the CeF_3 compound and the u'-v', u_0-v_0 doublets to Ce^{3+} in Ce_2O_3 and/or CeOF. According to reference

[73], the CeOF spectra partially resemble the Ce_2O_3 spectra. The fluctuations thus could be caused by the CeOF ↔ CeF_3 chemical changes under oxygen-rich and oxygen-lean conditions respectively. We note that the CeF_3 would have the hexagonal structure in contrast to the cubic structures of CeOF, Ce_2O_3 and CeO_2 [78].

Considering the spectra and the growth of the inhomogeneous CeOF by fluorine migration from CaF_2 in [73] and no signs of hexagonal structure during our LEED measurements, we suggest the first explanation as more probable.

The overall decreasing trend in Figure 10 is obviously identical for both the monitored areas and all the samples. The principle of the cerium oxide reduction is based on migration of oxygen that is released from its lattice position [36], [111], while cerium oxide remains in cubic fluorite-like phase [38]. Similar behavior can be expected for fluorine atoms that are incorporated in the ceria lattice in interstitial positions or substituted for oxygen without any change of structure [78]. Fluorine can also migrate in the CeOxFy [78] or in the CeOx material [73]. It could explain the fluorine concentration decrease during the cyclical exposures of the samples to CO and O_2 gases at elevated temperatures (see Figure 10). Thus, fluorine either dissolves into the Rh(111) substrate or reacts with the incoming gases and subsequently desorbs. In any case, fluorine concentration in the CeOxFy layer decreases after the gas exposures due to fluorine migration in the material.

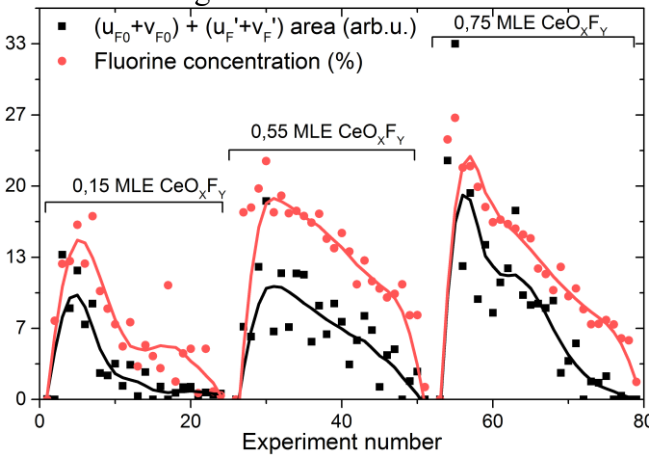

Figure 10: Correlation of the u_{F0}-v_{F0} and u_F'-v_F' doublets area obtained from the fitting procedure of the Ce 3*d* spectra, and the fluorine concentration. The u_{F0}-v_{F0} + u_F'-v_F' intensity corresponds to the amount of fluorine bond to cerium atoms. The amount of fluorine and changes in Ce 3*d* spectral features were monitored by XPS during the preparation of the samples and after the CO and O_2 gas exposures.

The characteristic changes in Ce 3*d* spectra induced by fluorine and corresponding F 1*s* peaks are displayed in Figure 11. It shows the 0.75 MLE CeOxFy/Rh (111) sample during several CO and O_2 exposures and heating cycles. The Ce 3*d* spectra of CeOxFy with higher concentration of fluorine contain prominent peaks at around 884.5 eV (v_{F0}) and 903 eV (u_{F0}). Other fluorine contributions are recognizable at 888 eV (v_F') and 906 eV (u_F'). The overall shape of these CeOxFy spectra with significant fluorine concentration (Figure 11 – (a) and (b)) resembles more the shape of the reduced CeOx rather than the shape of CeO_2. This is caused by substituting O^{2-} with F^- accompanied by cerium reduction from Ce^{4+} to Ce^{3+}. Both the Ce^{3+}-O^{2-} and Ce^{3+}-F^- bonds affect the shape of the spectra. However, this model is very simplified and the charge assignment should not be understood definitely. Upon the gas exposures, fluorine migrates in CeOxFy material

due to the elevated temperature, which enhances the diffusion. During the oxidation cycles, missing fluorine is replaced with O^{2-} and cerium oxidizes back to Ce^{4+}. The shape of the Ce 3*d* spectrum then consists of Ce^{4+} cerium atoms bond to eight O^{2-} ions, which create the typical CeO_2 shape, and the Ce^{3+} atoms, which remain in the F^{-}-Ce^{3+}-O^{2-} state (cf. Figure 9 and Figure 11). The more fluorine atoms are released from CeOxFy, the more cerium is in the Ce^{4+} state and the more the spectral shape resembles the CeO_2 shape.

Notice that the binding energies of the u_{F0}-v_{F0} and u_F'-v_F' doublets in Figure 11 remain constant and do not shift with increasing oxygen concentration. In Figure 11 – (f), the missing depression at 884.5 eV (compare with Figure 9 – CeO_2), which is caused by the presence of residual fluorine, is clearly apparent. This confirms that the nature of u_{F0}-v_{F0}, u_F'-v_F' and u_0-v_0, u'-v' is different and these states remain unchanged in various environments (CeO_2 or Ce_2O_3).

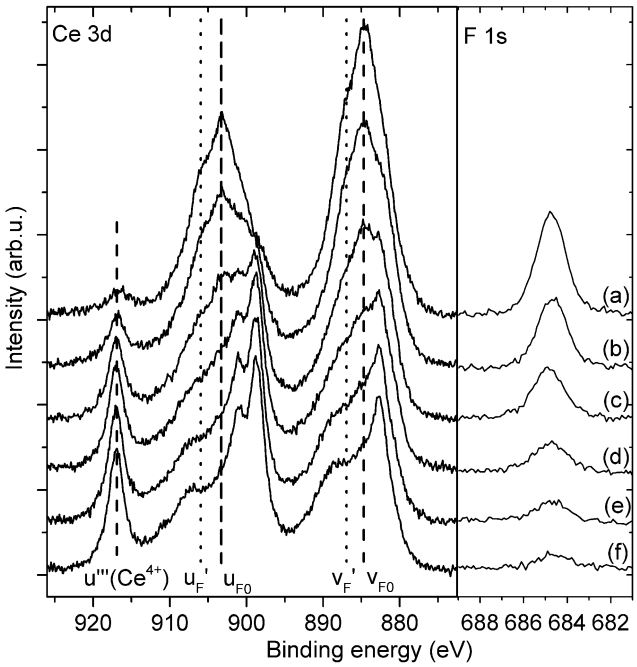

Figure 11: A comparison of Ce 3*d* spectra and corresponding F 1*s* spectra on the 0.75 MLE CeOxFy/Rh(111) sample. Binding energies of approximately 917 eV and 884.5 eV are characteristic for the u''' and v_{F0} peaks respectively, which are the most distinctive features of CeO_2 and CeF_3 spectra shapes. Spectra were obtained after the CO reduction which followed bellow mentioned procedures: (a) sample preparation; (b) three CO and O_2 exposure cycles; (c) four CO and O_2 exposure cycles and one flashing to 500°C; (d) six CO and O_2 exposure cycles and 1 min heating at 500°C; (e) seven CO and O_2 exposure cycles and 3 min heating at 500°C; (f) eight CO and O_2 exposure cycles and 10 min heating at 500°C.

3.1.5. Conclusion

In summary, we have showed that fluorine-cerium interaction influences the shape of the Ce 3*d* spectrum. The u_{F0}-v_{F0} and u_F'-v_F' doublets are characteristic for this Ce-F interaction and the overall Ce-F area correlates with the concentration of fluorine. The origin of u_{F0}-v_{F0}, u_F'-v_F' and u_0-v_0, u'-v' is different and the states do not change even at high oxidation level of the CeO_XF_Y layers. Fluorine substitutes the oxygen atoms or remains in interstitial positions in the CeO_XF_Y. The concentration of fluorine decreases after the exposure to O_2 and CO gases at elevated

temperatures. The released fluorine atoms are gradually replaced by the oxygen ions that come from the O_2 exposures. We introduce the fitting procedure that allows to evaluate the influence and concentration of fluorine in the cerium layer from the shape of the Ce 3*d* spectrum. The research focused on CeO_XF_Y materials can be very useful for PEM fuel cell technology where fluorine from the Nafion proton exchange membrane interacts with cerium oxide-based catalyst and thus, influences its properties.

3.2. Anion Doped CeOxFy/Rh(111) and CeOx/Rh(111) Inverse Catalysts

3.2.1. Preface

The previous chapter showed how the core-hole screening changes in dependence on the vicinity of Ce^{3+} atoms. Moreover, it provided us means to differentiate these two kinds of atoms (Ce^{3+}-F and Ce^{3+} next to the vacancy) in the ceria layer. Nevertheless, the measurement showed also a flaw of usage of fluorine – its limited stability in the layer. Even though the mixed CeOxFy samples were discontinuous, the reference CeO_2, Ce_2O_3 and CeF_3 samples were all thick and continuous, so the deconvolution procedure should have general applicability. This basic understanding of the spectrum of ceria allowed us to move to a more complex experimental setup of inverse catalyst.

In this chapter, main body consists of an article published in Journal of Physical Chemistry C [112]. We make use of the previously obtained information and apply them on an inverse catalyst setup. Such configuration permits to observe the interplay between the ordered substrate and the discontinuous ceria layer. The Ce 3*d* deconvolution technique allows us to observe and evaluate the oxidation state changes of cerium oxyfluoride layers and compare them with reference fluorine-free ceria samples. In this way, we are able to analyze the effect of fluorine-doping on the OSC of ceria layers. Moreover, the inverse configuration is able to reveal the morphological differences of fluorine-free and fluorine-doped ceria. The AFM measurements presented in this chapter were done by Mgr. Peter Kúš.

One of the concerns is also the practical applicability of the oxyfluoride layers. There is evidence that the reduced CeOx layers behave differently than the fully oxidized CeO_2 layers [62], [113], however, oxygen vacancies are not stable at oxygen rich conditions. Therefore, the idea to use the level of reduction of ceria layer to steer a reaction in a desired way may be challenging since the temperature induced reduction of ceria is observed only at very high temperatures even at UHV conditions [47], [52]. In contrast, fluorine induced reduction of ceria could permanently change the properties of ceria. Moreover, such material should be stable even at atmospheric conditions [79], [80]. However, it is of question whether the altered catalytic properties of reduced ceria are caused by the presence of oxygen vacancy or by the presence of a Ce^{3+} cation.

Another potential benefit of fluorine dopants could be their disruptive function in the ceria layer. It is well known, that the OSC of ordered ceria layers is lower in comparison with disordered ceria [114]. In fact, doping ceria with cations like Zr or Al/Mg should increase the dispersion of ceria and, by this, improve the temperature stability of the support while maintaining its good OSC. Fluorine in ceria could have the same disruptive effect.

The last unprecedented ability of anion dopants is their potential mobility in the layer. Such behavior could definitely change the charge transfer properties of such

layers and thus change the conductivity. Both, the ionic and electronic conductivities are important for any usage of ceria in fuel cells [115], yet, this particular effect will be more discussed in next chapters.

3.2.2. Introduction

Rhodium, platinum and palladium are dominantly used in today's three-way catalysts [7]. These noble metals are typically deposited in the topmost layers of the catalyst, where the most crucial processes, such as adsorption and reaction of reactants and desorption of products, take place. Cerium oxide or mixed Ce-Zr or Ce-Al oxides are used as a support for the active phase due to CeOx ability to store and release oxygen [8], [11], [116]. In oxygen lean environment cerium oxide provides extra oxygen for the reactions and gradually becomes reduced; however, the oxygen rich conditions cause its reoxidation. The reduction of cerium oxide is facilitated by formation of oxygen vacancies, with the oxide keeping its cubic FCC structure up to Ce_2O_3 [38], [117]. These processes help to promote the reactions catalyzed by cerium oxide-based catalysts.

Oxygen vacancies propagate through migration of oxygen in CeOx layers and between the CeOx layers and the active metal. Transfer of adsorbate atoms into the support is called spillover, while the opposite mechanism is called back-spillover or reverse spillover [67]–[69]. The amount of oxygen released from the CeOx layer is highly influenced by the structure and ordering of the substrate [114]. It was reported that the catalyst's performance drops due to degradation of the support or sintering of the active metals [8], [10]. These effects are commonly called ageing.

The utilization of mixed oxides (e.g. CeO_2-ZrO_2, CeO_2-Al_2O_3) in the support layer has three main reasons. Firstly, it hinders the Rh, Pt and Pd particles from sintering [12], [118]. Secondly, it stabilizes the cerium particles [8]. Thirdly, additives act as an impurity in the cerium oxide layers and thus hinder crystallization, create oxygen vacancies and promote oxygen mobility in the layer [36], [111], [114], [119]. All these effects lead to higher oxygen storage capacity and thermal stability of the catalysts.

Another way to disturb the homogeneity of a cerium compound is to replace the anion. Formation of cerium oxychloride as a result of chlorine introduction into Rh/CeO_2 was reported in refs [120] and [121]. Chlorine impurities lead to higher stability of Ce^{3+} state and higher rhodium dispersion. Similarly, fluorine is reported to create cerium oxyfluoride [78]–[80]. The most important difference between the anion substitution and the employment of mixed oxides is probably the ability of anions (e.g. fluorine or chlorine) to migrate in the cerium oxide lattice [73], [121]. The second important difference is the ability of anion dopants to enforce electronic changes in the oxide. Incorporation of fluorine or chlorine into the cerium oxide structure by substituting for oxygen leads to creation of Ce^{3+} sites through localization of 4*f* electrons on Ce atoms. This can substantially influence the catalytic and chemical properties of the material [113], [122].

Fluorine is quite a common impurity in rare earth ores [75]. Fluorine contamination of cerium oxide was reported in single crystals [71], [72] or on contact of cerium oxide and fluorine containing layers [73]. Other possible fluorine contamination is reported on exposing cerium oxide to fluorine vapors [78]. In contrast, exposure of fluorine contaminated cerium oxide layers to oxygen leads to decrease of fluorine concentration [104]. Similar behavior was reported for cerium oxychloride upon contact with air [121].

In this paper ([112]), we observe the electronic structure and compare catalytic properties of discontinuous fluorine-free CeOx/Rh(111) and fluorine-doped CeOxFy/Rh(111) inverse catalysts with respect to CO oxidation reactions. The inverse model catalyst approach allows us to observe the chemical changes of the cerium oxide layers in detail. Specifically, we focus on the reducibility of cerium oxide layers as the source of oxygen for the reaction. We investigate both the chemical and morphological changes induced by fluorine and discuss its depletion during oxidation. Additionally, we compare the morphology and ordering of the CeOx/Rh(111) and CeOxFy/Rh(111) samples upon heating. We measured the surface orientation by low energy electron diffraction (LEED) and the morphological changes by atomic force microscopy (AFM). Our results show differences in growth and ordering tendencies of the layers. At 250°C, CeOx/Rh(111) forms flat layers while CeOxFy/Rh(111) forms 3D islands. After annealing at 500°C CeO_2 exhibited distinct (1.4 × 1.4) spots with respect to the Rh(111) substrate, while the CeOxFy spots were either faint or elongated. This lengthening of the LEED spots is caused by stretching of the lattice constant of CeOxFy, which results in rotation of some of the islands by about 9° with respect to [1-10] direction of the substrate. Similarly rotated spots were observed on highly reduced, fluorine-free cerium oxide layers grown in ultrahigh vacuum (UHV) conditions. We also observed the changes of C 1*s*, O 1*s*, F 1*s* and Ce 3*d* core levels by X-ray photoelectron spectroscopy (XPS), and followed the CO_2 production during CO gas exposures via temperature programmed reaction (TPR) method. Our results show substantial changes in oxidation state of cerium oxide after CO and O_2 gas exposures at elevated temperatures and reveal depletion of fluorine during the oxidation cycle. Especially at elevated temperatures, oxygen displaces fluorine which then desorbs as hydrogen fluoride. After comparing the overall CO_2 production, CeOxFy layers show higher activity for CO oxidation reaction. The oxygen storage capacity, as measured by XPS, is also higher for the fluorine doped layers. The increased activity is primarily of morphological origin, with the CeOxFy samples exposing more of the Rh(111) substrate. Because Rh(111) surface can effectively store more oxygen than a single cerium oxide monolayer, the CO_2 production rates provide information about the surface coverage, rather than the oxygen storage capacity of cerium oxide. Nevertheless, the most important message of this paper is that anion doping provides a way for disruption of the regular CeO_2 structure, providing Ce^{3+} sites without reducing the oxygen storage capacity.

3.2.3. Experimental Section

XPS and TPR experiments were carried out in an ultrahigh vacuum system with a base pressure of 10^{-8} Pa. The Rh(111) single crystal (MaTecK) was cleaned by several cycles of Ar^+ ions sputtering followed by annealing at 600°C in 5×10^{-5} Pa of O_2 (Linde 4.5). The CeOx layers were deposited similarly to [52] by evaporating Ce metal (Alfa Aesar 99.9%) in oxygen atmosphere of 5×10^{-5} Pa at substrate temperature of 250°C. After the deposition, the sample was cooled down to room temperature in the oxygen atmosphere.

For the deposition of the CeOxFy layers, the source Ce metal was exposed to HF vapors. Before loading into evaporator, the metal was placed for 60 minutes approximately 2 cm over the surface of 20 vol% HF heated to 90°C. To avoid contamination of the system with fluorine, the preparation of the fluorine-doped layers was performed in a separate preparation chamber with a base pressure of 1×10^{-7} Pa. The CeOxFy layers were prepared by evaporating the fluorine exposed Ce

metal in oxygen atmosphere of 5×10^{-5} Pa at substrate temperature of 25°C. The oxygen inlet was closed 1 minute after the evaporation finished. Initial stoichiometry of the prepared layers was estimated using the XPS sensitivity factor analysis [105] to $CeO_{0.3}F_{0.5}$.

Three sets of CeOx and CeOxFy layers were prepared with varying coverage of the Rh(111) substrate. To quantify the amount of deposited material, we used several methods including quartz crystal microbalance system, attenuation of Rh 3*d* signal in XPS (with inelastic mean free path calculated by TPP-2M [90]), TPR and LEED. The most reliable evaluation was found to be Ce 3*d* area comparison combined with LEED and TPR measurements. Therefore, we define 1 monolayer equivalent (MLE) as an amount of deposited CeOx on Rh(111) at which the LEED pattern from the Rh(111) completely disappears and, simultaneously, the sample does not adsorb/desorb any CO. We note that we observed no CO adsorption/desorption on thick (>1 MLE) CeOx layers on Rh(111). The coverage of all the samples is henceforth calculated from the Ce 3*d* signal area with respect to 1 MLE CeOx sample. The coverage of the samples was assessed to be 0.2 MLE, 0.5 MLE and 0.65 MLE for CeOx/Rh(111) and 0.15 MLE, 0.55 MLE and 0.75 MLE for CeOxFy/Rh(111), with estimated accuracy of 0.1 MLE. The three pairs of samples are hereafter referred to as low, medium and high covered, respectively.

After the preparation, the samples were measured by LEED and XPS. The UHV chamber is equipped with a dual anode Mg/Al source and Omicron EA 125 hemispherical electron energy analyzer. All the spectra were measured using the $K\alpha_{1,2}$ lines of the Mg anode with excitation energy of 1253.6 eV. The TPR method employs a differentially pumped quadrupole mass spectrometer Leybold Inficon 2000. The gases for the TPR experiments are introduced into the system through two separate pipe lines, which prevents gas mixing. The incoming molecules pass through a small double aperture and form a simple molecular beam. The beam intensity is controlled via two precise variable leak valves. The sample holder allows programmed heating and cooling in the range of -100 – 600°C.

The TPR experiments included saturation CO exposures at 150°C (~ 5 L in 250 s, 1 Langmuir = 10^{-6} Torr × s), saturation O_2 exposures at 250°C (~ 5 L in 250 s) and annealing procedures to 500°C. We stress that all the CO exposures were conducted at sample temperature of 150°C and all the O_2 exposures at sample temperature of 250°C. At 150°C adsorbed oxygen on Rh(111) starts to react with CO and desorbs as CO_2, while CO desorption is still negligible at this temperature [114]. On the other hand, the O_2 exposure step at 250°C should deprive the surface of any remnants of CO and reoxidize the cerium oxide layer. CO desorption maximum is around 250°C. 250°C is also a temperature at which the oxygen atoms start to migrate through cerium oxide [123].

The TPR experiments were conducted in cycles with XPS measurements in-between each. The first CO (150°C) and O_2 (250°C) cycles were used for sample stabilization and their TPR results were not taken into consideration. Detailed experimental plan is schematically shown in Figure 12. The last experimental procedure consisted of combined exposure to both gases (CO : O_2 = 1:1) with gradually increasing temperature up to 500°C.

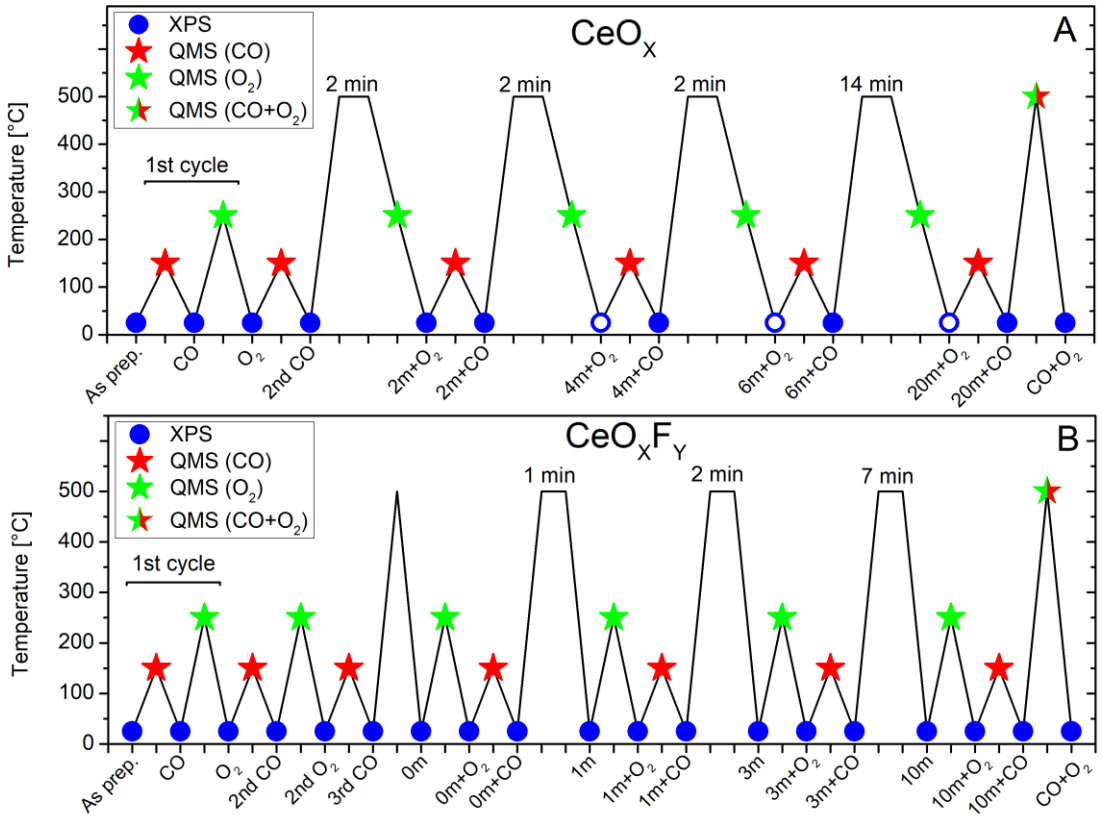

Figure 12: Experimental procedures and XPS measurements labeling for (A) CeOx/Rh(111) samples and (B) CeOxFy/Rh(111) samples. Empty circle symbols mark measurements conducted only on 0.5 MLE CeOx/Rh(111) sample as opposed to other CeOx/Rh(111) samples.

The shape of Ce 3*d* spectrum reflects the oxidation state of cerium. In order to evaluate such chemical changes, we deconvoluted the Ce 3*d* spectra into Ce^{3+}, Ce^{4+} and Ce-F doublets. The parameters and principles used for the Ce 3*d* spectra deconvolution are described in detail in section 3.1 and in publication [104].

Samples for ex situ AFM measurements were prepared in 5×10^{-5} Pa O_2 at substrate temperature of 250°C. The surface coverage was 0.75 MLE for both the fluorine-doped and fluorine-free samples. AFM Veeco di MultiMode-V, operating in ScanAsyst mode with Bruker ScanAsyst-Air probes, was used for the analysis. After the AFM measurement, the samples were checked by XPS and annealed in O_2 (5×10^{-5} Pa at 250°C) to reduce the carbon contamination. Except the carbon contamination, no chemical change of the sample was observed. The morphological change was induced by further annealing at 500°C for 5 minutes in 5×10^{-5} Pa O_2 and 5 minutes with the oxygen valve closed. Thereafter, the samples were again measured ex situ by AFM.

Detailed LEED experiments were carried out at the Materials Science Beamline at Elettra synchrotron in Trieste (Italy). The system has a base pressure of 1×10^{-8} Pa. The apparatus is equipped with a hemispherical electron energy analyzer Specs Phoibos 150, dual Mg/Al X-ray radiation source, LEED, evaporators, gas inlets and sample heating system. The samples were prepared at room temperature using the same preparation procedures as described above (including the first stabilizing cycle). The samples were heated in first annealing cycle for 1 min at 500°C and in second annealing cycle for 1 min at 800°C. Additionally, highly reduced CeOx/Rh(111) samples were prepared by CeOx growth in UHV conditions (without

the 5 × 10^{-5} Pa of O_2). The resulting layers exhibited high degree of reduction. In order to keep the samples reduced, such layers were only heated to 250°C, 500°C and 800°C in UHV. The surface coverage below 1 MLE was confirmed using the LEED method and the chemical state of the sample was checked by XPS.

3.2.4. Results – Morphology

The catalytic activity at the catalyst can be strongly influenced by morphological changes of the surface [15]. Inverse catalysts are convenient for study of thermal degradation processes and the influence of cerium oxide morphology on the catalytic activity [36], [111], [114]. The ageing of the catalysts causes morphological changes and decrease of oxygen storage capacity [10]. In this section, we will discuss growth of fluorine-free CeOx/Rh(111) and fluorine-doped CeOxFy/Rh(111) samples and their structural changes upon annealing.

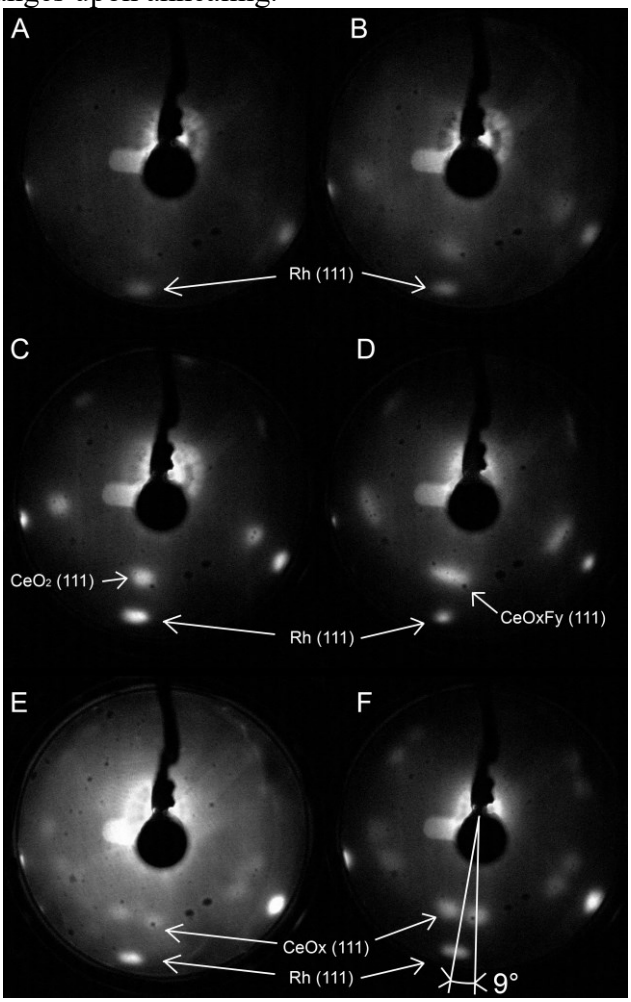

Figure 13: LEED diffractograms from thin (< 1 MLE), discontinuous layers: (A) (1 × 1) spots of Rh(111) substrate after CeOx/Rh(111) preparation at 25°C, 68 eV. (B) (1 × 1) spots of Rh(111) substrate and (1.4 × 1.4) spots of CeO_2 on the CeOx/Rh(111) after oxidation and reduction treatments at 250°C, 68 eV. (C) CeOx/Rh(111) after annealing at 500°C for 1 min, 68 eV. (D) (1 × 1) spots of Rh(111) substrate and (1.4 × 1.4) spots of CeOxFy on CeOxFy/Rh(111) after the annealing at 500°C for 1min, 68 eV. (E) (1 × 1) spots of Rh(111) substrate and (1.4 × 1.4) spots of CeOx grown in UHV conditions after the annealing at 500°C for 1 min, 68 eV. (F) CeOx grown in UHV after annealing at 800°C for 1 min, 68 eV.

After the preparation fluorine-free as well as fluorine-doped cerium oxide layers showed no or very weak ordering (the diffractogram from the as prepared CeOx/Rh(111) sample is shown in Figure 13 – A). After the gas treatments the layers slightly ordered creating a weak (1.4 × 1.4) superstructure over the (1 × 1) Rh(111) substrate (Figure 13 – B). After 1 minute at 500°C, we can see intense (1.4 × 1.4) spots (Figure 13 – C), which are noticeably broadened in the case of CeOxFy layers (Figure 13 – D). From this, we can conclude that both the fluorine free and fluorine-doped cerium oxide layers grow disordered at room temperature. The gas treatment cycle at 250°C leads to partial ordering of the layers. Further annealing at 500°C for 1 minute leads to creation of well-ordered layers. The broadened spots on fluorine doped samples are probably caused by the fluorine atoms, which hinder the ordering and cause an overall reduction of the cerium oxide layers by bonding to Ce atoms, substituting for oxygen. Looking at the Figure 13 – E, F, we can see thin reduced CeOx layers grown in UHV, which show 2 slightly rotated domains on the Rh(111) substrate. This rotation can be explained as a relaxation due to a lattice expansion of the reduced CeOx [124]. As the cerium oxide becomes more reduced, the lattice constant increases and the accompanying stress is released through rotation of the structure by about 9° with respect to the [1-10] direction of the substrate. This rotation is demonstrated by a simple structural model shown in Figure 14.

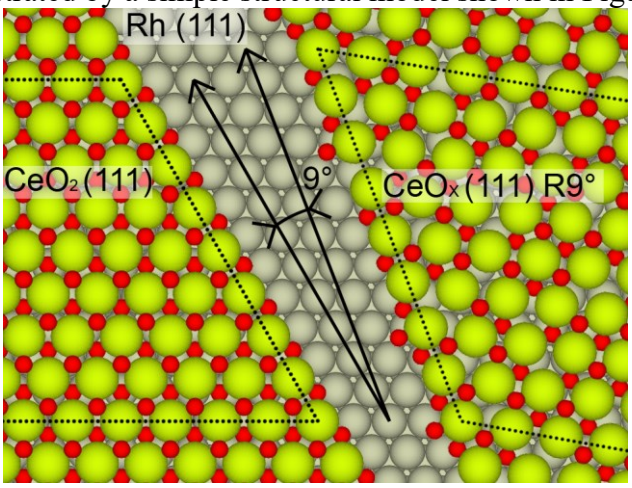

Figure 14: Epitaxial ordering model of fully oxidized cerium oxide (CeO_2(111)) and reduced cerium oxide (CeOx(111)) on Rh(111). The atoms are colored as follows: Rh (grey), Ce (yellow), O (red).

In the view of bulk properties of materials, Rh lattice parameter 3.8 Å corresponds to Rh(111) surface lattice constant 2.69 Å [125], while the CeO_2 lattice parameter 5.41 Å corresponds to CeO_2(111) surface lattice constant 3.84 Å. That makes the ratio between the two ca. 1:1.4. Mašek et al. [50] reported a shortening of the lattice parameter for thin cerium oxide layers deposited on Cu(111). The reported value 5.13 Å for 0.5 ML thick layers corresponds to CeO_2(111) surface lattice constant 3.63 Å. On the other hand, cerium oxide lattice constant grows as it becomes more reduced [124]. Our model in Figure 14 proposes expansion of the surface lattice parameter from 3.70 Å to 3.74 Å, which leads to a 8 × 8 coincidence between the Ce lattice and the Rh substrate (see Figure 14). This model corresponds well to the surface lattice constants determined from the LEED spots (Figure 13 – C and D), which are 3.7 Å and 3.8 Å for CeO_2/Rh(111) and CeOxFy/Rh(111), respectively. The discrepancy between the values reported by Mašek et al. [50] and the values considered for our model is likely related to the difference between the Cu(111) and Rh(111) substrates. The 9° rotation is brought about by a strain in the

CeOx structure, which prevents epitaxial growth in the Rh [1-10] direction, and, therefore, the CeOxFy layer relaxes by the rotation in order to maintain the 8 × 8 coincidence. The proposed surface lattice constant stretch is well within the reported values for reduction induced stretching, which can reach 3.5 % [124].

In view of these facts, the elongated LEED spots in Figure 13 – D can be explained by the presence of fluorine, which reduced the cerium oxide layers and caused rotation of some of the islands. Obviously, not all of the islands are rotated due to growth in oxygen atmosphere of 5×10^{-5} Pa. Especially smaller islands could be more susceptible to fluorine depletion and subsequent reorientation during the annealing procedures. Fluorine depletion and its impact will be further discussed in section 3.2.7.

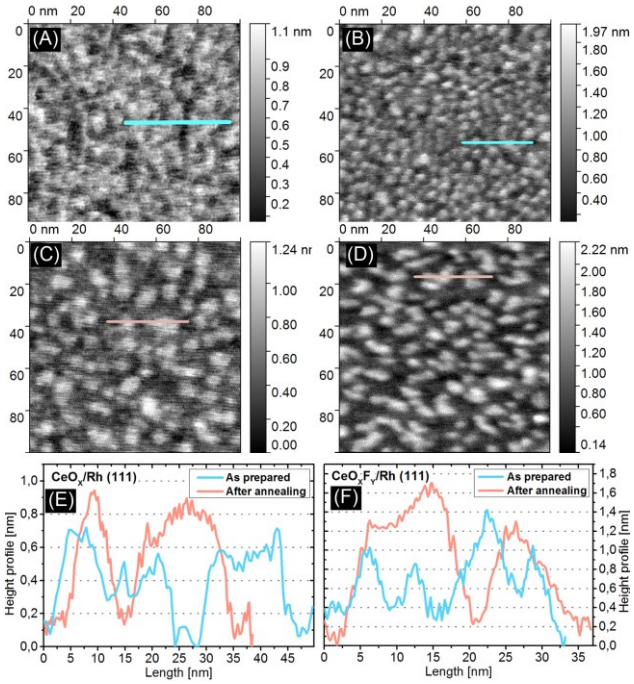

Figure 15: AFM images showing the morphological changes of 0.75 MLE CeOx/Rh(111) and 0.75 MLE CeOxFy /Rh(111) samples. (A) CeOx/Rh(111) after preparation (250°C) and several CO and O_2 procedures. (B) CeOxFy/Rh(111) after preparation (250°C) and several CO and O_2 procedures. (C) CeOx/Rh(111) sample after 5 minutes of annealing at 500°C in 5×10^{-5} Pa of O_2 and 5 minutes of annealing at 500°C in UHV conditions. (D) CeOxFy /Rh(111) sample after 5 minutes of annealing at 500°C in 5×10^{-5} Pa of O_2 and 5 minutes of annealing at 500°C in UHV conditions. (E) Height profiles of the CeOx/Rh(111) sample along the lines marked in (A) and (C). (F) Height profiles of the CeOxFy/Rh(111) sample along the lines marked in (B) and (D).

To check the morphological changes by AFM we prepared CeOxFy/Rh(111) and CeOx/Rh(111) samples with high surface coverage (0.75 MLE). The presence of Rh(111) LEED spots and CO adsorption and desorption were confirmed before the ex situ AFM measurements. The Figure 15 – (A) and (B) shows the surface morphology of CeOx/Rh(111) and CeOxFy/Rh(111) samples after the preparation at 250°C and several CO and O_2 gas treatments. The Rh(111) substrate is almost completely covered by cerium oxide. The CeOx comprises of flat islands with an average height of around 0.45 nm (Figure 15 – (A) and (E)). In contrast, the CeOxFy layer seems to form smaller, ca. 0.6 nm high 3D islands (Figure 15 – (B) and (F)). After annealing the sample for 5 minutes in 5×10^{-5} Pa of O_2 and 5 minutes in UHV

conditions at 500°C, cerium oxide clustered revealing the Rh(111) substrate. The CeOx islands reached the height of approximately 0.6 nm (Figure 15 – (C) and (E)). The (111) orientation of the CeO_2 surface was confirmed by LEED (data not shown). On the other hand, the CeOxFy layers formed much higher islands (ca. 1.1 nm) (Figure 15 – (D) and (F)) with only faint LEED spots (data not shown). These layers still contained a small amount of fluorine, so it is possible that the remaining fluorine acted here as a perturbation in the CeO_2 lattice, preventing it from ideal ordering. It is also apparent that fluorine modifies the morphology of the layers, promoting formation of 3D structures as a response of cerium oxide to the fluorine induced strain.

3.2.5. Results – Chemical Changes in Cerium Oxide

The evolution of oxidation state of cerium in CeOx/Rh(111) and CeOxFy/Rh(111) samples is clearly demonstrated in Figure 16. Figure 16 – A shows that CeOx/Rh(111) samples grown in oxygen atmosphere of 5×10^{-5} Pa are stoichiometric CeO_2, without any traces of Ce^{3+} atoms. The discontinuous CeOx layers are easily reducible by the CO stream. The samples stabilize with the first CO and O_2 exposures, which is manifested in shrinking oscillation of Ce^{4+} concentration between first O_2 and second CO exposure. During the CO exposure, the O_2 pre-exposed Rh surface is progressively covered with CO molecules, some of which react with oxygen and desorb as CO_2. The CeOx layers become partially reduced through an oxygen spillover to Rh(111) surface [68]. During the oxygen exposures, the O_2 molecules reoxidize the CeOx layers either directly or via oxygen back-spillover from the Rh surface [67].

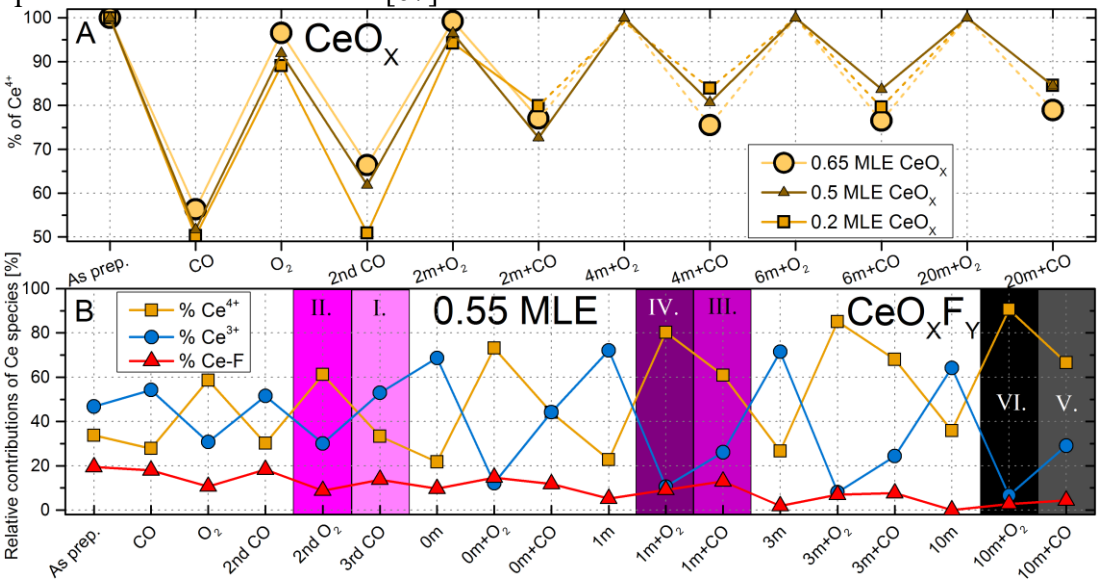

Figure 16: Oxidation state changes of cerium oxide after CO and O_2 gas exposures and annealing procedures at 500°C. The concentrations of the Ce species were obtained by fitting the Ce 3*d* spectra with estimated accuracy ± 3%. (A) The changes in Ce^{4+} concentration of CeOx/Rh(111) after preparation, CO and O_2 exposure procedures (150°C and 250°C) and step-wise annealing at 500°C for 2, 4, 6 and 20 minutes, additively. Every annealing step was followed by O_2 (250°C) and CO (150°C) exposures. The lines are guides to the eyes. (B) Relative contributions of Ce^{4+}, Ce^{3+} and Ce-F areas for the 0.55 MLE CeOxFy/Rh(111) sample. 0m means that after reaching the 5001C, the sample was immediately cooled down to the room temperature.

The ageing effects are simulated by annealing the samples to 500°C. After only two minutes of annealing, the reducibility of CeOx after the CO procedure (2m + CO) is considerably lowered. Subsequent annealing cycles (4, 6 and 20 minutes in total) influenced the reducibility of the layer only slightly.

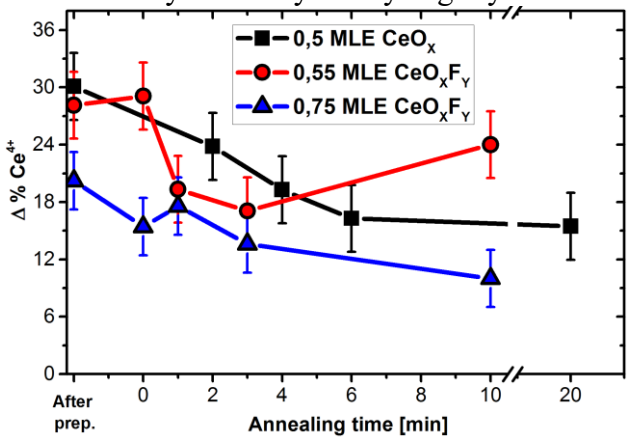

Figure 17: Changes of the Ce^{4+} area contribution to Ce 3*d* XPS spectrum after the CO reduction step in dependence on the time of annealing at 500°C for the 0.5 MLE CeOx/Rh(111), 0.55 MLE CeOxFy/Rh(111) and 0.75 MLE CeOxFy/Rh(111) samples. As explained in experimental section, first CO and O_2 cycle was used for sample stabilization and thus, these data were not taken into consideration. 0 minutes means that after reaching the 500°C, the sample was immediately cooled down to room temperature.

The changes in relative amount of Ce^{4+} after the CO reduction procedure are plotted in Figure 17 for the medium covered CeOx and CeOxFy samples and high covered CeOxFy sample. The changes in Ce^{4+} concentration from the state after the O_2 exposure to the state after the CO exposure (also referred to as reducibility of the sample or Δ % Ce^{4+}) are directly related to the amount of oxygen accessible during the CO oxidation reaction under these conditions (Langmuir doses of O_2 and/or CO in UHV). Comparing medium covered CeOx and CeOxFy samples, we can see that fluorine addition had not considerably altered the reducibility. After the series of annealing cycles, the reducibility is substantially lowered, which indicates that most of the oxygen in cerium oxide layers remains inaccessible during the CO oxidation reaction. The decrease of Δ % Ce^{4+} after the annealing cycles is caused mainly by coalescence and ordering of cerium oxide islands as was discussed in detail in section 3.2.4.

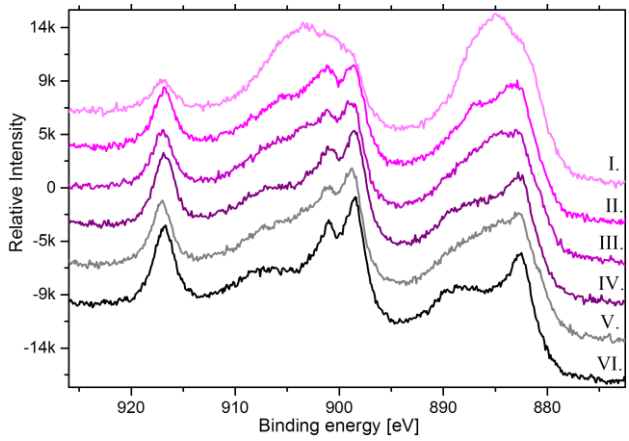

Figure 18: Evolution of Ce 3*d* spectra of the 0.55 MLE CeOxFy/Rh(111) sample at different stages marked in Figure 16 – B.

In Figure 16 – B, we can see the Ce 3*d* spectra components for the medium covered CeOxFy/Rh(111) sample. The most evident difference with respect to the CeOx layer is in the level of reduction of the fluorine-doped samples. Evolution of the Ce 3*d* spectra of the 0.55 MLE CeOxFy/Rh(111) sample with respect to the content of fluorine and previous sample treatment is plotted in Figure 18. The initial content of Ce^{4+} atoms is around 30% (see Figure 16 – B). The rest consists of the Ce^{3+} atoms located near the oxygen vacancy or the fluorine atom. The fluorine-doped layers are also oxidized after the oxygen exposure and reduced after the CO exposure, but they maintain their low concentration of Ce^{4+} atoms. In Figure 17, we can see that the reducibility of the 0.55 MLE CeOxFy sample is comparable to the 0.5 MLE CeOx sample. The reason for lower Δ % Ce^{4+} on high covered CeOxFy sample will be explained in section 3.2.6.

Although fluorine can be incorporated into CeO_2 without changing its oxidation state [78], the prepared cerium oxide layers had only a small portion of Ce^{4+} atoms, indicating that majority of the fluorine is actually bonded to cerium atoms. This is further supported by the fact that gradual fluorine depletion during the O_2-CO-annealing cycle leads to gradual oxidation of the CeOxFy layer (Figure 16 – B, Figure 18). The issue of fluorine depletion will be thoroughly discussed in section 3.2.7. Despite the fixation of a part of Ce atoms in the Ce^{3+} state by fluorine, the reducibility of the CeOxFy layer is comparable to CeOx layer, suggesting a similar amount of accessible oxygen during the reaction (Figure 17). In conclusion, our results indicate that fluorine disrupts the cerium oxide layers (see Figure 16) and facilitates the oxygen migration and oxygen vacancy creation and, by this, preserves the reducibility of the CeOxFy layers (Figure 16 – B and Figure 17). The preserved reducibility of the fluorine-doped samples can also be connected to the change in morphology (see Figure 15). The migration distance to the cerium oxide layer – Rh(111) interface is much shorter in the case of 3D islands than in the case of flat 2D islands.

3.2.6. Results – CO Oxidation Reaction

To compare the CO_2 production on the CeOx/Rh(111) and CeOxFy/Rh(111) samples, we exposed the samples consecutively to O_2 and CO gas streams and monitored the outgoing gases via the TPR method. The quadrupole signal provided information on the proceeding CO or O_2 adsorption and CO or CO_2 desorption. The total amount of produced CO_2 was calculated by integrating the areas under the CO_2 desorption curves recorded during the CO exposures (see Figure 19 – A).

The cerium oxide layers are oxidized during exposure to oxygen at 250°C, either by splitting and incorporating oxygen directly or by oxygen back-spillover from the Rh(111) substrate [67]. Oxygen also adsorbs dissociatively on the Rh(111) substrate, forming a (2 × 1) oxygen reconstruction on the surface [126]. During the subsequent sample exposure to CO at 150°C, the CO molecules react with the oxygen, form CO_2 and desorb. This involves both the oxygen adsorbed on Rh(111) and the oxygen in cerium oxide overlayer, which becomes accessible through the spillover from cerium oxide to the substrate [68], [69]. When all the accessible oxygen is depleted, the CO molecules adsorb on the Rh(111) surface without further reaction. We verified that CO does not adsorb or react directly with cerium oxide under these exposure conditions (CO exposures ~ 5 L in 250 s). We exposed thick, continuous CeOx/Rh(111) and CeOxFy/Rh(111) layers to CO and registered no CO adsorption or CO_2 production.

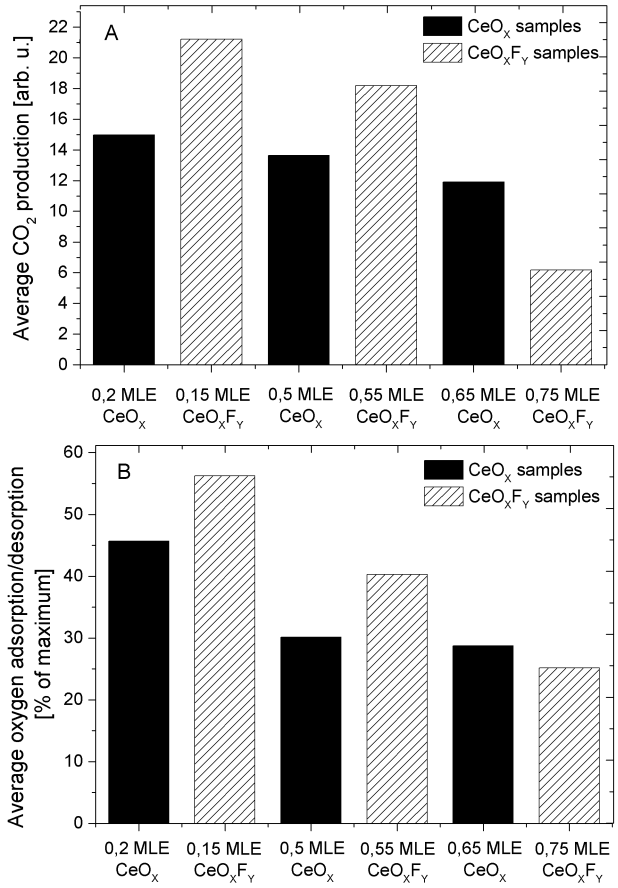

Figure 19: (A) Average CO_2 production of oxygen pre-exposed CeOx (full columns) and CeOxFy (striped columns) samples during the CO exposure at 150°C. (B) Average changes of O_{lat} area (cf. Figure 20) – after CO and O_2 exposures. Maximum O_{lat} area (i.e. CeO_2) for each sample corresponds to 100%.

We also evaluated the changes in O 1*s* area after consecutive exposures to O_2 and CO gases. To differentiate the components contributing to the O 1*s* signal, we fitted the O 1*s* spectra with three Voigt-type peaks as showed in Figure 20. The proper fit of the O 1*s* spectrum was possible only by utilizing the reference spectra of CO adsorbed on clean Rh(111) substrate. The CO molecules adsorb predominantly at the on-top sites at 150°C, while at room temperature CO occupies both the on-top and hollow sites [23]. The measured binding energies of 532.3 eV and 530.8 eV (cf. Figure 20 – III and IV) correspond well to the energies reported by Jaworowski et al.: 532.1 eV and 530.5 eV, respectively [23]. However, we cannot fully exclude the presence of OH groups on cerium oxide [113], which would have similar binding energy to the CO_{hollow} on Rh(111). By fitting the oxygen spectra, we could monitor the changes of O 1*s* – O_{lat} area, which corresponds either to oxygen adsorbed on Rh(111) or oxygen in cerium oxide lattice. Unfortunately, these two oxygen contributions cannot be distinguished.

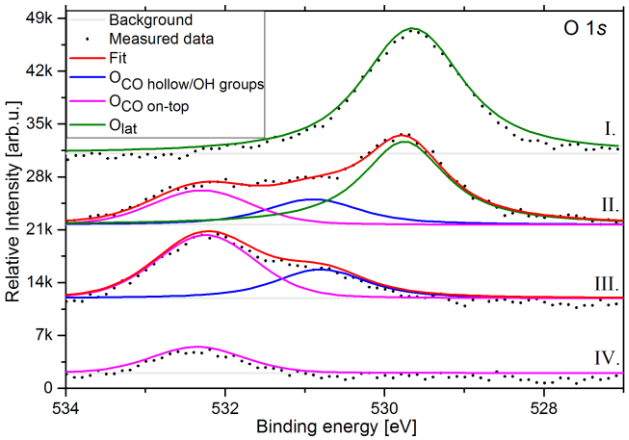

Figure 20: The O 1*s* XPS spectra of different samples fitted by three Voigt-type peaks. (blue) O_{CO} hollow/OH groups; (pink) O_{CO} on-top; (green) O_{lat}. (I.) Discontinuous layer of CeOx/Rh(111) without any traces of CO or OH after O_2 exposure. (II.) Discontinuous layer of CeOx/Rh(111) after CO exposure. (III.) CO in on-top and hollow positions adsorbed on the Rh(111) substrate at room temperature. (IV.) CO adsorbed only in the on-top positions after CO exposure of Rh(111) at 150°C.

Thus, to compare the CeOx/Rh(111) and CeOxFy/Rh(111) samples, we evaluated the relative changes in the area of O_{lat} peak after the O_2 and CO gas treatments. After the oxygen exposure at 250°C, the cerium oxide layers are highly oxidized and the Rh(111) substrate is covered with oxygen. There are no remnants of CO or other carbonate species (see Figure 20 – I). Therefore, the O_{lat} peak intensity is higher than that after the CO treatment (see Figure 20 – II), when all oxygen from the Rh(111) surface and available oxygen from the cerium oxide layers were consumed in the CO oxidation reaction.

The relative changes in O_{lat} areas are displayed in Figure 19 – B. There is a clear correlation between these results and the CO_2 production data in Figure 19 – A. At 250°C the oxygen adsorbed on Rh(111) is still firmly bonded to the Rh(111) substrate and its reaction with CO and desorption as CO_2 is the only way by which it can leave the sample. Thus, we can conclude that the amount of oxygen consumed during the reaction with CO directly relates to the quantity of produced CO_2.

The most noticeable phenomenon in Figure 19 is the decrease of produced CO_2 with the increase of the Rh(111) coverage. This can be explained by considering the amount of oxygen which is available for the reaction. We know from LEED images that CeO_2 shows ca. (1.4 × 1.4) spots with respect to Rh(111) [52] (see Figure 14). Thus, in 2D view, the area of 4 CeO_2 primitive cells equals 9 Rh lattice structures. 4 CeO_2 primitive cells can provide 2 O atoms by reducing to 2 Ce_2O_3. Moreover, the percentage of O atoms in cerium oxide that is actually available for the reaction is even lower, around 25% (see section 3.2.5 and Figure 17). In contrast, the Rh(111) surface provides adsorption positions for oxygen up to 0.5 ML, forming (2 × 1) O - Rh(111) reconstruction [126]. 9 Rh units can thus provide as much as 4.5 O atoms, which is more than twice as much as cerium oxide can provide from the same area. Therefore, the amount of produced CO_2 reflects the area of uncovered Rh(111) surface and morphology of cerium oxide, rather than a quantity of oxygen released from the cerium oxide layer.

The fact that the Δ % Ce^{4+} further drops to 12% on high covered CeOxFy/Rh(111) sample (see Figure 17) is probably caused by larger area of cerium oxide islands, which increases distance from the island center to the free Rh surface

(see Figure 21). As CO adsorbs predominantly on Rh(111), the oxygen has to spillover from the cerium oxide layers to the Rh(111) substrate in order to react with the CO and desorb as CO_2. The mobility of oxygen atoms seems to play an important role in this step. It is probable that, with growing distance to the cerium oxide – rhodium interface, the amount of oxygen vacancies in cerium oxide islands has a gradient in the horizontal direction. Similar, thermodynamically driven gradient has been previously observed in the vertical direction [38]. Therefore, higher surface coverage results in lower CO_2 production not only due to covering of the Rh(111) substrate but also due to limited oxygen mobility and, therefore, limited spillover from island centers. This model can explain lower production of CO_2 on 0.75 MLE CeOxFy/Rh(111) sample in comparison with 0.65 MLE CeOx/Rh(111) (see Figure 19) and also the lower reducibility of the 0.75 MLE CeOxFy sample in comparison with the 0.55 MLE CeOxFy sample (see Figure 17).

On the other hand, the higher CO_2 production of 0.55 MLE CeOxFy sample in comparison with 0.5 MLE CeOx sample (see Figure 19) can be explained by formation of higher islands in the case of fluorine-doped cerium oxide (see section 3.2.4). 3D islands reveal larger area of Rh(111) than flat CeOx layers for the same amount of material; thus, the CO_2 production is higher. Moreover, the 3D stacked CeOxFy islands have shorter oxygen migration distance from the island centers than the 2D CeOx layers.

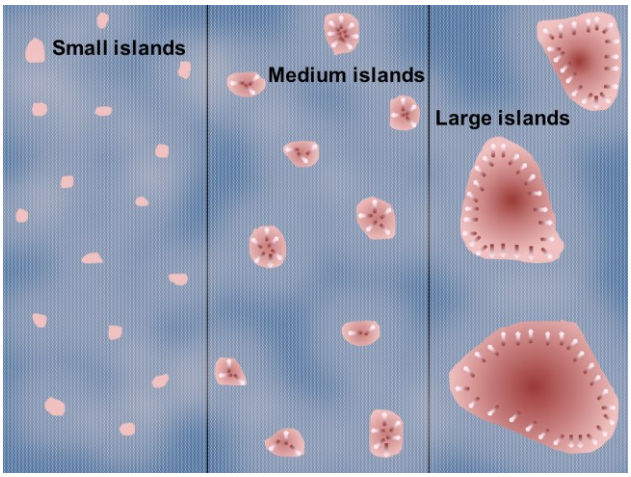

Figure 21: Influence of island size on the oxygen spillover. The limited migration distance of oxygen from the cerium oxide layer (red) to Rh(111) (blue) results in lower reduction of centers of large islands. The darker the color of the CeOx island, the higher the amount of Ce^{4+}.

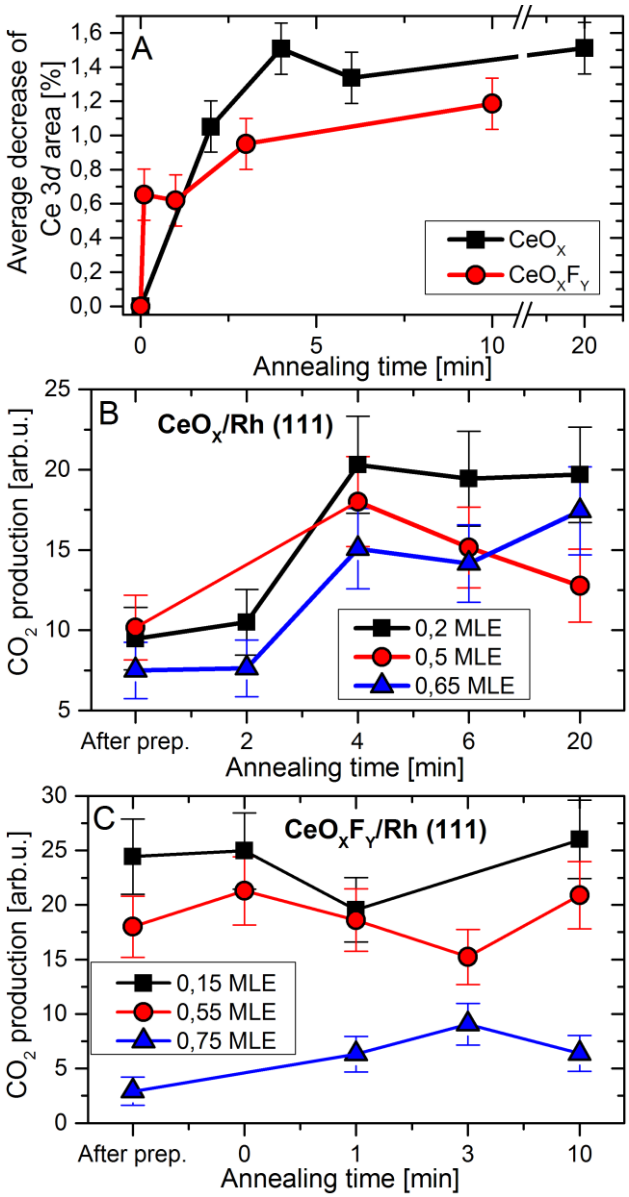

Figure 22: (A) Average decrease of the Ce 3*d* area measured by XPS for all samples. Data were collected after the annealing (500°C) procedures. 100% corresponds to Ce 3*d* area of every sample after the preparation. The total annealing time is plotted on the x-axis. The decrease at 0 min corresponds to the state after the 0m procedure (cf. Figure 12 – (B)). (B,C) The amount of produced CO_2 during the CO exposures at 150°C for the CeOx/Rh(111) and CeOxFy/Rh(111) samples, respectively. The samples exposed with oxygen prior to the CO exposures.

To check the speed of the coalescence of cerium oxide islands, we plotted the decrease of the Ce 3*d* area as measured from the XPS in Figure 22 – (A). The results for the CeOxFy/Rh(111) and CeOx/Rh(111) samples do not differ significantly. The Ce 3*d* area of fluorine-doped CeOxFy/Rh(111) samples lowered in average by 1% while the fluorine-free samples showed about 1.4% decrease. The area dropped immediately after heating to 500°C. After about 5 minutes of annealing at 500°C, the Ce 3*d* area ceased to decrease.

As a consequence of the coalescence and 3D stacking of the islands, CO_2 production should rise due to larger area of free Rh(111) surface. On the other hand, the increasing area of individual islands (compare Figure 15 – A and C, Figure 15 –

B and D) reduces the oxygen spillover from the cerium oxide. Moreover the oriented CeO_2(111) is more likely to impede the oxygen vacancy formation in comparison with the disordered structure [36], [114], [127]. Our results in section 3.2.5 also support this fact, illustrating the decrease in reducibility. Nevertheless, the uncovered Rh(111) area is the determining factor for the overall CO_2 production as follows from Figure 22 – (B). The CO_2 production of all three CeOx/Rh(111) samples is almost doubled after the 4 minutes of annealing at 500°C, primarily due to the twice as high oxygen capacity of free Rh(111) surface compared with the CeOx, as was discussed above.

On the other hand, the CeOxFy/Rh(111) samples do not show any CO_2 production increase after the annealing even though the morphological changes are evident in Figure 15 – (B) and (D). A possible explanation of this phenomenon lies in the 3D stacking of the CeOxFy layers. By merging the 3D islands due to the coalescence, the overall Rh(111) surface area covered by the cerium oxide layers does not change as much as in the case of a 2D → 3D transition on CeOx/Rh(111) samples. This effect can explain the stable CO_2 production on the CeOxFy/Rh(111) samples in Figure 22 – (C).

The most important conclusion from CO_2 production on these discontinuous layers is that they give information about the cerium oxide morphology and Rh(111) coverage rather than about the oxygen spillover efficiency. The oxygen spillover and back-spillover is therefore best documented by shape alterations of the Ce 3*d* spectra, showed and evaluated in Figure 18 and Figure 16.

3.2.7. Results – Fluorine Depletion

The Ce-F doublets are obtained from Ce 3*d* XPS spectra by fitting and evaluating the contributions corresponding to Ce bonded to fluorine [104]. The area of Ce-F doublets is directly related to the amount of fluorine in the layer. Thus, as the quantity of fluorine gradually decreases, the Ce-F signal becomes less intense (see Figure 16 – B). The changes in the shape of the Ce 3*d* spectra after the oxidation and reduction procedures as well as the overall changes of the shape caused by the loss of fluorine are displayed in Figure 18.

From the data shown in Figure 16, it is clear that the fluorine depletion is a consequence of the O_2-CO-annealing cycle. With each cycle, the Ce-F signal decreases and the Ce^{4+} signal grows, which indicates that fluorine is replaced by oxygen. The decrease of fluorine could be caused either by desorption or by diffusion into the Rh(111) substrate. However, no fluorine was observed by XPS after a removal of the cerium oxide layers by Ar^+ sputtering. Moreover, fluorine tends to migrate into the cerium oxide [73] or, specifically, to the surface of cerium oxide [72], rather than to the substrate. These facts, along with the rapid decrease of Ce-F area on low covered sample (data not shown), support the fluorine desorption theory. Therefore, we employed TPR to monitor the outgoing fluorine and some of its possible compounds (HF, OF, COF_2) during the gas exposures. Although the signal intensity was very low, we were able to follow the desorption by time averaging of all the measured data from respective (O_2, CO, annealing) procedures. We also measured the F 1*s* peak and averaged the area decrements after each procedure. We considered all the sample thicknesses and every XPS measurement which followed that kind of procedure. The results of the analysis are displayed in Figure 23.

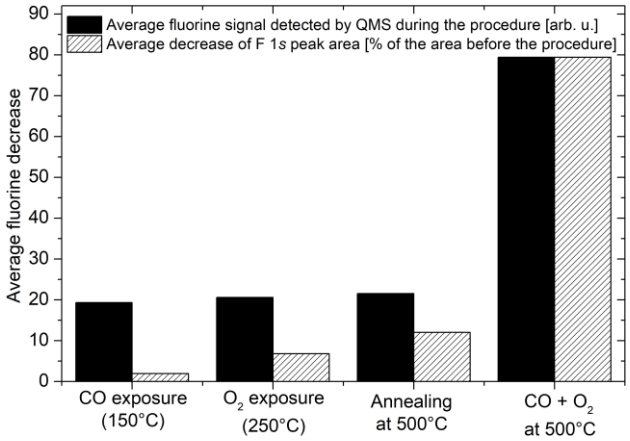

Figure 23: Average fluorine desorption peak area (full columns) and F 1*s* XPS signal decrease (striped columns) after various sample treatments.

It is obvious that fluorine depletion depends on the temperature; however, the most intense fluorine dissipation was observed during/after the annealing at 500°C along with the simultaneous CO and O_2 ($CO+O_2$) gas exposure (last procedure in Figure 12 – B). While the gas phase oxygen displaces the fluorine [79], the elevated temperature enhances mobility of fluorine in the cerium oxide layer [73].

We have also observed a small desorption peak of hydrogen fluorine during annealing of a thick CeOxFy/Rh(111) sample to 600°C (data not shown). As the hydrogen molecule is the most abundant element in the residual UHV atmosphere, fluorine can react with hydrogen and desorb at higher temperatures. Hydrogen dissociation could be facilitated by the presence of Rh(111) surface [128]. Another possibility is a dissociation of hydrogen molecules on the cerium oxide surface [129]. In this case, hydrogen binds to the surface oxygen, forming OH groups. The OH groups can then swap the hydrogen with the fluorine on the surface. Third possible origin of hydrogen is water in the residual atmosphere. Water can dissociate on reduced CeOx [113] and create OH groups. The remaining hydrogen could then react with fluorine and desorb as HF. Similar processes were already proposed for LaOF and LaF_3 oxidation [130] and reported for CeOF at atmospheric pressures [80].

Ability of cerium oxides to absorb fluorine is already investigated for application in fluorine removal from aqueous solutions [82]. Consequently, oxygen stimulated fluorine desorption at elevated temperatures could be used for regeneration of cerium oxide based fluorine absorbents. In this way, the reusable CeOx based fluorine absorbents could provide a cheap way for fluorine removal from chemical wastewater or from contaminated drinking water.

3.2.8. Conclusion

In conclusion, our results show that discontinuous fluorine-free CeOx layers grow as 2D islands on Rh(111) whereas fluorine addition promotes 3D growth of CeOxFy layers on Rh(111). Annealing of the samples caused a gradual ordering of the layers into the (1.4 × 1.4) superstructure on the (1 × 1) Rh(111) substrate. Fluorine-doped samples showed broadened LEED spots due to stretching of the lattice parameter and relaxation into two 9° rotated domains. Similar relaxation was observed for highly reduced CeOx layers prepared by Ce evaporation in UHV conditions.

Our Ce 3*d* XPS spectra analyses revealed changes in Ce^{4+}, Ce^{3+} and Ce-F contributions in dependence on the sample treatment. After the oxygen exposures at

250°C, the layers oxidize, while exposures to CO at 150°C cause creation of oxygen vacancies and reduction of the cerium oxide layers. Fluorine dopants cause reduction of the layer, fixing some of the Ce atoms in the Ce^{3+} oxidation state. Nevertheless, the Ce 3*d* spectra analyses showed that doping with fluorine does not decrease the overall amount of Ce atoms undergoing oxidation and reduction during the reaction. This finding implies that fluorine dopants in CeOxFy do not hinder oxygen vacancy creation and that the oxygen surrounded Ce atoms can still reversibly vary between Ce^{4+} and Ce^{3+}.

We also compared the quantity of produced CO_2 on CeOxFy/Rh(111) and CeOx/Rh(111). We recorded the gases desorbing from the samples during CO treatments at 150°C. The total amount of produced CO_2 is mainly influenced by the extent of uncovered Rh(111) area. Moreover, we monitored and fitted the O 1*s* spectra, measured before and after the CO exposure. We found out that the relative decrease in O_{lat} area coincides with CO_2 production due to the oxygen consumption during the CO oxidation reaction. The difference between fluorine-free and fluorine-doped samples was found to be mainly caused by the change in the morphology of the cerium oxide layers on the Rh(111) substrate. While the CeOx forms flat 2D islands, the CeOxFy stacks into 3D islands. After annealing, CeOx transforms to 3D islands exposing more of the Rh(111) substrate. This effectively increases the quantity of produced CO_2 on the CeOx/Rh(111) samples. No similar increase was observed on the CeOxFy/Rh(111) samples.

The Ce 3*d* XPS data also showed that fluorine gradually depletes from the CeOxFy layers, possibly due to desorption in the form of HF. The fluorine depletion seems to be thermally and chemically promoted. This could be caused by a limited migration of fluorine in the CeOxFy layer at low temperatures. The highest fluorine loss was measured after the combined (1:1) $CO+O_2$ exposure at 500°C, with oxygen expected to be responsible for the fluorine replacement.

In summary, the addition of fluorine significantly reduces the cerium oxide layers without altering the oxygen storage capacity. The modifications of the electronic and morphological structure indicate that anion doping could play a key role in rational design of future cerium oxide based catalysts. Thermally activated fluorine desorption in oxygen atmosphere can also be utilized in regeneration of cerium oxide based fluorine adsorbents.

3.3. Anion-Mediated Electronic Effects in Fluorine-Doped Ceria

3.3.1. Preface

The results presented in the previous chapter seem quite optimistic for any application of anion doping as a tool for steering the chemistry of a catalyst in a desired way. Since fluorine addition did not alter the most valued faculty of ceria – oxygen storing, there is a chance that the anion dopants could alter the surface chemistry of the material without any serious damage to their main purpose. Moreover, such tools could have unprecedented capabilities like mobility in the oxide layer [73], [131]. Stability of fluorine in the layer should be good in comparison to other potential anion dopants thanks to its high electronegativity and small ionic radius comparable to that of oxygen. Furthermore, fluorine favors to migrate to the surface rather than to stay in the bulk [71], [72]. All these properties make fluorine anion the most promising candidate for engineering the chemistry of catalysts.

Main body of this chapter consists of a manuscript describing the changes in valence band induced by fluorine doping of ceria. Since changes in valence band play a crucial role in chemistry of such material, the observed variations have a potential to steer the properties of fluorine-doped ceria.

The manuscript was written in collaboration with the University Uppsala in Sweden, namely with Dr. Mathew Wolf, Dr. Jolla Kullgren, and Prof. Kersti Hermannson, who conducted the DFT calculations and provided the necessary theoretical insight. The text of the manuscript was improved by Dr. Senjaya D. Senanayake from Brookhaven National Laboratory in order to increase its readability and potential impact on the targeted audience.

3.3.2. Introduction

Cation dopants are commonly used to tailor the (heterogeneous) catalytic activity and selectivity of reducible oxides, through concerted changes to the electronic structure, morphology and metal–support interactions [64], [132], [133]. In contrast, anions (such as pnictogens or halides) are seldom considered as dopants, despite the fact that anion mediated reactivity is common in homogenous organometallic catalysis [134], [135]. This is in part due to a lack of understanding of the true nature of such dopants in oxides. Herein, we study the effect of F anion doping on a prototypical reducible oxide system, namely CeO_2 (ceria), and establish the modifications to the electronic structure using a combination of experimental and theoretical approaches. Our results indicate that doping with anions represents a straightforward and well controlled method for altering catalytic chemistry through the manipulation of the electron density and properties arising thereof.

In numerous heterogeneously catalyzed reactions, charge transfer between the substrate and adsorbate(s) is the rate-limiting step [115]. Charge transfer is governed by the nature and energetic alignment of the participating electronic states [136], [137]. The participating states of the substrate are typically those of the valence band; consequently, deliberate modification of the valence band density of states provides a means to influence charge transfer-limited reactions. So-called valence band engineering may be achieved in various ways. Some are physical, such as stress-induced lattice constant modification, and some are chemical, most notably doping with impurities [138]–[140]. Ceria is a prototypical reducible rare earth oxide that has become a mainstay in catalytic applications where oxygen storage and dissociation of water are essential [141]. However, typically, it is not catalytically active unless combined with a metal, although there are some known exceptions [142], [143]. Current research in ceria based catalysis is primarily oriented towards strategies to improve on the reducibility, conductivity and oxygen storage capacity of ceria by way of metal supported oxides (M–CeOx), mixed oxides (MOx–CeOx) and promoters (P–CeOx) [62], often involving (a) foreign cation(s) used to influence phenomenological effects in ceria.

Instead we have focus on the possibility of anion doping, specifically with the use of fluorine, a strongly electronegative halogen gas. The reasons for this choice of dopant are numerous: firstly, although the Ce^{4+}/Ce^{3+} couple has long been believed to play the dominant role in reactions, recent work has highlighted the role of the anion states of the valence band [144], [145]. Furthermore, CeOF is known to form a stable compound with very similar structural properties as ceria [79], [80], [146], indicating that various levels of F incorporation could be achieved with minimal distortion to the structure of the host lattice [71]. Finally, we note that such doping

can take the form of unintentional contamination [72], [73]. This is especially relevant due to the prevalent use of ceria in modern hydrogen fuel cell technology, where Nafion is used as a proton conductor, and is in direct contact with ceria at the anode [77], [141]. Furthermore, Teflon is often used as a coating for hydrophobicity, for example in autoclaves, and in sealing materials. Despite the importance of the above-mentioned applications, the understanding of the properties of fluorine doped ceria is lacking, and there is a lack of guiding design principles on how to use it to achieve positive effects in ceria.

Fluorine is incorporated into ceria as F^- ions substituting for lattice O^{2-}. The most obvious electronic effect of this substitution is the addition to the system of one electron per fluoride ion, which is immediately evident from the electronic configurations of oxygen ([He] $2s^2$ $2p^4$) and fluorine ([He] $2s^2$ $2p^5$) atoms. The excess electron localizes in a 4*f* orbital of a single Ce ion, reducing the nominal oxidation state of the ion from 4+ to 3+. However, as we have shown previously, the Ce^{3+} ion associated with an F^- substituent is not spectroscopically identical to those in pure ceria, as is directly evident from Ce 3*d* core-level photoemission spectra, where both the ratio and position of the final state components differ [104], implying a distinct screening response to the 3*d* core hole [44], [147]. One plausible explanation is the different local environments of the two Ce^{3+} species; the Ce^{3+} associated with an oxygen vacancy resides in the next-nearest position [148], and is therefore surrounded by 6 O ions, whereas that associated with an F substituent resides in the nearest neighbor position and is therefore surrounded by 1 F and 5 O ions [71], [131]. The alteration of Ce^{3+} ion properties is important because of the significant role that 4*f* electrons play in ceria related chemistry [149], but it can also be utilized in determining fluorine concentration in ceria, as is done here, and could explain otherwise anomalous core-level spectra reported elsewhere in the literature [77].

3.3.3. Results and Discussion

In this work, we are interested in investigating more subtle electronic features induced by the incorporation of F into ceria. In Ref. [71], it was predicted that the 2*p* levels of surface F^- ions should reside at energies towards the bottom of the valence band of ceria, which was used to explain their appearance as depressions in STM experiments [117], and would therefore be difficult, if not impossible, to reveal by ordinary photo-electron spectroscopy. Therefore, we approach this question by resonant photoemission spectroscopy at the Ce 4*d* → Ce 4*f* photoabsorption threshold. The resonant photoemission process in ceria is of a twofold nature [45]. In the case of Ce^{3+} ions it is an intraatomic process that greatly enhances the spectral gain from 4*f* electrons, allowing detection of such species when present even in very small concentrations. In the case of Ce^{4+} ions it is an interatomic process that carries information about cation – anion covalency. We leverage these benefits in a comparative study of two pairs of ceria samples: One containing essentially only Ce^{3+} ions ($Ce_1^{3+}O_{1.06}^{2-}F_{0.88}^{1-}$ and $Ce_2^{3+}O_3^{2-}$), and the other containing both Ce^{3+} and Ce^{4+} ions ($Ce_{0.55}^{4+}Ce_{0.45}^{3+}O_{1.37}^{2-}F_{0.80}^{1-}$, $Ce_{0.73}^{4+}Ce_{0.27}^{3+}O_{1.87}^{2-}$). The stoichiometry of the referential undoped samples was chosen so as to enable direct comparison with respect to the Ce^{3+}/Ce^{4+} ratio. The measured resonant photoemission spectra are shown in Figure 24.

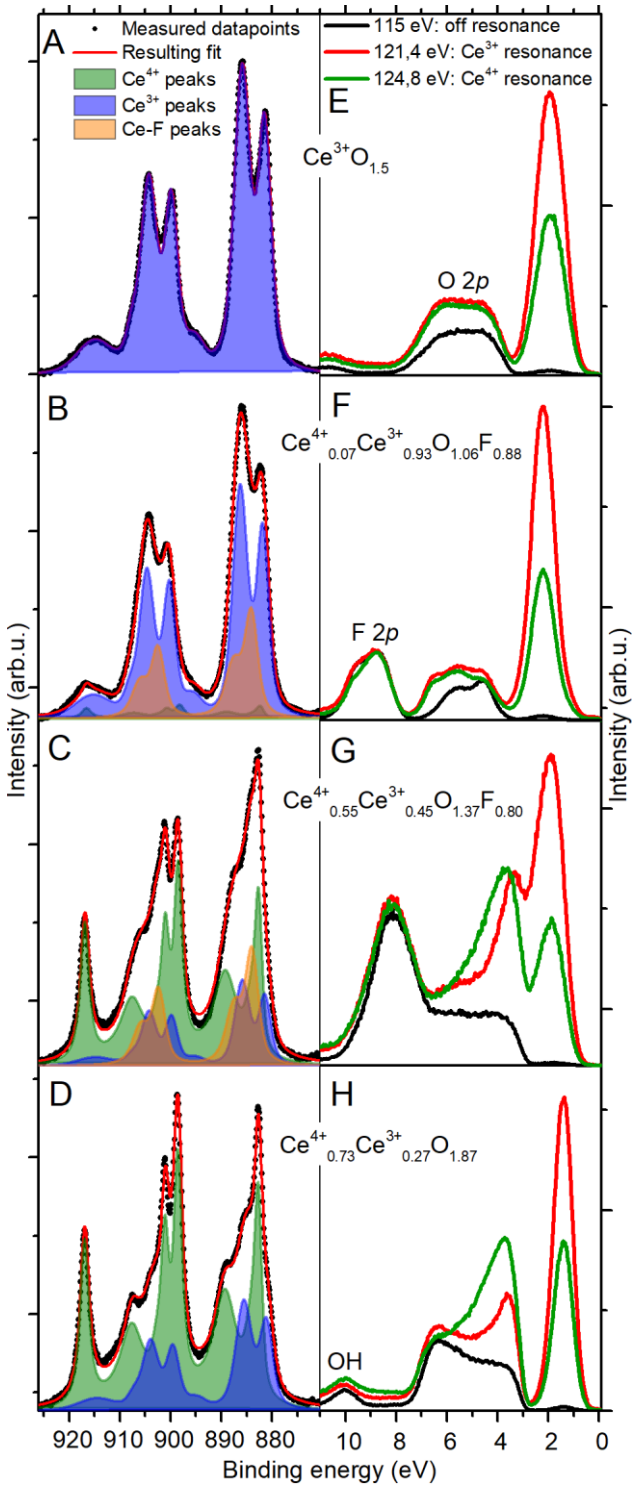

Figure 24: XPS and SPRPES spectra of representative (fluorine doped) ceria samples. Ce 3*d* core levels (A – D) were measured with photon energy of 1253.6 eV. Valence band spectra (E – H) were measured with energy of 115 eV (off resonance), 121.4 eV (Ce^{3+} resonance) and 124.8 eV (Ce^{4+} resonance). All spectra were normalized to the maximum intensity. Deconvolution of the Ce 3*d* spectra (green, blue and orange lines in A – D) has been carried out according to [104].

We start the discussion by comparing the spectra of samples containing virtually only Ce^{3+} ions i.e. c-Ce_2O_3 and CeOF, shown in Figure 24, panels E and F. Ce_2O_3 exhibits two bands, due to occupied Ce 4*f* and O 2*p* states. The most striking effect

of the inclusion of F is a new broad spectral feature which we ascribe to F 2*p* states, which consists of two contributions at 8.6 eV and 9.5 eV. We also notice a slight alteration of the O 2*p* spectral envelope, which we expect to be modified by two effects. The substitutional fluorine incorporation changes the relative amount of the O 2*p* electrons with respect to $Ce_2^{3+}O_3^{2-}$ and also creates new coordination shells for oxygen atoms. The latter influences the electrostatic potential around the oxygen atoms, and consequently the degree of covalency of the bond between O 2*p* and Ce 4*f* and Ce 5*d* electrons [150]. We note that this affects charge transfer between the anions and cerium atoms, the consequence of which is the distinct response to a Ce 3*d* core hole (as discussed above), but the most significant effect on the chemistry will be provided by direct interaction with the F 2*p* electrons.

Surprisingly, the F doped sample of intermediate stoichiometry presents a qualitatively different spectrum (see Figure 24 panel G). The previously observed F 2*p* spectral features appear to be shifted towards lower binding energy and, possibly due to overlap of several states, to form a broad envelope with maximum at 8.2 eV. Interestingly, the shift leads to conjoining of the F 2*p* and O 2*p* spectral envelopes. Even more remarkable is the modification of the density of states at the top of the O 2*p* band, which, while invisible using off resonant photon energies, is revealed through the resonant photoemission process. Specifically, we see a new maximum appear at the Ce 4*d* → Ce 4*f* photoabsorption threshold for Ce^{3+} ions (121.4 eV) at a binding energy of 3.4 eV. These states are necessarily distinct from the resonating O 2*p* states which in principal cannot have the same intensity at photon energies both below and at the Ce 4*d* → Ce 4*f* photoabsorption threshold for Ce^{4+} ions (124.8 eV) [12] (compare with Figure 24, panel H). Furthermore, due to the nature of the resonant photoemission process in ceria [45], these states must also include contributions from Ce^{4+} ions, which is emphasized by the fact that presence of fluorine in ceria containing only Ce^{3+} ions does not lead to the same effect. Both the observed shift of the F 2*p* states towards the bottom of the valence band, and the emergence of new states at the top of the O 2*p* band represent distinct elements of possible fluorine facilitated valence band engineering in ceria based materials.

In order to understand the origin of the fluorine induced modification of the valence band density of states, we used hybrid density functional theory calculations to investigate various models of fluorine incorporation into ceria. We initially consider models containing fluorine substituents in the surface, and subsurface oxygen layers of a (111) ceria slab. The corresponding calculated atom projected densities of states are shown in Figure 25, panels A and B. Starting from the fluorine in the first oxygen layer, we see that the F 2*p* states move to higher binding energy the deeper the fluorine is (a shift of about 0.5 eV) between the surface and subsurface fluorine, from 7.5 eV to 8.0 eV. The result of this is that there is no gap between the F 2*p* and O 2*p* states for surface fluorine, in contrast to the subsurface position. Here, we recall that the measured valence band photoemission spectra exhibit a gap in the case of fully reduced $Ce_1^{3+}O_{1.06}^{2-}F_{0.88}^{1-}$, but not in the case of $Ce_{0.55}^{4+}Ce_{0.45}^{3+}O_{1.37}^{2-}F_{0.80}^{1-}$. Taking this into account, the calculated results seem to indicate a different depth distribution of fluorine for the two samples. While we expect fluorine to be located in the surface of a thermodynamically equilibrated ceria sample, this has been determined only for the case of low level of reduction. It is conceivable that the situation is different for ceria containing only Ce^{3+} ions. Severe reduction of ceria leads to stabilization of ordered structure of oxygen vacancies in the surface, which could hinder the segregation of fluorine to the surface. Consequently, not only the concentration of fluorine, but also the concentration of oxygen vacancies affects the

depth distributions of fluorine in the sample and therefore the binding energy of the F 2*p* states.

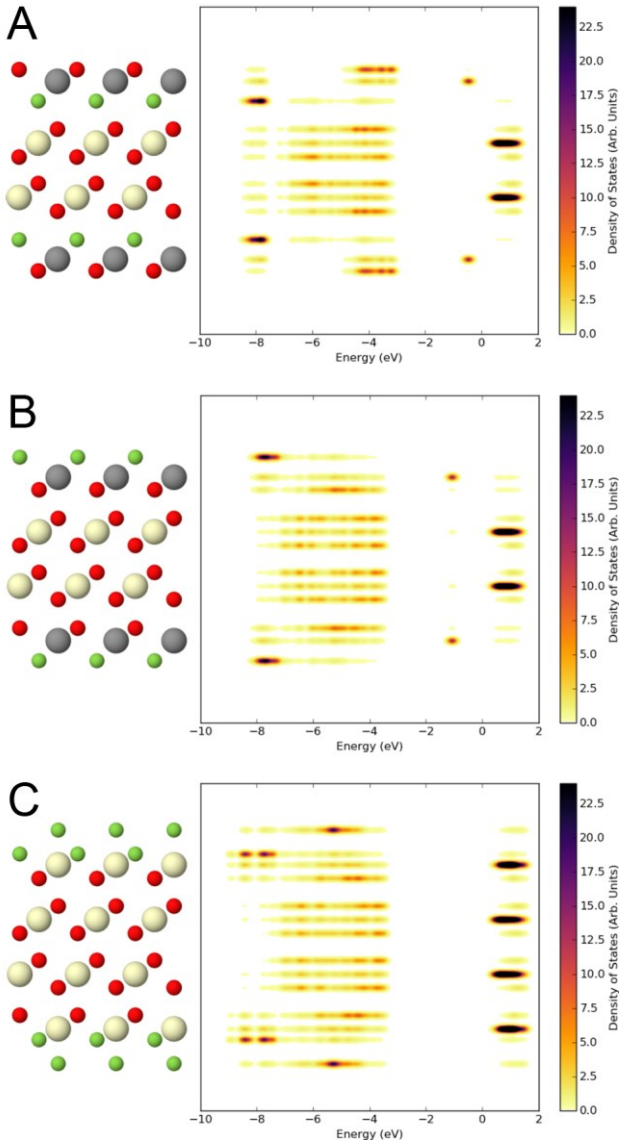

Figure 25: Calculated projected densities of states (PDOS) of the fluorine doped ceria(111) structures considered herein. Ce^{4+} and Ce^{3+} are represented by large cream and grey colored spheres, while O and F ions are represented by red and green colored spheres, respectively. Densities in PDOS are vertically separated, each line corresponds to contributions from atoms in the respective layer depicted on the left. The darker the color, the higher the PDOS density. Detailed description of the considered structures (A) – (C) can be found in the text.

The calculated density of states of the subsurface fluorine reveals another interesting effect, namely that the O 2*p* states of the oxygen atoms in the surface contract and shift to lower binding energies. This can be rationalized as the effect of the exclusive presence of fluorine induced Ce^{3+} ions in their vicinity, which reduces hybridization between cerium and oxygen atoms. One could easily jump to the conclusion that this corresponds to the new states at the top of the O 2*p* band in the measured photoemission spectra of $Ce^{4+}_{0.55}Ce^{3+}_{0.45}O^{2-}_{1.37}F^{1-}_{0.80}$, however, there are several reasons why such a conclusion would be inconsistent with the results presented here. First, subsurface fluorine is energetically less favorable than surface fluorine [71],

[131]. Second, we do not observe the gap between F 2*p* and O 2*p* states in the experiment. And, most importantly, the interatomic nature of the resonant photoemission process at the Ce $4d \rightarrow 4f$ photoabsorption threshold of Ce^{3+} ions, the ones bonded to the surface oxygen atoms, will be solely comprised of the $f - f$ interaction decay channel, disregarding any surrounding 2*p* electrons [45]. This means that the structure we are looking for has to have Ce^{4+} atoms in the vicinity of any such electrons as would give rise to the new states. Interestingly, our recent theoretical work on fluorine impurities at $CeO_2(111)$ surface suggests a candidate that would satisfy the condition [131]. The structure consists of a fluorine atom in the surface and an additional fluorine atom adsorbed on top of a cerium lattice site. The presence of two fluorine atoms per one surface oxygen atom leaves no excess electron to be localized on the Ce^{4+} ion, which therefore maintains its nominal 4+ oxidation state. The calculated density of states for this configuration is shown in Figure 25, panel C. We see that the F 2*p* states of the adsorbed F^- ion shift markedly to lower binding energies, to the extent that they appear at the top of the O 2*p* band. A concurrent increase in density of states is also visible on the surface cerium atoms, which suggests a degree of covalent bonding between the two. We put this configuration forward as the origin of the observed emergent states on $Ce^{4+}_{0.55}Ce^{3+}_{0.45}O^{2-}_{1.37}F^{1-}_{0.80}$.

Our combined experimental and theoretical results expose the flexibility fluorine doping offers for modification of ceria based chemistry. The effects extend beyond the direct increase of *f* electron density (without hampering reducibility of ceria at low concentration)[112] and allow tailoring of 2*p* mediated interactions beyond the O 2*p* band. The controlled modification of the density of states at the bottom and below the O 2*p* band facilitates enhanced alignment with several relevant molecules, specific examples of which are water (characteristic $1b_1$ and $3a_1$ states at 6.9 eV and 9.5 eV, respectively), methanol, ethanol and OH^- (3σ orbitals at 9.8 eV) [113], [151], [152]. The emergent states at the top of the O 2*p* band offer possibilities for alteration of interaction with *d* states of metals that are commonly supported on ceria, such as Cu, Ni and Pt [153], [154].

In summary, we have presented a detailed study of the effect of substitutional fluoride anions in ceria on the valence band density of states. We find that an interplay between concentration of oxygen vacancies and fluorine dopants influences depth distribution of the latter. We show that the location of fluorine determines its contribution to the valence band density of states. Consequently, we demonstrate that the (111) surface of ceria, which is lowest in energy and therefore most prevalent, exhibits capability to support fluorine in a distinct adsorbed position, that has a marked effect on the energy of the corresponding F 2*p* states. This electronic structure is distinct and unique to the anion incorporation. The results illustrate the importance of understanding the effect of fluorine doping in ceria, be it through contamination or rational design, and allow us to propose anion doping as a viable tool for valence band engineering in oxide based chemistry.

3.3.4. Experimental section

Resonant photo-electron spectroscopy (RPES) experiments were conducted in an ultrahigh vacuum system at the Materials Science Beamline at Synchrotron Elettra (Trieste, Italy). The system has a base pressure of 1×10^{-8} Pa and features LEED optics, a dual Mg/Al anode X-ray source, electron energy analyzer (SPECS) and other sample cleaning and preparation techniques. The substrate was a Rh(111)

single crystal (MaTecK) which was first cleaned by Ar^+ bombardment and annealing in 5×10^{-5} Pa of O_2 (Linde 4.5). Ce (Goodfellow) was evaporated from tantalum crucibles heated by electron bombardment in the background atmosphere of O_2 (Linde, 4.5) for the growth of undoped samples. Fluorine doped samples were prepared utilizing a separate evaporator of the same construction which was loaded with a Ce (Alfa Aesar 99.9%) that was preexposed to HF vapor for 60 min at 90°C. The ceria films were grown at room temperature in 5×10^{-5} Pa of O_2 and their fluorine doping level was controlled by alternating deposition of fluorine doped and undoped ceria in several steps. The prepared films were annealed to 250°C in 5×10^{-5} Pa of O_2 and checked by LEED for the characteristic hexagonal diffraction pattern of the (111) surface termination. The thickness of the films was determined to be 9 ML from the attenuation of the Rh 3*d* signal. Photoelectron spectroscopy of the Ce 3*d*, F 1*s*, O 1*s* and Rh 3*d* core levels was performed with X-ray radiation of 1253.6 eV (Mg Kα), and valence band spectra were measured with synchrotron radiation in the range of 115-125 eV. The presented Ce 3*d* spectra have been processed in order to remove the satellite peaks using procedures implemented in CASA XPS and then deconvoluted into Ce^{4+}, Ce^{3+} and Ce-F doublets. The stoichiometry of the samples was calculated from the Ce^{4+}/Ce^{3+} and O/F ratios according to the charge neutrality principle. The detailed description of the applied fitting procedure can be found in Ref. [104].

Density functional theory calculations were carried out using the projector augmented wave method [155], as implemented in the Vienna Ab-initio Simulation Package [156]–[158], version 5.3.5. We use the HSE06 hybrid functional [159], which has been applied to ceria [160]. The projector augmented wave (PAW) potentials used were the standard Perdrew-Burke-Ernzerhof (PBE) potentials distributed with this version of Vienna Ab initio Simulation Package (VASP), which incorporate the [Xe] $4d^{10}$ electrons of Ce atoms and the 1*s* electrons of the O and F atoms into the core. A plane-wave cut off energy of 400 eV was used.

The structural model comprised a slab of 12 atomic layers (for the stoichiometric slab), with a $p(1 \times 1)$ surface unit cell. A $4 \times 4 \times 1$, Γ centered *k*-point mesh was used, automatically generated according to the Monkhurst-Pack scheme. A vacuum gap corresponding to 15 atomic layers of bulk ceria was used. The addition of fluorine to the slab was performed symmetrically with respect to the top and bottom surface of the slab, in order to avoid the formation of a dipole across it. The projected densities of states images were generated by taking the coefficients of the Kohn-Sham eigenstates projected using the PAW, and convolving them with Gaussian functions of 0.1 eV in energy and 0.1 Å in space. The images themselves were generated with the matplotlib.pyplot Python module [161]. The colormap was the perceptually uniform "inferno" map, reversed.

3.4. Epitaxial growth of CeO_2(110) on Rh(110)

3.4.1. Preface

Up till now, all the presented results were obtained on polycrystalline or (111) ordered cerium oxide. Even though the (111) facet is considered as the most stable [162], [163], its catalytic activity should be lower in comparison with differently ordered terminations [35]–[37]. Therefore, defined preparation and investigation of these stable yet more reactive facets is of interest.

This prompted us to try to prepare the CeO_2(110) by epitaxial growth on Rh(110). The choice for CeO_2(110) was quite straightforward, because it should be the second most stable facet [162], which possesses the highest OSC [36]. However, such ordered system has yet been prepared only in the form of nanorods [111]. For any surface science research, it would be much more convenient to be able to prepare such termination in situ as a flat continuous layer.

From this chapter on, the presented results are less than one year old, and thus none of the results have been published so far.

3.4.2. Experimental section

LEED and TPR experiments were carried out in an ultrahigh vacuum system described thoroughly in section 2.8.1. The Rh(110) single crystal (MaTecK) was cleaned by Ar^+ ion sputtering, subsequent annealing to 650°C in 5×10^{-5} Pa of O_2 (Linde 4.5), and annealing to 500°C in CO (Alphagaz 4.5). The adsorbed CO was then removed by flash annealing to 500°C.

The CeO_2 layers were deposited by evaporating Ce metal (Goodfellow 99.99%) in oxygen atmosphere of 5×10^{-5} Pa. In case of Ce deposition at elevated temperature, the sample was cooled down in oxygen stream to 150°C. On the other hand, the ceria layer deposited at room temperature was subsequently annealed for 10 min in 5×10^{-5} Pa of O_2 to 650°C.

The testing of continuity of prepared ceria layers was conducted by two cycles of CO adsorption at room temperature followed by TDS to 500°C. The area under the TDS curve then represents the amount of adsorption positions for CO, which can be found, at these pressures and temperatures, only on Rh(110) surface.

3.4.3. Results

In order to achieve the epitaxial growth of a material, the basic unit cell dimensions of the substrate and the deposited material may not significantly differ. For ceria, these parameters are adequate for wide range of metallic substrates such as Cu, Rh, or Ru. The epitaxial growth of CeO_2(111) on these Cu(111), Rh(111), and Ru(0001) surfaces was mastered and repeatedly applied in many surface science studies [38], [52], [164], [165]. Such growth is possible due to convenient dimensions of lattice constants of these materials. The surface lattice constant of Cu(111), Rh(111), and Ru(0001) are 2.56 Å, 2.69 Å, and 2.70 Å, respectively, while the surface lattice constant of CeO_2(111) is 3.83 Å. Calculating the misfit m according to:

$$m = |a_s - a_d|/a_s \tag{21}$$

where the a_s and a_d denote the lattice constants of substrate and deposit, respectively, the misfit for substrate to deposit 3 : 2 growth reaches 0, 5, and 5 % for Cu(111), Rh(111), and Ru(0001). However, even on the virtually perfect Cu(111) substrate, the deposited layers do not match precisely because the lattice constant of ceria changes with the thickness of the deposited layer [48], [50]. The values reported by Mašek et al. for 1 ML thick layer of CeO_2 reach the lattice constant value of 5.15 Å. In such case, the lattice parameter for (111) facet is 3.64 Å, which would increase the lattice mismatch to 5, 10, and 10 % for Cu(111), Rh(111), and Ru(0001). Actually, for the last two substrates, the 4 : 3 growth would provide much lesser lattice mismatches, namely only 1 %, while for the Cu(111), this setup would give 7 % mismatch.

In light of the previous analysis, the elementary unit of surface of Rh(110) has its basic dimensions 3.80 × 2.69 Å, while the CeO_2(110) has its size 3.82 × 5.41 Å or 3.64 × 5.15 Å using the bulk or 1 ML layer lattice parameters, respectively. Therefore, the correspondence between the dimensions of two Rh(110) basic cells 3.80 × 5.38 Å and one ceria cell give 1 % or 4 % mismatch in case of bulk or 1 ML layer lattice constants, respectively. Hence, Rh(110) seems to be almost perfect substrate for an epitaxial growth of CeO_2(110) layers. The illustration of this growth is depicted in Figure 26 - A. It is clear that in this configuration, the rows of Rh(110) will be perpendicular to the rows of CeO_2(110), i.e. [-110] CeO_2(110) ⊥ [-110] Rh(110).

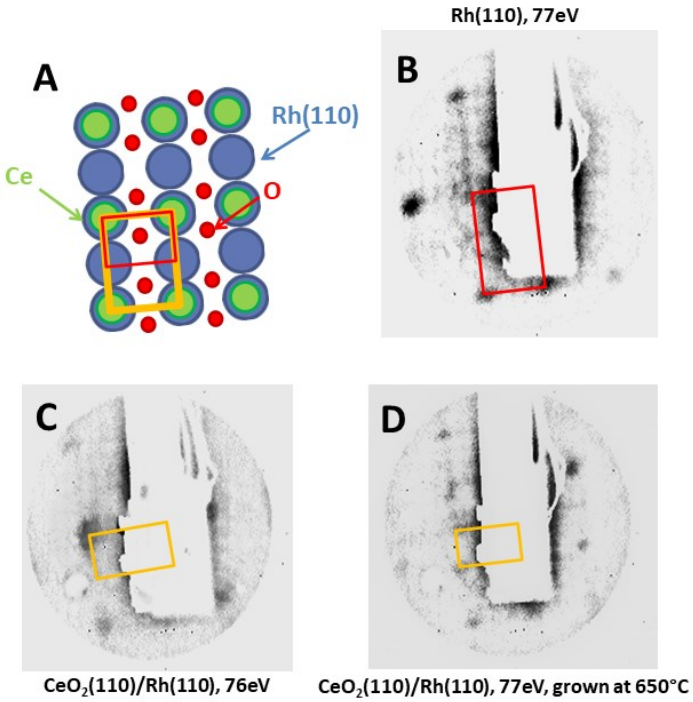

Figure 26: (A) Model of epitaxial growth of CeO_2(110) on Rh(110). (B) Rh(110), 77eV. (C) 2 nm of CeO_2(110)/Rh(110) annealed to 650°C after the deposition, 76eV. (D) 2 nm of CeO_2(110)/Rh(110) prepared at 650°C, 77eV.

By comparing the diffractograms in Figure 26 – B and C, we observe no obvious change even though the attenuation of the Rh(110) signal and the growth of the Ce 3*d* XPS signal hint that the substrate is covered with ca. 2 nm of ceria. Therefore, we have checked the substrate coverage by CO adsorption and desorption experiments. The results presented in Figure 27 (red line) show no CO desorption peak for this sample, so we can conclude that the prepared CeO_2(110) is continuous.

However, according to model in Figure 26 – A, we should be able to observe a (1 × 2) reconstruction with respect to Rh(110) structure. Thus, we cleaned the Rh(110) substrate and tried to prepare the ceria layer at temperature 650°C. The elevated temperature should improve the ordering of the deposited layer, however, such layer do not have to maintain its continuity. The resulting diffractogram and the CO desorption peak are shown in Figure 26 – D and Figure 27 (green line), respectively. The presence of the middle spot in Figure 26 – D gives clear evidence that the prepared layers are CeO_2(110) perpendicularly ordered with respect to Rh(110) substrate. Unfortunately, these highly ordered layers are not continuous as is obvious from the desorption peak in Figure 27 (green line). Nevertheless, by comparing the CO desorption signal intensities, the Rh(110) on this 650°C-prepared

CeO_2(110)/Rh(110) sample exposes only approx. 10% of the total area. Since the majority of the LEED signal comes still from the ordered ceria layer, it is unlikely that the (1 × 2) reconstruction is created by any adsorbate reconstruction on the Rh(110) substrate.

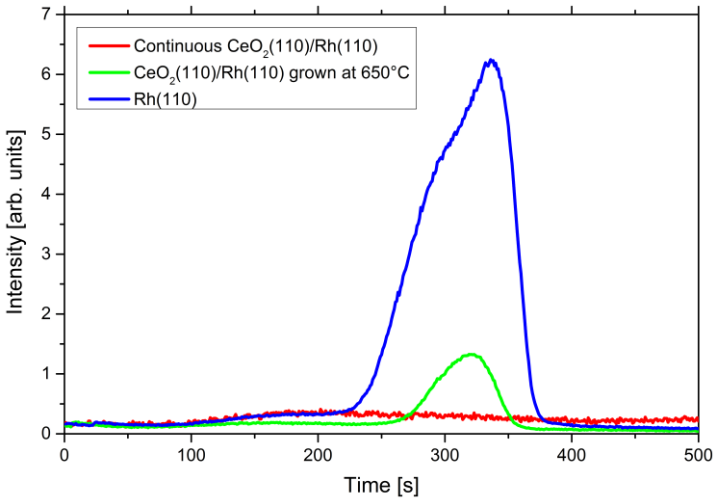

Figure 27: Comparison of CO desorption peaks from various samples.

3.4.4. Conclusion

In conclusion, we have shown that ceria grows on Rh(110) in the form of ordered CeO_2(110) layers. The rows of CeO_2(110) are perpendicular to the rows of Rh(110), i.e. [-110] CeO_2(110) ⊥ [-110] Rh(110). The growth of 2 nm thick ceria layers at room temperature followed by annealing to 650°C yields continuous layers with slightly worse ordering than in the case of layers prepared at 650°C. However, the CeO_2(110) layer prepared at 650°C was discontinuous, exposing ca. 10% of the Rh(110) substrate.

From our results follows that it is possible to prepare well ordered CeO_2(110) layers on Rh(110) substrate which can be used for various surface science experiments. Because the (110) facet is the second most stable facet of ceria, which is much more reactive than the well known (111) plane, this possibility broadens the capabilities to prepare and investigate different defined surface terminations of ceria in situ.

3.5. ^{18}O and ^{16}O Oxygen Exchange on Model Rh/CeOx(Fy) Systems

3.5.1. Preface

The results and gained knowledge opened us doors for more complex studies in which cerium oxide will play a role of a substrate for the deposited metal. In this setup, we abandon the idea of an inverse catalyst and move toward a more realistic configuration similar to one used in commercial catalytic converters. However, we will maintain the model approach by controlled preparation of cerium oxide layers by epitaxial growth on Rh(111) and Rh(110) single crystals.

One of our earliest goals was to be able to compare and visualize the OSC phenomenon of different substrates directly. This effort had been unfortunately hampered by two facts. Firstly, the oxygen adsorbed on Rh has the same binding energy as the oxygen bonded in ceria. Therefore, the OSC cannot be observed

directly by XPS or SRPES. Secondly, as has been already explained in section 3.2.6, the surface of Rh has higher oxygen capacity than 1 ML of ceria, so any CO oxidation reaction yields give information about the coverage rather than the OSC. Since ceria by itself is not catalytically active, we have had to design the experiment in such way that we would be able to discriminate the oxygen in ceria and the oxygen adsorbed on rhodium.

The easiest solution was to exploit the possibilities of isotopically labeled gases in combination with the TPR method. The plan was to prepare the ceria and cerium oxyfluoride layers using the usual $^{16}O_2$. It was essential to use the conventional oxygen for the preparation because the source ceria metal is usually oxidized to some extent and this oxygen is released during the evaporation procedure. In order to avoid any remnants of adsorbed ^{16}O on Rh, the layer had to be continuous. Afterwards, as the active metal, rhodium was evaporated on the ordered layer in desired amount. All the following exposures of the sample had to contain only the isotopically labeled oxygen, so that all the ^{16}O observed by the QMS must have come from the cerium oxide layer.

In order to be able to use the isotopically labeled gases repeatedly, the gas introduction system on the XPS/TPR/LEED system had to be improved. The $^{18}O_2$ and $^{13}C^{18}O$ gases were bought and attached to the system permanently, each with its own precision leak valve.

The utilization of complex model systems in combination with the isotopically labeled gases broadens our possibilities in observation of previously inaccessible mechanisms in heterogeneous catalysis such as oxygen exchange, or oxygen spillover. In this chapter, the newest results obtained on NAP-XPS and XPS/TPR/LEED will be presented. Besides the direct comparison of OSCs of various samples, we will focus also on hydrogen oxidation reaction.

Cerium oxides are, among other uses, employed in PEMFC as an anode catalyst. Pt^{2+} deposited on the ceria was long considered as the active element responsible for high specific power of the used catalysts [84]. Nevertheless, it has been recently shown that the Pt^{2+} plays no role in hydrogen dissociation [166]. However, the still unconsidered fact is the ceria contamination with fluorine, which is inevitably present due to fluorine migration from the fluorine-containing membrane – see section 1.4. Therefore, our secondary objective was to elucidate the effect of fluorine in ceria on the hydrogen dissociation capability.

3.5.2. Experimental section

The experiments were conducted in two experimental systems, XPS/TPR/LEED and NAP-XPS, described in detail in chapters 2.8.1 and 2.8.3. Additionally, the samples prepared for NAP-XPS measurements in XPS/TPR/LEED apparatus were investigated with AFM prior and after the NAP-XPS measurements.

In total, four samples were prepared for both measurements. $Rh/CeO_2(111)/Rh(111)$, Rh/CeOxFy(111)/Rh(111), $Rh/CeO_2(110)/Rh(110)$, and Rh/CeOxFy(110)/Rh(110) samples were prepared by deposition of fluorine-free or fluorine-doped ceria on rhodium single crystals. The continuous $CeO_2(111)$ and $CeO_2(110)$ layers were prepared by evaporation in 5×10^{-5} Pa of $^{16}O_2$ at 250°C or 350°C, respectively. The continuous CeOxFy(111) and CeOxFy(110) layers for the experiments in XPS/TPR/LEED were prepared in 5×10^{-5} Pa of $^{16}O_2$ at 400°C. The CeOxFy(110) layer was afterwards annealed to 600°C for 15 minutes. However, the continuous CeOxFy(111) and CeOxFy(110) layers for experiments in NAP-XPS

were prepared at 350°C and 25-600°C, respectively. The fluorine doped layers were prepared in several steps which ensured that the fluorine to oxygen ratio will be lower than one. The maximal temperature in each preparation step of CeOxFy(110) for NAP-XPS differed in range 25-600°C. By increasing the temperature during the growth, the exchange of fluorine for oxygen is enhanced in the growing cerium oxide layer. Therefore, the maximal temperature was determined by the doping level of the source material in the evaporator as well as by the measured ratio of fluorine to oxygen in the layer. In order to prepare thin and continuous layers, the sample temperature during the growth of fluorine-doped layers started always at room temperature, which the sample was held at for 15 minutes. Then the temperature was ramped to its maximum value (mentioned above) at rate 10°C/min. In this way, prepared layers should achieve better continuity [47].

Keeping the fluorine to oxygen ratio lower than one should ensure that the prepared layers maintain the cubic structure. The content of fluorine in the prepared cerium oxyfluoride layers was around 30% or 40% for the oxygen exchange experiment samples and for the NAP-XPS samples, respectively. The orientation and continuity of all prepared layers was checked by LEED measurement. Additionally, the ceria films for oxygen exchange experiments were checked for continuity by CO adsorption and TPD. Thicknesses of the prepared CeOx(Fy) layers ranged from 10 to 20 monolayers.

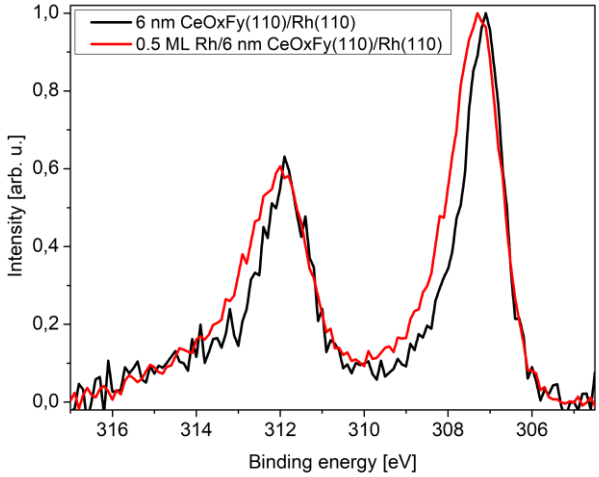

Figure 28: EMSI effect observed on Rh particles deposited on 6 nm thick CeOxFy(110). The samples maintained their O 1*s* binding energy of 529.8 eV.

On top of these ordered cerium oxide layers, Rh was deposited by physical vapor deposition from Rh wire (Goodfellow 99.9%). The amount of deposited material was in range 0.4 to 0.8 ML. The prepared Rh showed the effects of Electronic Metal-Support Interaction (EMSI) – see Figure 28. Surprisingly, even the partially reduced CeOxFy layers showed positive charging of deposited Rh, which was in the case of fluorine-free ceria observed only for fully oxidized supports [66]. Concurrently, we observed slight reduction of the Ce 3*d* spectrum after the Rh depostition. The samples showed no signs of charging effects. The binding energy of lattice oxygen remained at 529.8 eV.

3.5.3. Results – Oxygen Exchange

The ceria layers can be reduced via oxygen back-spillover during the reducing reactions on Rh particles, by deposition of metallic cerium [38], or solely by

annealing to high temperatures [47], [52]. According to Dvořák et al. [47], the advent of oxygen vacancies starts already at temperatures exceeding the temperature during the preparation of the layer. On the other hand, Eck et al. showed the appearance of ordered vacancies in (3 × 3), (√7 × √7)R19.1°, and (4 × 4) reconstructions upon annealing 5-13 nm thick ceria layers to temperatures above 650°C [52]. In order to evaluate this contribution of thermally released ^{16}O to the total amount of ^{16}O released during the reaction of samples with $^{13}C^{18}O$, we have exposed the samples with $^{18}O_2$ and monitored the oxygen exchange rate. The results for exposure of CeOx(Fy) and Rh/CeOx(Fy) are showed in Figure 29. Surprisingly, we were not able to detect any signs of oxygen exchange, which would be observable as a peak in signal of $^{16}O_2$ or $^{16}O^{18}O$. The same results were measured during the exposures up to 650°C.

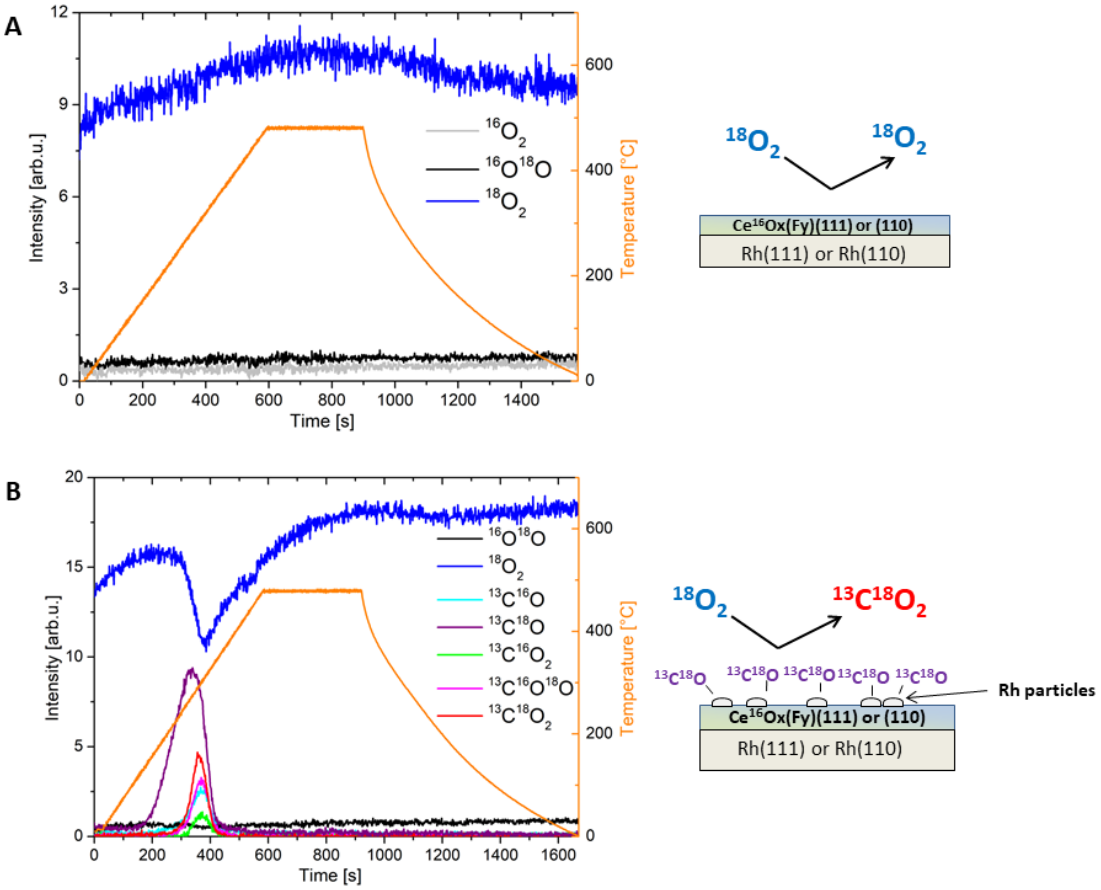

Figure 29: (A) QMS signal during the exposure of ordered CeOx(Fy) layers with $^{18}O_2$. (B) QMS signal during the exposure of Rh/CeOx(Fy) samples with $^{18}O_2$. The samples were preexposed with $^{13}C^{18}O$.

The explanation of these observations has to consider three important facts. Firstly, the annealing up to 650°C was in this case conducted effectively in 2.7×10^{-6} Pa of $^{18}O_2$. Therefore the discrepancy with respect to results published in [47] can be accounted for either different substrate or distinctive oxygen chemical potential which had been recently shown to play substantial role in growth of ceria [167]. Higher partial pressure of oxygen can also explain the lack of tendency to create oxygen vacancies even at temperatures as high as 650°C.

However, the data in Figure 29 – B reveal one more interesting thing. As it is evident, the oxygen back-spillover plays a role in CO oxidation reaction on Rh particles. Nevertheless, except from the expected $^{13}C^{16}O^{18}O$, we can also see the

production of $^{13}C^{16}O_2$, which gives evidence of partial dissociation of $^{13}C^{18}O$ on Rh particles.

In contrast to situation during the exposure with $^{18}O_2$, we observed a massive oxygen exchange during the exposure of ordered Rh/CeOx(Fy) with $^{13}C^{18}O$ – see Figure 30. This phenomenon clearly would not be observable without the usage of isotopically labeled CO. Except from the CO oxidation reaction, we can see a decrease in signal of $^{13}C^{18}O$ and a coincident increase in observed intensity of $^{13}C^{16}O$.

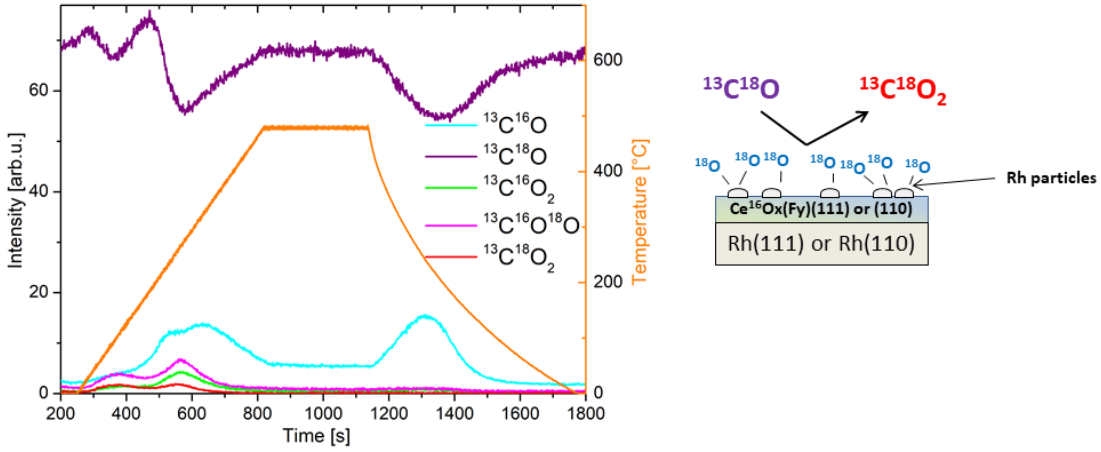

Figure 30: QMS signal during the $^{13}C^{18}O$ exposure of Rh/CeOx(Fy) layers. The samples were preexposed with $^{18}O_2$.

In principle, there are three possible mechanisms for the oxygen exchange during the CO exposure, which are schematically demonstrated in Figure 31. In the first possibility (Figure 31 – A), the oxygen exchange takes place on the Rh particle due to continuous back-spillover of ^{16}O. In such case, however, there would be no reason for stopping of CO_2 production. In contrast, we see that the second oxygen exchange maximum at time 1300 s (Figure 30) occurs without any significant amount of produced CO_2. Moreover, ceria substrate is, in this case, already fully reduced after providing all the accessible oxygen during the annealing. Therefore, this mechanism can be apparently excluded.

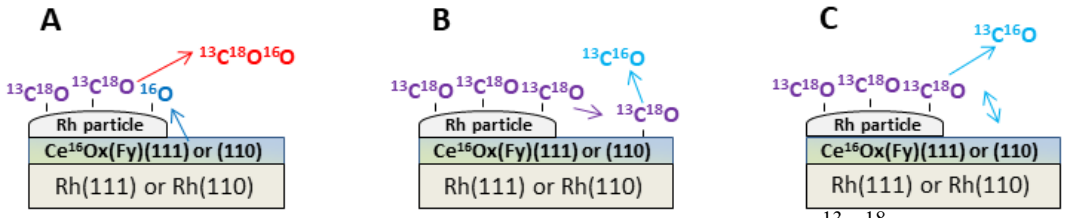

Figure 31: Possible explanations of oxygen exchange during the $^{13}C^{18}O$ exposure.

The second possibility (Figure 31 – B) illustrates that the adsorbed $^{13}C^{18}O$ diffuses on top of ceria. We recall that CO cannot adsorb directly on ceria at these conditions; however, migration of carbon or carbon monoxide from Rh particles to ceria cannot be fully excluded. Nevertheless, such carbon monoxide which would reside on top of ceria waiting for the chance to swap oxygen and desorb would have to be observable by XPS as an increased intensity of C 1*s* signal. After checking our data we were not able to see any signs of increased carbon intensity, rather the other way round. The amount of adsorbed CO correlates linearly with the coverage of the Rh substrate. For these reasons, we can most probably rule out also the second mechanism (Figure 31 – B).

However, these contemplations left us with the only remaining possibility depicted in Figure 31 – C. So, we can conclude that the oxygen exchange takes place at the interface of Rh particles and ceria. Nonetheless, this leaves us one more question to answer. What actually happens with the ^{18}O after the oxygen exchange? Since the exchange occurs also after ceria is reduced, the most straightforward answer is that ^{18}O incorporates into ceria instead of the released ^{16}O. However, one more mechanism plays a significant role in the observed behavior – oxygen migration in ceria. The reaction would quickly diminish were it to have only the oxygen at the interface available for the exchange. Hence, ^{18}O has to be quickly diluted in all other oxygen in ceria. Either this or the fact that $^{13}C^{18}O$ is not able to overcome the barrier for the oxygen exchange stand behind the diminishing of the exchange at temperatures below 150°C (see Figure 30). This means that the oxygen diffusion at temperatures above 150°C has to be facile enough to take all ^{18}O away from the interface. These findings correlate well with the observed back-spillover of oxygen from ceria to Rh which starts at temperatures above 125°C [68].

On the other side of the oxygen exchange maximum, the temperature starts to be too high. Even though the speed of oxygen migration in ceria is high enough, the oxygen exchange intensity declines due to change in CO adsorption probability. As the temperature rises, the surface residence time is lower and the majority of CO immediately leaves the surface.

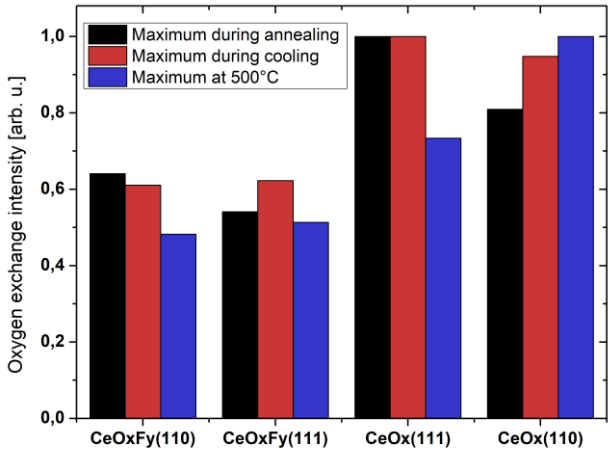

Figure 32: The comparison of oxygen exchange rates. Values of each type of measurement (black, red, blue columns) were normalized independently to 1.

In fact, we have witnessed the consequences of the interfacial oxygen exchange. In Figure 32, we can see the comparison of oxygen exchange rates for the prepared samples. The columns represent the average $^{13}C^{16}O$ desorption rate (measured at the maxima and at 500°C) normalized to the amount of deposited Rh on cerium oxide layers. The data show that the oxygen exchange rate is approximately 30% lower in the case of fluorine-doped samples. The amount of fluorine in the prepared CeOxFy layers was also ca. 30% (see Section 3.5.2). Therefore, it is conceivable that fluorine blocks the positions at the interface with ceria, and thus hinders the exchange of oxygen at these spots (see Figure 33).

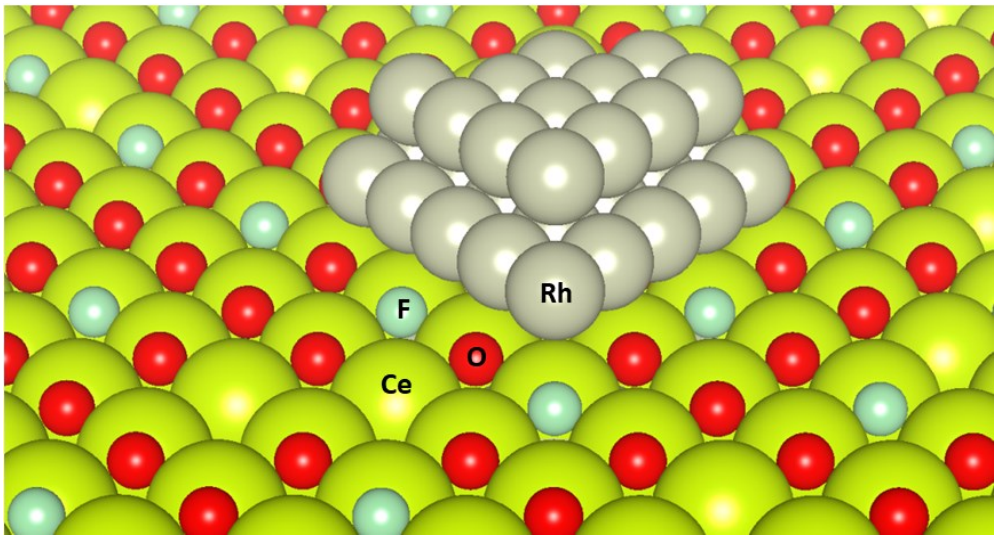

Figure 33: Model of a Rh particle on the surface of CeOxFy(111) layer. Fluorine atoms substitute for oxygen in CeOxFy and partially block the oxygen exchange at the interface.

3.5.4. Results – Oxygen Storage Capacities

In order to compare the OSCs of different samples, the samples were exposed in several steps to $^{13}C^{18}O$ and $^{18}O_2$ gases. During the $^{13}C^{18}O$ exposure, the sample was exposed to 4 L at room temperature, then the temperature was ramped to 500°C at rate of 1°C/s and the sample was exposed to another 6 L at 500°C. Afterwards, the sample was, still in the CO stream, cooled down to room temperature. During the $^{18}O_2$ exposure, the sample was immediately annealed in $^{18}O_2$ to 500°C at rate of 1°C per second and exposed to 6 L at 500°C. Both exposure procedures are depicted in Figure 29 and Figure 30.

However, the plan to count simply all the ^{16}O desorbing from the layer was again hampered by the observed oxygen exchange during the $^{13}C^{18}O$ exposure. Therefore, we have integrated only the areas of produced $^{13}C^{16}O^{18}O$ and $^{13}C^{16}O_2$, which are related to the oxygen back-spillover rates and CO oxidation reaction rates. The average values obtained for each sample are depicted in Figure 34 (black columns). Even though it is highly probable that the CO molecule quickly desorbs after the oxygen exchange, we cannot omit the possibility that some of the $^{13}C^{16}O$ sticks to the surface long enough to react with another oxygen and desorb as CO_2. Moreover, the limited number of experiments created large margin of error of the obtained data.

Therefore, we calculated also the ^{16}O released during the $^{18}O_2$ exposure – see Figure 34 (red columns). These values are not influenced by the oxygen exchange and tell us about the oxygen back-spillover rate on the samples. Since cerium oxide can be reoxidized either by oxygen spillover from Rh particles to cerium oxide [67], or by direct interaction with molecular oxygen even at room temperature [168], the reoxidation of ceria is faster than CO desorption from Rh particles. The observed ^{16}O in CO and CO_2 thus comes either from $^{13}C^{16}O$ which remained on the surface after the oxygen exchange (in the previous $^{13}C^{18}O$ exposure step), or from the oxygen back-spillover. However, in the beginning of annealing in $^{18}O_2$, we do not observe any desorption of $^{13}C^{16}O$, only the $^{13}C^{18}O$ (see Figure 29 – B). This proves that the oxygen exchange process stops at higher temperature than the CO desorption. Therefore, the Rh particles are initially covered only with $^{13}C^{18}O$ and, for this reason,

all ^{16}O observed during the $^{18}O_2$ exposure comes from oxygen back-spillover. Since there are two contradictory mechanisms – the $^{13}C^{18}O$ desorption and $^{13}C^{18}O$ reaction with released ^{16}O, we obtain higher ^{16}O content on samples with quicker back-spillover process or, in other words, samples with lower back-spillover activation energy. Nevertheless, this value naturally coincides with the OSC of the sample because, when the layers reduce, their back-spillover activation energy grows. Consequently, the lower the back-spillover activation energy for fully oxidized layer is, the higher is the total OSC.

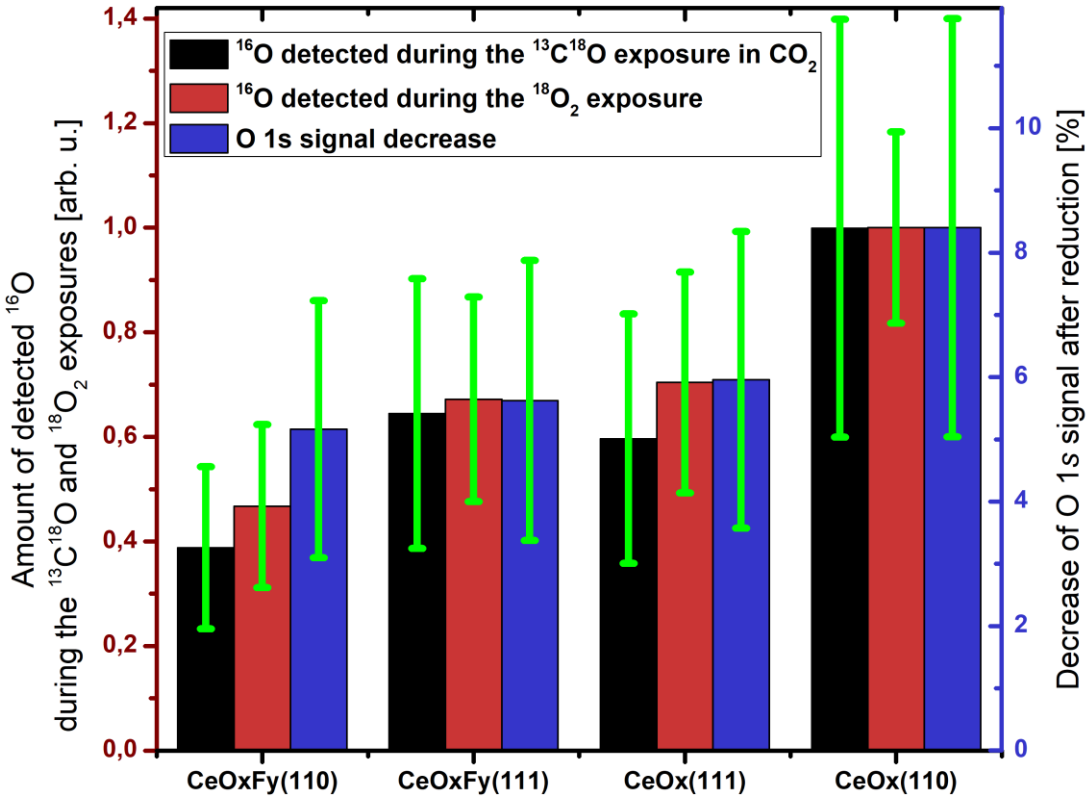

Figure 34: Average amount of ^{16}O detected in $^{13}C^{16}O^{18}O$ and $^{13}C^{16}O_2$ during the $^{13}C^{18}O$ exposure (black columns); Average amount of detected ^{16}O during the $^{18}O_2$ exposure (red columns); Average decrease of O 1*s* area after depletion of oxygen from the cerium oxide layers due to CO oxidation reaction (blue columns).

In order to be absolutely sure about the obtained OSC, we compared the previous results with the average decrease of O 1*s* signal after the CO oxidation reactions – see Figure 34 (blue columns).

The presented results from the three independent methods are all related to the overall OSC of the samples. In Figure 34, we can see that these values are well correlated; however, the values largely differ for various samples. The highest OSC is observed for the CeOx(110) layer, while fluorine-doped CeOxFy(110) layer shows massive decrease in OSC. Surprisingly, fluorine doping of (111) ordered layers does not cause any significant deterioration of OSC, which is in agreement with our previous results [112] (see Section 3.2). This might be caused by different interaction of ceria supports with rhodium particles. Fluorine might be prone to block the interfacial positions, and thus hinder the reduction of fluorine-doped layers with (110) orientation. Another effect where different surface orientation plays a significant role is the expelling of fluorine to adsorbate positions [131] (see also

Section 3.3). It is plausible that this mechanism largely differs on (111) and (110) surface terminations, and, in this way, causes the observed disparity.

3.5.5. Results – Hydrogen Oxidation Reaction

In attempt to evaluate the effect of fluorine doping to hydrogen dissociation, we stood before a question, whether we are able to follow any products of the hydrogen dissociation reaction via QMS or observe some changes in XPS spectra. We have proven that interaction of hydrogen in UHV condition with thick layer of ceria does not induce any changes observable by XPS. Therefore, the presence of an active metal which activates hydrogen by adsorption and dissociation is a necessity for any observable chemical changes [166], [169]. Atomic hydrogen then migrates on top of ceria, where it creates hydroxyl groups [170]. When such hydroxyl groups interact with atomic hydrogen or with each other, water is produced.

Nevertheless, in case of cerium oxyfluoride, the QMS signal for water can mix with the signal of hydrogen fluoride desorbing from the layer. In order to be able to differentiate between these two signals, we have deliberately exchanged some ^{16}O for ^{18}O in the ceria layer. Despite low intensity of signals, we were able to confirm desorption of water from ceria and cerium oxyfluoride – see Figure 35.

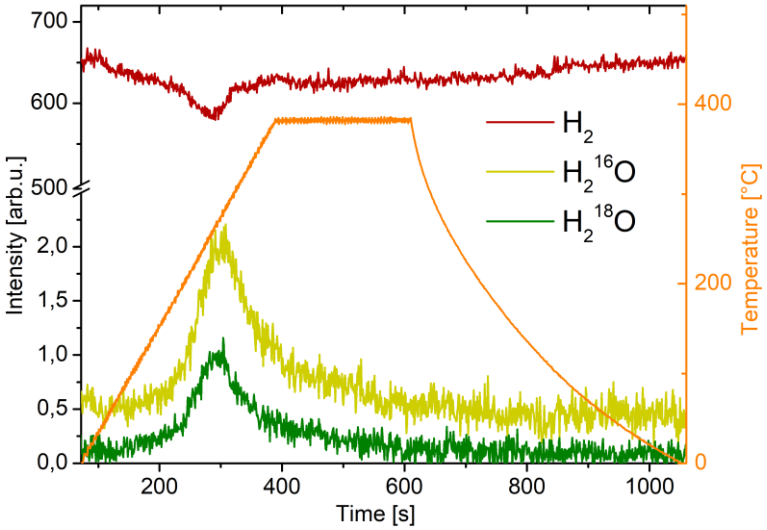

Figure 35: Water desorption during exposure of Rh/CeOxFy(110) sample with H_2 to 400°C. ^{16}O in the CeOxFy layer was partially exchanged for ^{18}O.

We were also able to confirm that the reaction proceeds via adsorbed OH groups – see Figure 36. The reaction naturally stops when ceria becomes reduced and energy needed for desorption of another water molecule exceeds the sum of energies of the interacting reactant molecules. Therefore, after the reaction, OH groups remain firmly bond to the surface, which is the most stable surface configuration [131].

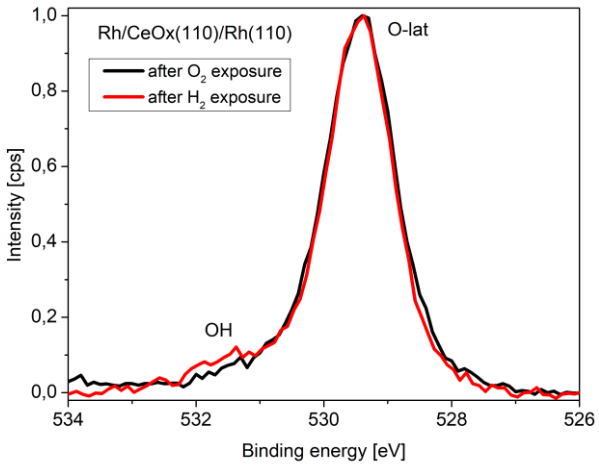

Figure 36: O 1*s* spectra before and after the H_2 exposure to 500°C.

Even though the overall water production can be used to analyze the OSC of different substrates (see Figure 37 – wine columns), which gives results comparable to those presented in Section 3.5.4, these values are not closely related to the rate of hydrogen dissociation or hydrogen oxidation reaction. We may get little closer to the hydrogen oxidation reaction rate by comparing the temperatures of water desorption maxima (Figure 37 – blue columns). These values are related to the strength of the bond of OH groups to the surface of cerium oxide. In fact, these measurements give us valuable information about the conditions which we have to set in order to observe the rate limiting step in hydrogen oxidation reaction. According to Feng et al., the rate limiting step is the electron transfer between cerium cations and hydroxyl ions [115] (see Figure 38).

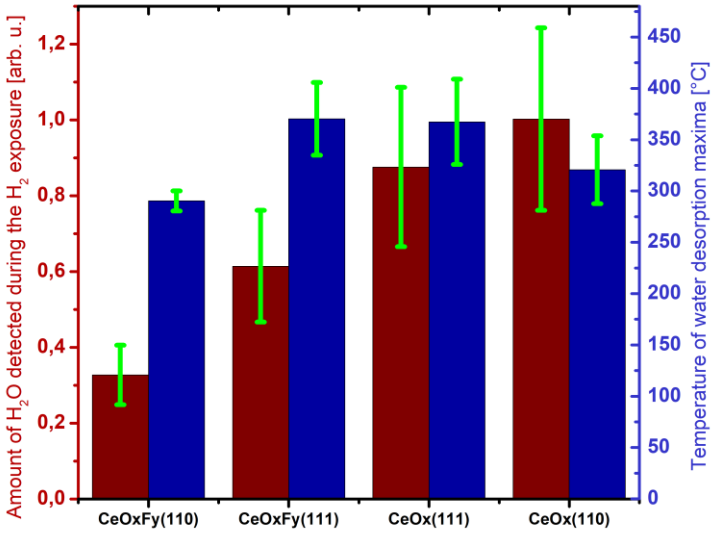

Figure 37: Average amount of produced water during the H_2 exposures (wine columns) and the temperatures of desorption maxima (blue columns).

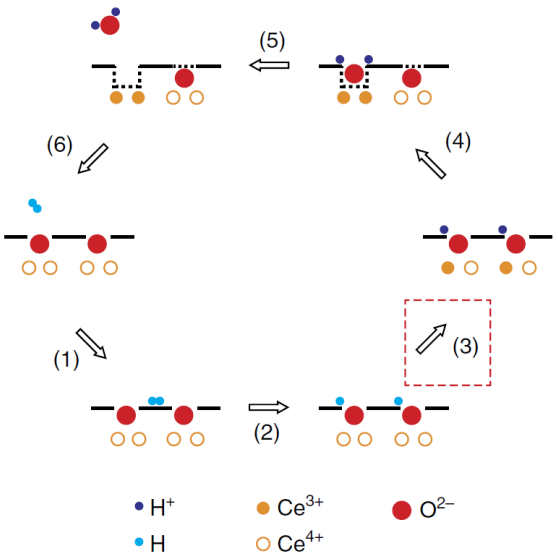

Figure 38: Hydrogen oxidation reaction cycle, taken and adapted from [115]. (1) Hydrogen adsorption and dissociation; (2) Spillover and migration of atomic hydrogen; (3) Charge transfer and OH creation; (4) OH association (5) Water desorption; (6) Reoxidation of cerium oxide surface.

Therefore, in order to be able to observe the rate limiting step, we had to eliminate several drawbacks of reactions in UHV chamber. As a result, we have devised an experiment in NAP-XPS apparatus which compared the reaction rates in steps (1) to (3) (see Figure 38). Unfortunately, we were not able to separate or limit the possibility of a rate limitation in steps (1)-(3). The first hindrance we had to eliminate was the cerium oxide reduction in step (6). So as to ascertain that the substrate was fully oxidized, we monitored the Ce 3*d* spectrum throughout the reaction of H_2 with O_2 (ratio 2:1), which took place in partial pressure of 70 Pa. In this way, we made sure that the surface was permanently fully oxidized and that all the emerged oxygen vacancies were immediately healed. On top of that, we increased the temperature above the water desorption maxima found out in UHV experiments. So, we conducted the reaction at 500°C and measured the O 1*s* signal for any signs of OH groups, which had been clearly visible at lower reaction temperatures. Nevertheless, we observed neither OH groups at 500°C nor any signs of adsorbed H_2O in the O 1*s* spectra. This confirmed that the reaction steps (4) and (5) were fast enough and did not limit the speed of the observed reaction. The ascertained experimental conditions allowed us to focus on the critical steps (1)-(3), which had to act as a bottleneck for the hydrogen oxidation reaction.

The comparison of the amount of produced water on different samples is shown in Figure 39. We can clearly see that the reaction over the (110) ordered samples is more efficient, however, for both the sample orientations, the fluorine doping slightly decreased the hydrogen oxidation rate. This could be caused simply by the presence of fluorine in the topmost layers, where it substitutes for oxygen and blocks by this the hydrogen anchorage. In other words, fluorine hinders the charge transfer and creation of hydroxyl group on the surface. On the other hand, this property could be understood as a benefit of fluorine doped samples, whose ability to dissociate hydrogen depends on the capabilities of rare metal particles and which would not tend to lose atomic hydrogen in hydrogen oxidation reactions.

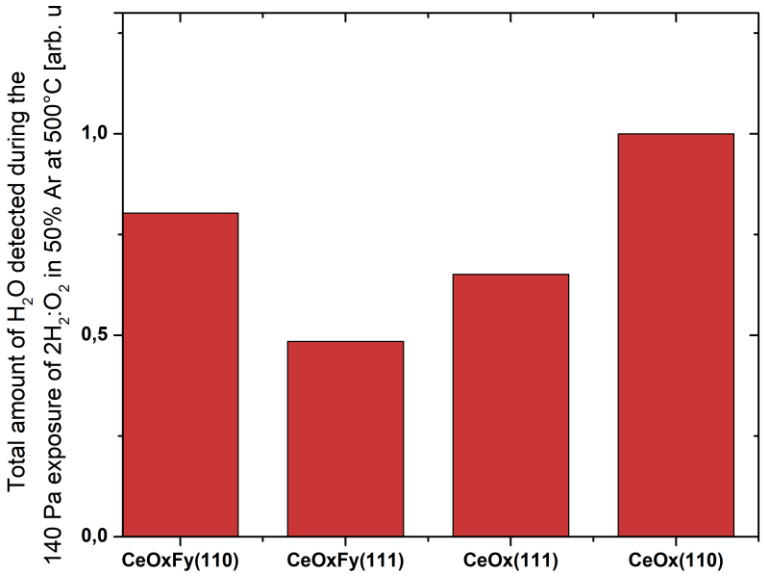

Figure 39: Total amount of produced water over different samples as detected by QMS in NAP-XPS apparatus. The reaction conditions were: Sample temperature 500°C, 50% of H_2 and O_2 – H_2:O_2 ratio 2:1 and 50% of Ar, total pressure 140 Pa.

3.5.6. Conclusion

In conclusion, we have shown the possibilities of isotopically labeled gases in combination with the TPR experimental setup. We identified the oxygen exchange taking place at the interface of Rh particles and ceria upon exposure with $^{13}C^{18}O$ gas. We have ruled out other possible mechanisms for oxygen exchange and employed this mechanism in deliberate doping of cerium oxide layers with ^{18}O. We have also compared the OSCs of different samples. The highest OSC was observed for CeOx(110) layers while the fluorine-doped CeOxFy(110) showed lowest OSC. The results for CeOx(111) and CeOxFy(111) layers were comparable, which agrees with our previously published results [112] (see also Section 3.2).

We have also used the isotopically labeled gases to identify water produced over the samples upon annealing in a stream of hydrogen. The experiments conducted in UHV confirmed the previously observed OSCs of the samples and helped to devise experimental conditions for hydrogen oxidation reaction study in NAP-XPS. NAP-XPS allowed us to monitor the chemical state of the sample during the hydrogen oxidation reaction and set experimental conditions so as to exclude few rate limiting steps in the reaction. In the devised experiment, we have compared the rate of hydrogen dissociation, hydrogen spillover, and electron transfer between cerium and hydroxyl group, which should be the rate limiting step for the reaction. Our results favorite the (110) terminated samples over the (111) terminated and show that fluorine-doping has negative impact on water production. This could be viewed as an advantage for PEMFC, where the hydrogen dissociation rate is determined by the choice and load of a rare metal and the water production is rather an unwanted side product.

3.6. Stability of Fluorine in CeOxFy Layers

3.6.1. Preface

One of the goals of the measurements in NAP-XPS was to assess the stability of fluorine in CeOxFy layers in near-ambient pressure conditions. Even though we already know that fluorine is apt to get exchanged for oxygen in UHV conditions, the effect of higher pressure can cause its utmost instability. This question is very important for any future application of deliberately fluorinated cerium oxide layers in real catalytic systems. Moreover, these findings can be used also in deliberate defluoridation of contaminated ceria systems. Potential applications are, for instance, cleaning of ceria single crystals or recycling of ceria-based water defluoridation filters [82].

In this chapter, we will also discuss the dissimilarities observed on fluorine doped CeOxFy(111) and CeOxFy(110) samples. Our UHV observations suggested that fluorine is more stable on one of the facet and we wanted to confirm these results also in near-ambient conditions. However, surface stability seems to be altered by the presence of Rh particles on the layer too. This could be related to the ability of Rh particles to dissociate hydrogen, which was demonstrated in Section 3.5.5. Dissociated hydrogen migrating on the surface could be prone to interact with fluorine in adsorbate positions, yielding HF, which was already suggested as the means of fluorine depletion in Section 3.2.7. Moreover, (111) surface has been recently found prone to expel fluorine into such adsorbate positions [131]. Experimental confirmation of this theoretical prediction is provided in Chapter 3.3.

3.6.2. Experimental Section

The experiments were conducted on XPS/TPR/LEED and NAP-XPS systems, which were described in detail in Sections 2.8.1 and 2.8.3.

The samples consist of continuous CeOx(Fy) layers prepared on Rh(111) and Rh(110) single crystals, whose preparation was described in detail in previous chapter (see Section 3.5.2). Stability of fluorine is investigated in two different configurations. In the first part, stability of fluorine in cerium oxide without any presence of ceria-rhodium interface will be discussed. For the second part, fluorine depletion after the deposition of Rh particles will be examined.

3.6.3. Results – Fluorine Stability in CeOxFy(111) and CeOxFy(110)

We have examined fluorine stability by annealing samples in partial pressure of oxygen 2.7×10^{-6} Pa at the sample surface. Exposure of cerium oxyfluoride layers to oxygen or air in order to release fluorine and create cerium oxide was reported already in refs. [79], [80]. We have annealed the samples consecutively to increasing temperatures, which started at temperature applied during the preparation of the layer. The results for different fluorine doping levels are showed in Figure 40.

Even though all the prepared layers showed the requested ordering, we cannot responsibly ascertain that the layers with fluorine content above 50% keep the cubic fluorite-like structure. Although CeOF was reported to maintain cubic structure [79], [80], upon higher levels of fluorine doping, cerium oxyfluoride tends to switch to hexagonal CeF_3 [78]. So, in spite of the fact that the green line in Figure 40 has its initial fluorine content around 80%, we can clearly see the overall trend of the (111)

ordered samples to decrease their fluorine doping level. Most pronounced are these changes on samples with lower initial fluorine content. This could be caused by migration of fluorine from deeper layers to the surface [72], which would cause virtual increase of the fluorine content in the layer. Therefore, we get the best overview by comparing the samples with equal initial doping level (black and red lines in Figure 40). On these two samples we can clearly see the contrast in fluorine diminishing. Because the structure of cerium oxyfluoride should be cubic in both cases, the most straightforward explanation of the observed discrepancies must be based on the surface ordering difference. A significant role could be played by the fluorine expelling mechanism, which was confirmed on (111) surface (see Section 3.3), and whose effects stood probably behind the observed difference in OSCs (see Section 3.5.4).

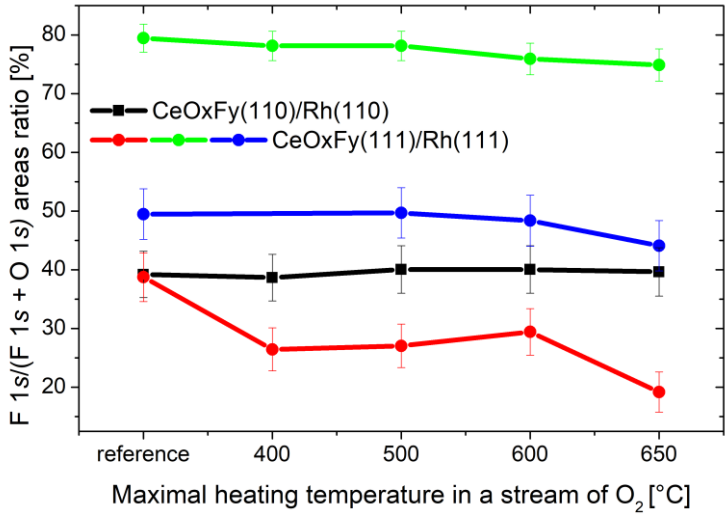

Figure 40: Fluorine content in continuous cerium oxyfluoride layers after annealing to 400, 500, 600 and 650°C in a stream of O_2.

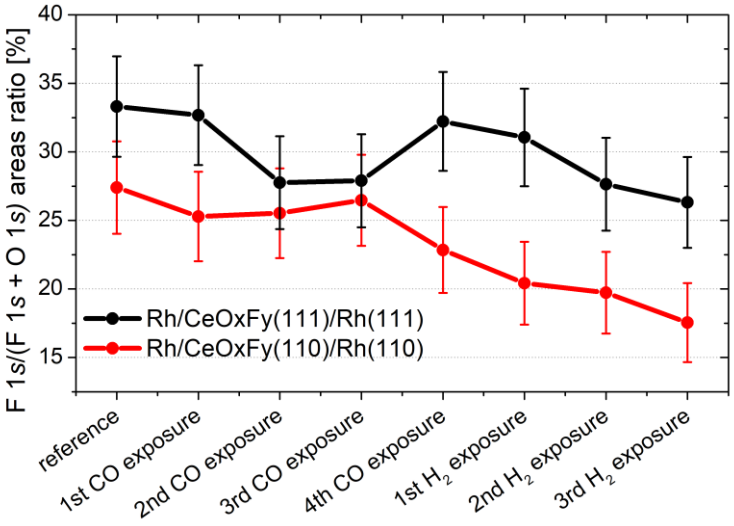

Figure 41: Fluorine diminishing on Rh/CeOxFy(111) and Rh/CeOxFy(110) samples. The CO and H_2 exposure cycles were conducted in partial pressures of 2.7×10^{-6} Pa and 1.3×10^{-5} Pa, respectively. During the first CO exposure, the samples were annealed to 150°C, during every other exposure, samples were annealed to 500°C. After each CO or H_2 exposure followed a O_2 exposure in 2.7×10^{-6} Pa of O_2 to 500°C.

However, stability of fluorine is largely changed by deposition of Rh particles on top of the CeOxFy layers – see Figure 41. We can see, that after deposition of Rh particles, fluorine content decreased in cases of both (111) and (110) surface terminations. This could be explained either by migration of fluorine on top of the Rh particles, however we note that no such behavior was observed on low coverage inverse catalysts, or by a reaction catalyzed by Rh particles which involves fluorine.

3.6.4. Results – Fluorine Stability in Near-Ambient Conditions

To resolve the puzzle outlined in previous section, we have to consider the measurements conducted in NAP-XPS, where any fluorine depletion is more pronounced (see Figure 42). In Figure 42, we can see that there is little to no difference between the (110) and (111) surface terminations, yet the fluorine in CeOxFy(111) seems slightly more stable. Despite its lower initial content, CeOxFy(111) shows higher doping level at most of the elevated temperatures. In addition, CeOxFy(111) does not have such pronounced differences between the maximal and minimal value at 200°C and 250°C. This slightly higher stability could be explained by higher reactivity of (110) layers, discussed in Sections 3.5.4 and 3.5.5, in case when oxygen (or fluorine) is more weakly bonded on the surface with (110) termination. This allows more oxygen to be released from these layers, as well as it showed itself in lower temperature of water production maxima (see Figure 34 and Figure 39).

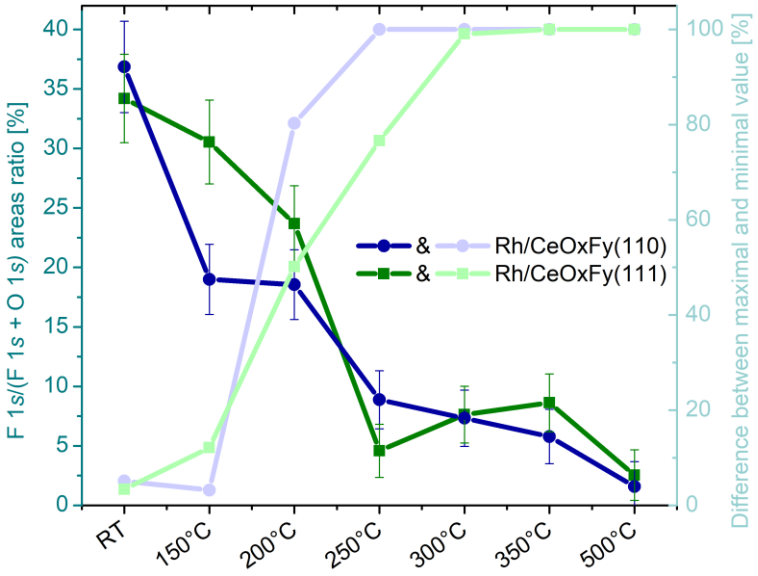

Figure 42: Maximal fluorine content during NAP-XPS measurements at certain temperature (dark lines, left axis); Relative change in fluorine doping level at each temperature as detected during various exposures with reducing and oxidizing gas mixtures (light lines, right axis). The value 100% means that no fluorine was detected during the oxidizing treatment.

From the data in Figure 42, we see that fluorine is continuously depleted from the layer even at the lowest temperature of 150°C. However, much more interesting is the difference in the observed amount of fluorine in dependence on the actual gas composition (light lines). During reducing treatments, we observed higher fluorine content attacking the maximal value presented in Figure 42 (dark lines), in contrast the detected value at oxidizing conditions was much lower, and, starting at 300°C,

we even detected no fluorine peak at all. Considering this, we can conclude that fluorine is stable in certain positions even up to 200°C or more.

However, we were able to identify the critical gas mixture after which the fluorine decrease was permanent and irreversible. In Figure 29, we can see that exposure with CO and O_2 mixture did not affected the fluorine content so heavily and, after the CO treatment, the fluorine content rose to its previous levels. However, the exposure with H_2 and O_2 mixture at the same temperature caused massive decrease of fluorine content, which was never restored to its previous levels. This key observation opens doors for understanding of the prevailing mechanism of fluorine removal. It seems that the combined exposure with hydrogen and oxygen is critical, while hydrogen exposure alone is not so aggressive towards fluorine. Thus, it is most probable that fluorine diminishes in reaction of atomic hydrogen and fluorine in the adsorbate position. While hydrogen exposure in the presence of Rh particles causes hydrogen dissociation and migration of atomic hydrogen on top of ceria, the function of oxygen is rather twofold. Firstly it expels fluorine from the topmost layer to the adsorbate positions, where it is exposed to the migrating hydrogen. Such fluorine is most possibly bond more weakly than the embedded fluorine in the lattice. In combination with higher temperature, fluorine reacts with atomic hydrogen and desorbs as HF.

Second function of oxygen exposure is in its repelling ability, which drives off fluorine from the surface. This is most likely the reason why fluorine keeps returning in the signal of F 1*s* up to 500°C. The repelled fluorine is returning to its most stable position at the surface upon treating the sample in reducing conditions. Therefore, the complete diminishing of fluorine signal and its reappearance in case of ceria reduction can be explained as the outcome of fluorine migration in the ceria layer. In oxidizing conditions, a part of fluorine atoms is expelled to the surface, while the second part is repelled away from it. After creation of oxygen vacancies, fluorine migrates back to the surface, which causes increase of the F 1*s* signal.

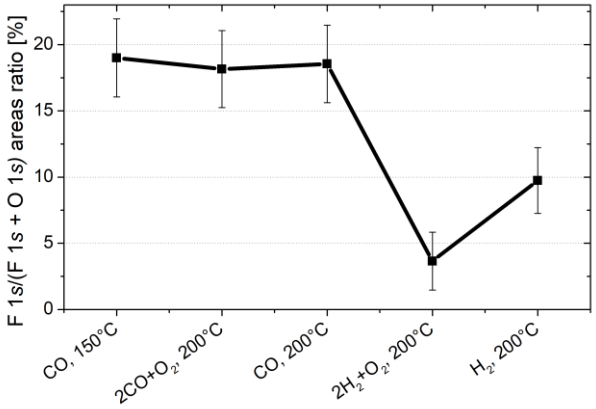

Figure 43: Fluorine content in Rh/CeOxFy(110) in dependence on gas mixture and temperature. Gas pressures during the exposures were ~ 100 Pa. During the $2CO+O_2$ exposure and $2H_2+O_2$ exposure, the gas ratio was 2:1, however, cerium oxide was fully oxidized. In contrast, during the CO and H_2 exposures, cerium oxide was significantly reduced.

We should also comment to the low levels of fluorine in the CeOxFy layers at 500°C. One might wonder whether the observed ca. 2% content of fluorine could influence the obtained results. In the light of the fluorine migration in the layer, we can expect that under favorable conditions, all fluorine will be situated at the surface. Considering thickness of the cerium oxide layer 10 ML and providing the IMFP of

oxygen in CeOF is 17 Å, the calculated content of fluorine in the topmost layer is around 9%. This means that for ten oxygen atoms there is one fluorine atom. We believe that such amount is capable to substantially influence the studied surface reactions.

3.6.5. Conclusion

We have shown that fluorine stability in ceria is very influenced by the surface termination of the layer. The (110) terminated sample was not prone to lose fluorine, while variously doped (111) layers showed continuous diminishing of fluorine. We believe that expelling of fluorine into the adsorbate position plays a significant role in elucidation of this phenomenon.

Nevertheless, we showed that the situation is different in case of rhodium particles deposited on top of the cerium oxyfluoride layers. With this layout, the samples were losing fluorine irrespectively on the surface ordering. Under near-ambient conditions, fluorine remained stable in the layer up to 200°C. However, we have shown that important is not only temperature, but also the gas composition. Upon combined H_2 and O_2 exposure, the samples were most liable to lose fluorine permanently. Moreover, reductive or oxidative nature of the gas composition caused visible changes in F 1*s* signal readings. From these facts we suspect the combined acting of atomic hydrogen on fluorine in adsorbate position critical for fluorine stability in the layer. Nonetheless, the oxygen treatment is of twofold nature. On one hand it expels fluorine to adsorbate position; on the other hand it repels the remaining fluorine deeper into the ceria. Such fluorine will migrate back to the surface only after reduction of ceria.

All these findings can find its use in various applications dealing with fluorine removal from ceria. They are also important for any prospective utilization of fluorine doped materials in industrial sphere.

4. Summary

In summary, we have shown how fluorine incorporation in ceria influences its electronic, morphological and chemical state. Namely, we have shown and described the perturbations in the shape of Ce 3*d* spectrum as a result of fluorine inclusion in ceria and we proposed a procedure for Ce 3*d* spectra deconvolution. We have described the morphological differences in growth and ordering of fluorine-doped ceria layers on Rh(111) and showed that the OSC of fluorine-free and fluorine-doped ceria with (111) ordering is comparable. On top of that, we have observed the electronic effects induced by the presence of fluorine expelled to adsorbate position on ceria. This study also proved that the RPES measurements of Ce^{4+} are sensitive to local electronic structure, which was distorted by the presence of fluorine.

The following work focused also on comparison of two distinctive surface terminations – (111) and (110). CeO_2(110) and CeOxFy(110) layers were successfully prepared by epitaxial growth of (fluorine-doped) ceria on Rh(110) single crystal. These methods were used in preparation of complex Rh/CeOx(Fy)(111) and Rh/CeOx(Fy)(110) samples which maintained both the benefits of real catalytic layout and of model system approach. These samples then served for comparison of reactivity of Rh particles supported on fluorine-doped and fluorine-free ceria.

Additionally, we have employed isotopically labeled gases, which helped us to reveal the oxygen exchange mechanism taking place at the interface of rhodium and ceria. Moreover, we were able to compare directly the OSCs and hydrogen oxidation reaction rates of four different kinds of samples.

Eventually, we have focused on stability of fluorine in the ceria layers at various conditions. We have unveiled the twofold nature of oxygen exposure of fluorinated ceria and scrutinized the role of Rh particles in fluorine depletion from ceria.

Our findings can find its use in rational design of future catalysts which could use the anion doping as a tool for tailoring the reactivity or selectivity. Detailed study of fluorine diminishing from cerium oxyfluoride might be utilized either for improving of fluorine removal techniques or for developing methods for fluorine trapping in ceria.

Bibliography

[1] S. J. Green, *Industrial Catalysis*. London: E. Benn Limited, 1928.

[2] B. Lindström and L. J. Pettersson, "A brief history of catalysis," *Cattech*, vol. 7, no. 4, pp. 130–138, 2003.

[3] D. L. Davis, M. L. Bell, and T. Fletcher, "A look back at the London smog of 1952 and the half century since," *Environ. Health Perspect.*, vol. 110, no. 12, pp. 734–735, 2002.

[4] E. J. Houdry, "Catalytic structure and composition," US2742437, 1956.

[5] R. M. Yarrington and W. E. Bambrick, "Deactivation of Automobile Exhaust Control Catalyst," *J. Air Pollut. Control Assoc.*, vol. 20, no. 6, pp. 398–401, Jun. 1970.

[6] A. Faiz, C. S. Weaver, and M. P. Walsh, *Air Pollution from Motor Vehicles Standards and Technologies for Controlling Emissions*. Washington D.C., 1996.

[7] H. S. Gandhi, G. W. Graham, and R. W. McCabe, "Automotive exhaust catalysis," in *Journal of Catalysis*, 2003, vol. 216, no. 1–2, pp. 433–442.

[8] J. Kašpar, P. Fornasiero, and M. Graziani, "Use of CeO_2-based oxides in the three-way catalysis," *Catalysis Today*, vol. 50, no. 2. pp. 285–298, Apr-1999.

[9] A. Trovarelli, C. de Leitenburg, M. Boaro, and G. Dolcetti, "The utilization of ceria in industrial catalysis," *Catalysis Today*, vol. 50, no. 2. pp. 353–367, 1999.

[10] L. Martín, J. Arranz, O. Prieto, R. Trujillano, M. Holgado, M. Galán, and V. Rives, "Simulation three-way catalyst ageing Analysis of two conventional catalyst," *Appl. Catal. B Environ.*, vol. 44, no. 1, pp. 41–52, Aug. 2003.

[11] H. Muraki and G. Zhang, "Design of advanced automotive exhaust catalysts," *Catal. Today*, vol. 63, no. 2–4, pp. 337–345, Dec. 2000.

[12] S. Matsumoto, "Recent advances in automobile exhaust catalysts," *Catal. Today*, vol. 90, no. 3–4, pp. 183–190, 2004.

[13] K. Kili, L. Hilaire, and F. Le Normand, "Modification by lanthanide (La, Ce) promotion of catalytic properties of palladium: Characterization of the catalysts," *Physical Chemistry Chemical Physics*, vol. 1. pp. 1623–1631, 1999.

[14] D. N. Belton and K. C. Taylor, "Automobile exhaust emission control by catalysts," *Curr. Opin. Solid State Mater. Sci.*, vol. 4, no. 1, pp. 97–102, Feb. 1999.

[15] D. M. Fernandes, C. F. Scofield, A. A. Neto, M. J. B. Cardoso, and F. M. Z. Zotin, "The influence of temperature on the deactivation of commercial Pd/Rh automotive catalysts," *Process Saf. Environ. Prot.*, vol. 87, no. 5, pp. 315–322, Sep. 2009.

[16] X. Gao, Y. Jiang, Y. Zhong, Z. Luo, and K. Cen, "The activity and characterization of CeO_2-TiO_2 catalysts prepared by the sol–gel method for selective catalytic reduction of NO with NH_3," *J. Hazard. Mater.*, vol. 174,

no. 1–3, pp. 734–739, Feb. 2010.

[17] B. M. Weckhuysen, “In-situ characterization of heterogeneous catalysts themed issue,” no. 12, 2010.

[18] “http://www.energytrendsinsider.com/wp-content/uploads/2013/04/Energy-Density.png?00cfb7.” [Online]. [Accessed: 01-Aug-2017].

[19] D. . Castner, B. . Sexton, and G. . Somorjai, “Leed and thermal desorption studies of small molecules (H_2, O_2, CO, CO_2, NO, C_2H_4, C_2H_2 AND C) chemisorbed on the rhodium (111) and (100) surfaces,” *Surf. Sci.*, vol. 71, no. 3, pp. 519–540, Feb. 1978.

[20] R. A. Marbrow and R. M. Lambert, “Chemisorption, surface structural chemistry, and electron impact properties of carbon monoxide on rhodium (110),” *Surf. Sci.*, vol. 67, no. 2, pp. 489–500, Oct. 1977.

[21] M. Smedh, A. Beutler, T. Ramsvik, and R. Nyholm, “Vibrationally resolved C 1*s* photoemission from CO absorbed on Rh (111): the investigation of a new chemically shifted C 1s component,” *Surf. Sci.*, vol. 491, no. 1–2, pp. 99–114, 2001.

[22] V. Hove, “Structural reanalysis of the Rh(111) +(3 x 3)R30°-CO and Rh (111) + (2 x 2)-3CO phases using automated tensor LEED,” vol. 391, pp. 176–182, 1997.

[23] A. J. Jaworowski, A. Beutler, F. Strisland, R. Nyholm, B. Setlik, D. Heskett, and J. N. Andersen, “Adsorption sites in O and CO coadsorption phases on Rh(111) investigated by high-resolution core-level photoemission,” *Surf. Sci.*, vol. 431, no. 1–3, pp. 33–41, 1999.

[24] T. Engel, G. Ertl, H. P. D.D. Eley, and B. W. Paul, “Elementary Steps in the Catalytic Oxidation of Carbon Monoxide on Platinum Metals,” *Adv. Catal.*, vol. Volume 28, pp. 1–78, 1979.

[25] D. Castner and G. Somorjai, “LEED, AES and thermal desorption studies of the oxidation of the rhodium(111) surface,” *Applications of Surface Science*, vol. 6, no. 1. pp. 29–38, Sep-1980.

[26] M. Ganduglia-Pirovano and M. Scheffler, “Structural and electronic properties of chemisorbed oxygen on Rh(111),” *Phys. Rev. B*, vol. 59, no. 23, pp. 15533–15543, 1999.

[27] D. Alfè and S. Baroni, “The structure and phase stability of CO adsorbates on Rh (110),” *Surf. Sci.*, vol. 382, no. 1–3, pp. L666–L671, Jun. 1997.

[28] C. Q. Sun, “On the nature of the O-Rh (110) multiphase ordering,” *Surf. Sci.*, vol. 398, no. 3, pp. L320–L326, Feb. 1998.

[29] A. Baraldi, S. Lizzit, D. Cocco, G. Comelli, G. Paolucci, R. Rosei, and M. Kiskinova, “Oxygen and carbon monoxide interactions on Rh(110) studied by real-time X-ray photoemission spectroscopy,” *Surf. Sci.*, vol. 385, no. 2–3, pp. 376–385, Aug. 1997.

[30] A. De Koster and R. Van Santen, “Dissociation of CO on Rh surfaces,” *Surf. Sci.*, vol. 233, pp. 366–380, 1990.

[31] Z.-P. Liu and P. Hu, “General trends in CO dissociation on transition metal surfaces,” *J. Chem. Phys.*, vol. 114, no. 19, p. 8244, 2001.

[32] M. Mavrikakis and M. Ba, “Structure sensitivity of CO dissociation on Rh surfaces,” vol. 81, no. 3, pp. 153–156, 2002.

[33] C. T. Campbell and C. H. F. Peden, “Oxygen Vacancies and Catalysis on Ceria Surface,” *Science*, vol. 653, no. 2002, pp. 2004–2005, 2004.

[34] N. Skorodumova, S. Simak, B. Lundqvist, I. Abrikosov, and B. Johansson, “Quantum Origin of the Oxygen Storage Capability of Ceria,” *Phys. Rev. Lett.*, vol. 89, no. 16, p. 166601, Sep. 2002.

[35] Tana, M. Zhang, J. Li, H. Li, Y. Li, and W. Shen, “Morphology-dependent redox and catalytic properties of CeO_2 nanostructures: Nanowires, nanorods and nanoparticles,” *Catal. Today*, vol. 148, no. 1–2, pp. 179–183, Oct. 2010.

[36] Z. Wu, M. Li, and S. H. Overbury, “On the structure dependence of CO oxidation over CeO_2 nanocrystals with well-defined surface planes,” *J. Catal.*, vol. 285, no. 1, pp. 61–73, Jan. 2012.

[37] N. J. Lawrence, J. R. Brewer, L. Wang, T. S. Wu, J. Wells-Kingsbury, M. M. Ihrig, G. Wang, Y. L. Soo, W. N. Mei, and C. L. Cheung, “Defect engineering in cubic cerium oxide nanostructures for catalytic oxidation,” *Nano Lett.*, vol. 11, no. 7, pp. 2666–2671, 2011.

[38] T. Duchoň, F. Dvořák, M. Aulická, V. Stetsovych, M. Vorokhta, D. Mazur, K. Veltruská, T. Skála, J. Mysliveček, I. Matolínová, and V. Matolín, “Ordered phases of reduced ceria as epitaxial films on Cu(111),” *J. Phys. Chem. C*, vol. 118, no. 1, pp. 357–365, Jan. 2014.

[39] V. Stetsovych, F. Pagliuca, F. Dvořák, T. Duchoň, M. Vorokhta, M. Aulická, J. Lachnitt, S. Schernich, I. Matolínová, K. Veltruská, T. Skála, D. Mazur, J. Mysliveček, J. Libuda, and V. Matolín, “Epitaxial cubic Ce_2O_3 films via Ce-CeO_2 interfacial reaction,” *J. Phys. Chem. Lett.*, vol. 4, no. 6, pp. 866–871, Mar. 2013.

[40] A. Kotani, H. Mizuta, T. Jo, and J. C. Parlebas, “Theory of core photoemission spectra in CeO_2,” *Solid State Commun.*, vol. 53, no. 9, pp. 805–810, Mar. 1985.

[41] T. Jo and A. Kotani, “Theory of Photoemission, Photoabsorption and Inverse Photoemission in CeO_2 and Metallic Ce Compounds,” *Phys. Scr.*, vol. 35, no. 4, pp. 570–574, Apr. 1987.

[42] P. Burroughs, A. Hamnett, A. F. Orchard, and G. Thornton, “Satellite structure in the X-ray photoelectron spectra of some binary and mixed oxides of lanthanum and cerium,” *Journal of the Chemical Society, Dalton Transactions*, no. 1686. p. 1686, 1976.

[43] P. S. Bagus, E. S. Ilton, and C. J. Nelin, “The interpretation of XPS spectra: Insights into materials properties,” *Surface Science Reports*, vol. 68, no. 2. Elsevier, pp. 273–304, Jun-2013.

[44] C. J. Nelin, P. S. Bagus, E. S. Ilton, S. a. Chambers, H. Kuhlenbeck, and H.-J. Freund, “Relationships between complex core level spectra and materials properties,” *Int. J. Quantum Chem.*, vol. 110, no. 15, pp. 2752–2764, Aug. 2010.

[45] T. Duchoň, M. Aulická, E. F. Schwier, H. Iwasawa, C. Zhao, Y. Xu, K. Veltruská, K. Shimada, and V. Matolín, “Covalent versus localized nature of

4*f* electrons in ceria: Resonant angle-resolved photoemission spectroscopy and density functional theory," *Phys. Rev. B*, vol. 95, no. 16, p. 165124, Apr. 2017.

[46] P. S. Bagus, C. J. Nelin, D. A. Hrovat, and E. S. Ilton, "Covalent bonding in heavy metal oxides," *J. Chem. Phys.*, vol. 146, no. 13, p. 134706, 2017.

[47] F. Dvořák, O. Stetsovych, M. Steger, E. Cherradi, I. Matolínová, N. Tsud, M. Škoda, T. Skála, J. Mysliveček, and V. Matolín, "Adjusting morphology and surface reduction of CeO_2(111) thin films on Cu(111)," *J. Phys. Chem. C*, vol. 115, no. 111, pp. 7496–7503, 2011.

[48] O. Stetsovych, J. Beran, F. Dvořák, K. Mašek, J. Mysliveček, and V. Matolín, "Polarity driven morphology of CeO_2(100) islands on Cu(111)," *Appl. Surf. Sci.*, vol. 285, pp. 766–771, Nov. 2013.

[49] L. Szabova, O. Stetsovych, M. F. Camellone, and S. Fabris, "Distinct Physicochemical Properties of the First Ceria Monolayer on Cu(111)," no. 111, 2012.

[50] K. Mašek, J. Beran, and V. Matolín, "RHEED study of the growth of cerium oxide on Cu(111)," *Appl. Surf. Sci.*, vol. 259, pp. 34–38, Oct. 2012.

[51] M. Aulická, T. Duchoň, F. Dvořák, V. Stetsovych, J. Beran, K. Veltruská, J. Mysliveček, K. Mašek, and V. Matolín, "Faceting Transition at the Oxide–Metal Interface: (13 13 1) Facets on Cu(110) Induced by Carpet-Like Ceria Overlayer," *J. Phys. Chem. C*, vol. 119, no. 4, pp. 1851–1858, Jan. 2015.

[52] S. Eck, C. Castellarin-Cudia, S. Surnev, M. . Ramsey, and F. . Netzer, "Growth and thermal properties of ultrathin cerium oxide layers on Rh(111)," *Surf. Sci.*, vol. 520, no. 3, pp. 173–185, Dec. 2002.

[53] F. Šutara, M. Cabala, L. Sedláček, T. Skála, M. Škoda, V. Matolín, K. C. Prince, and V. Cháb, "Epitaxial growth of continuous CeO_2(111) ultra-thin films on Cu(111)," *Thin Solid Films*, vol. 516, no. 18, pp. 6120–6124, Jul. 2008.

[54] T. Staudt, Y. Lykhach, L. Hammer, M. A. Schneider, V. Matolín, and J. Libuda, "A route to continuous ultra-thin cerium oxide films on Cu(111)," *Surf. Sci.*, vol. 603, no. 23, pp. 3382–3388, 2009.

[55] V. Matolín, J. Libra, I. Matolínová, V. Nehasil, L. Sedláček, and F. Šutara, "Growth of ultra-thin cerium oxide layers on Cu(111)," *Appl. Surf. Sci.*, vol. 254, no. 1, pp. 153–155, Oct. 2007.

[56] S. D. Senanayake, D. Stacchiola, and J. A. Rodriguez, "Unique Properties of Ceria Nanoparticles Supported on Metals: Novel Inverse Ceria/Copper Catalysts for CO Oxidation and the Water-Gas Shift Reaction," *Acc. Chem. Res.*, vol. 46, no. 8, pp. 1702–1711, 2013.

[57] S. Eck, C. Castellarin-Cudia, S. Surnev, K. C. Prince, M. G. Ramsey, and F. P. Netzer, "Adsorption and reaction of CO on a ceria–Rh(111) 'inverse model catalyst' surface," *Surface Science*, vol. 536, no. 1–3. pp. 166–176, Jun-2003.

[58] Y. Suchorski and R. Wrobel, "CO Oxidation on a CeOx/Pt (111) Inverse Model Catalyst Surface: Catalytic Promotion and Tuning of Kinetic Phase Diagrams," *J. Phys. ...*, no. 111, pp. 20012–20017, 2008.

[59] J. A. Rodriguez, S. Ma, P. Liu, J. Hrbek, J. Evans, and M. Perez, "Activity of

CeOx and TiOx Nanoparticles Grown on Au(111) in the Water-Gas Shift Reaction," *Science*, vol. 318, no. 5857, pp. 1757–1760, Dec. 2007.

[60] S. D. Senanayake, D. Stacchiola, J. Evans, M. Estrella, L. Barrio, M. Pérez, J. Hrbek, and J. a. Rodriguez, "Probing the reaction intermediates for the water–gas shift over inverse CeOx/Au(111) catalysts," *J. Catal.*, vol. 271, no. 2, pp. 392–400, May 2010.

[61] S. J. Tauster, "Strong metal-support interactions," *Acc. Chem. Res.*, vol. 20, no. 11, pp. 389–394, 1987.

[62] D. R. Mullins, "The surface chemistry of cerium oxide," *Surf. Sci. Rep.*, vol. 70, no. 1, pp. 42–85, 2015.

[63] A. Bruix, J. a Rodriguez, P. J. Ramírez, S. D. Senanayake, J. Evans, J. B. Park, D. Stacchiola, P. Liu, J. Hrbek, and F. Illas, "A new type of strong metal-support interaction and the production of H2 through the transformation of water on Pt/CeO_2(111) and Pt/CeO(x)/TiO_2(110) catalysts.," *J. Am. Chem. Soc.*, vol. 134, no. 21, pp. 8968–74, 2012.

[64] C. T. Campbell, "Catalyst–support interactions: Electronic perturbations," *Nat. Chem.*, vol. 4, no. 8, pp. 597–598, 2012.

[65] Y. Lykhach, S. M. Kozlov, T. Skála, A. Tovt, V. Stetsovych, N. Tsud, F. Dvořák, V. Johánek, A. Neitzel, J. Mysliveček, S. Fabris, V. Matolín, K. M. Neyman, and J. Libuda, "Counting electrons on supported nanoparticles," *Nat. Mater.*, vol. 15, no. 3, pp. 284–288, Dec. 2015.

[66] K. Ševčíková, L. Szabová, M. Kettner, P. Homola, N. Tsud, S. Fabris, V. Matolín, and V. Nehasil, "Experimental and Theoretical Study on the Electronic Interaction between Rh Adatoms and CeOx Substrate in Dependence on a Degree of Cerium Oxide Reduction," *J. Phys. Chem. C*, vol. 120, no. 10, pp. 5468–5476, Mar. 2016.

[67] D. Martin and D. Duprez, "Mobility of Surface Species on Oxides. 1. Isotopic Exchange of $^{18}O_2$ with ^{16}O of SiO_2, Al_2O_3, ZrO_2, MgO, CeO_2 , and CeO_2 - Al_2O_3. Activation by Noble Metals. Correlation with Oxide Basicity.," *J. Phys. Chem.*, vol. 100, no. 22, pp. 9429–9438, Jan. 1996.

[68] G. Zafiris and R. Gorte, "Evidence for Low-Temperature Oxygen Migration from Ceria to Rh," *J. Catal.*, vol. 139, no. 2, pp. 561–567, Feb. 1993.

[69] M. Bowker, L. J. Bowker, R. A. Bennett, P. Stone, and A. Ramirez-Cuesta, "In consideration of precursor states, spillover and Boudart's `collection zone' and of their role in catalytic processes," *J. Mol. Catal. a-Chemical*, vol. 163, no. 1–2, pp. 221–232, 2000.

[70] C. T. Campbell, "Ultrathin metal films and particles on oxide surfaces: structural, electronic and chemisorptive properties," *Surf. Sci. Rep.*, vol. 27, no. 1–3, pp. 1–111, Jan. 1997.

[71] J. Kullgren, M. J. Wolf, C. W. M. Castleton, P. Mitev, W. J. Briels, and K. Hermansson, "Oxygen Vacancies versus Fluorine at CeO_2(111): A Case of Mistaken Identity?," *Phys. Rev. Lett.*, vol. 112, no. 15, p. 156102, Apr. 2014.

[72] H. H. Pieper, C. Derks, M. H. Zoellner, R. Olbrich, L. Tröger, T. Schroeder, M. Neumann, and M. Reichling, "Morphology and nanostructure of CeO_2(111) surfaces of single crystals and Si(111) supported ceria films,"

Physical Chemistry Chemical Physics, vol. 14, no. 44. p. 15361, 28-Nov-2012.

[73] J. Zarraga-Colina, R. M. Nix, and H. Weiss, "Growth, structure, and stability of ceria films on Si(111) and the application of CaF_2 buffer layers," *J. Phys. Chem. B*, vol. 109, no. 111, pp. 10978–10985, 2005.

[74] J. Zarraga-Colina, R. M. Nix, and H. Weiss, "A novel approach to the epitaxial growth of CeO_2 films on Si(1 1 1)," *Surf. Sci.*, vol. 563, no. 1–3, 2004.

[75] Z. Dan, C. Ji, and L. Deqian, "Separation chemistry and clean technique of cerium(IV): A review," *J. Rare Earths*, vol. 32, no. 8, pp. 681–685, Aug. 2014.

[76] D. Zou, J. Chen, H. Cui, Y. Liu, and D. Li, "Wet Air Oxidation and Kinetics of Cerium(III) of Rare Earth Hydroxides," *Ind. Eng. Chem. Res.*, vol. 53, no. 35, pp. 13790–13796, Sep. 2014.

[77] R. Fiala, M. Vaclavu, A. Rednyk, I. Khalakhan, M. Vorokhta, J. Lavkova, V. Potin, I. Matolinova, and V. Matolin, "Pt–CeOx thin film catalysts for PEMFC," *Catal. Today*, vol. 240, pp. 236–241, Feb. 2015.

[78] M. Takashima, S. Fukami, Y. Nosaka, and T. Unishi, "Reaction between rare earth oxides and elemental fluorine. II. Kinetics of the fluorination of cerium dioxide," *J. Fluor. Chem.*, vol. 57, no. 1–3, pp. 131–138, Apr. 1992.

[79] W. Finkelnburg and A. Stein, "Cerium oxyfluoride and its lattice structure," *J. Chem. Phys.*, vol. 18, no. 9, p. 1296, 1950.

[80] N. C. Baenziger, J. R. Holden, G. E. Knudson, and A. I. Popov, "Unit Cell Dimensions of Some Rare Earth Oxyfluorides," *J. Am. Chem. Soc.*, vol. 76, no. 18, pp. 4734–4735, Sep. 1954.

[81] Z. Mazej, "Room temperature syntheses of lanthanoid tetrafluorides (LnF_4, Ln = Ce, Pr, Tb)," *Journal of Fluorine Chemistry*, vol. 118. pp. 127–129, 2002.

[82] T. Zhang, Q. Li, H. Xiao, Z. Mei, H. Lu, and Y. Zhou, "Enhanced fluoride removal from water by non-thermal plasma modified CeO_2/Mg-Fe layered double hydroxides," *Appl. Clay Sci.*, vol. 72, pp. 117–123, 2013.

[83] R. Zhang, Q. Zhong, W. Zhao, L. Yu, and H. Qu, "Promotional effect of fluorine on the selective catalytic reduction of NO with NH_3 over CeO_2-TiO_2 catalyst at low temperature," *Appl. Surf. Sci.*, vol. 289, pp. 237–244, 2014.

[84] R. Fiala, A. Figueroba, A. Bruix, M. Vaclavu, A. Rednyk, I. Khalakhan, M. Vorokhta, J. Lavkova, F. Illas, V. Potin, I. Matolinova, K. M. Neyman, and V. Matolin, "High efficiency of Pt^{2+}- CeO_2 novel thin film catalyst as anode for proton exchange membrane fuel cells," *Appl. Catal. B Environ.*, vol. 197, pp. 262–270, 2016.

[85] R. Lin, C. Cao, H. Zhang, H. Huang, and J. Ma, "Electro-catalytic activity of enhanced CO tolerant cerium-promoted Pt/C catalyst for PEM fuel cell anode," *Int. J. Hydrogen Energy*, vol. 37, no. 5, pp. 4648–4656, 2012.

[86] V. Parry, G. Berthomé, J. C. Joud, O. Lemaire, and A. a. Franco, "XPS investigations of the proton exchange membrane fuel cell active layers aging: Characterization of the mitigating role of an anodic CO contamination on

cathode degradation," *J. Power Sources*, vol. 196, no. 5, pp. 2530–2538, 2011.

[87] A. Einstein, "On a Heuristic Point of View about the Creation and Conversion of Light?," *Ann. Phys.*, vol. 17, no. 132, p. 91, 1905.

[88] "The Nobel Prize in Physics 1921," 2014. [Online]. Available: http://www.nobelprize.org/nobel_prizes/physics/laureates/1921/index.html. [Accessed: 04-Aug-2017].

[89] D. Briggs and J. T. Grant, *Surface analysis by Auger and X-Ray Photoelectron Spectroscopy*. IM Publications and SurfaceSpectra Limited, 2003.

[90] S. Tanuma, C. J. Powell, and D. R. Penn, "Calculation of electron inelastic mean free paths (IMFPs) VII. Reliability of the TPP-2M IMFP predictive equation," *Surf. Interface Anal.*, vol. 35, no. 1, pp. 268–275, 2003.

[91] J. F. Moulder, W. F. Stickle, P. E. Sobol, and K. D. Bomben, "Handbook of X-ray Photoelectron Spectroscopy," p. 261, 1992.

[92] C. D. Wagner, L. E. Davis, M. V. Zeller, J. A. Taylor, R. H. Raymond, and L. H. Gale, "Empirical atomic sensitivity factors for quantitative analysis by electron spectroscopy for chemical analysis," *Surf. Interface Anal.*, vol. 3, no. 5, pp. 211–225, 1981.

[93] M. Repoux, "Comparison of background removal methods for XPS," *Surf. Interface Anal.*, vol. 18, no. 7, pp. 567–570, 1992.

[94] S. Hüfner, *Photoelectron spectroscopy: principles and applications*. 2003.

[95] "Atomic Calculation of Photoionization Cross-Sections and Asymmetry Parameters." [Online]. Available: https://vuo.elettra.eu/services/elements/WebElements.html. [Accessed: 30-Aug-2017].

[96] S. Tanuma, C. J. Powell, and D. R. Penn, "Calculations of electron inelastic mean free paths. IX. Data for 41 elemental solids over the 50 eV to 30 keV range," *Surf. Interface Anal.*, vol. 43, no. 3, pp. 689–713, 2011.

[97] K. Hermann and M. A. Van Hove, "LEEDpat4." [Online]. Available: http://www.fhi-berlin.mpg.de/KHsoftware/LEEDpat/. [Accessed: 07-Aug-2017].

[98] R. M. Nix, "An Introduction to Surface Chemistry." [Online]. Available: http://www.chem.qmul.ac.uk/surfaces/scc/. [Accessed: 09-Aug-2017].

[99] P. a. Redhead, "Thermal desorption of gases," *Vacuum*, vol. 12, no. 4, pp. 203–211, 1962.

[100] A. M. de Jong and J. W. Niemantsverdriet, "Thermal desorption analysis: Comparative test of ten commonly applied procedures," *Surf. Sci.*, vol. 233, no. 3, pp. 355–365, 1990.

[101] E. Habenschaden and J. Küppers, "Evaluation of flash desorption spectra," *Surf. Sci.*, vol. 138, no. 1, 1984.

[102] R. Vašina, V. Kolařík, P. Doležel, M. Mynář, M. Vondráček, V. Cháb, J. Slezák, C. Comicioli, and K. C. Prince, "Mechanical design aspects of a soft X-ray plane grating monochromator," *Nucl. Instruments Methods Phys. Res. Sect. A Accel. Spectrometers, Detect. Assoc. Equip.*, vol. 467–468, pp. 561–

564, 2001.

[103] "NAP XPS - SURFACE KFPP." [Online]. Available: http://physics.mff.cuni.cz/kfpp/povrchy/equipment/napxps. [Accessed: 11-Aug-2017].

[104] M. Kettner, K. Ševčíková, P. Homola, V. Matolín, and V. Nehasil, "Influence of the Ce–F interaction on cerium photoelectron spectra in CeOXFY layers," *Chem. Phys. Lett.*, vol. 639, pp. 126–130, 2015.

[105] D. Briggs and M. P. Seah, *Practical Surface Analysis by Auger and X-ray Photoelectron Spectroscopy*. John Wiley and Sons Ltd, 1983.

[106] B. Choudhury, P. Chetri, and A. Choudhury, "Oxygen defects and formation of Ce^{3+} affecting the photocatalytic performance of CeO_2 nanoparticles," *RSC Adv.*, vol. 4, p. 4663, 2014.

[107] A. Kotani and Y. Toyozawa, "Photoelectron spectra of core electrons in metals with an incomplete shell," *J. Phys. Soc. Japan*, vol. 37, no. 4, pp. 912–919, Oct. 1974.

[108] T. Skála, F. Šutara, M. Škoda, K. C. Prince, and V. Matolín, "Palladium interaction with CeO_2 , Sn–Ce–O and Ga–Ce–O layers," *J. Phys. Condens. Matter*, vol. 21, no. 5, p. 55005, Feb. 2009.

[109] R. Hesse, T. Chassé, and R. Szargan, "Peak shape analysis of core level photoelectron spectra using UNIFIT for WINDOWS," *Fresenius. J. Anal. Chem.*, vol. 365, no. 1–3, pp. 48–54, Sep. 1999.

[110] D. Barreca, A. Gasparotto, C. Maccato, C. Maragno, and E. Tondello, "Cerium (III) Fluoride Thin Films by XPS," *Surf. Sci. Spectra*, vol. 13, no. 1, p. 87, 2006.

[111] Z. Wu, M. Li, J. Howe, H. M. Meyer, and S. H. Overbury, "Probing defect sites on CeO_2 nanocrystals with well-defined surface planes by raman spectroscopy and O_2 adsorption," *Langmuir*, vol. 26, no. 21, pp. 16595–16606, Nov. 2010.

[112] M. Kettner, K. Ševčíková, T. Duchoň, P. Kúš, Z. Rafaj, and V. Nehasil, "Morphology and CO Oxidation Reactions on Anion Doped CeOxFy/Rh(111) and CeOx/Rh(111) Inverse Catalysts," *J. Phys. Chem. C*, vol. 120, no. 47, pp. 26782–26792, Dec. 2016.

[113] D. R. Mullins, P. M. Albrecht, T.-L. Chen, F. C. Calaza, M. D. Biegalski, H. M. Christen, and S. H. Overbury, "Water Dissociation on CeO_2 (100) and CeO_2 (111) Thin Films," *J. Phys. Chem. C*, vol. 116, no. 36, pp. 19419–19428, 2012.

[114] H. Cordatos, T. Bunluesin, J. Stubenrauch, J. M. Vohs, and R. J. Gorte, "Effect of Ceria Structure on Oxygen Migration for Rh/Ceria Catalysts," *J. Phys. Chem.*, vol. 100, no. 2, pp. 785–789, 1996.

[115] Z. a. Feng, F. El Gabaly, X. Ye, Z.-X. Shen, and W. C. Chueh, "Fast vacancy-mediated oxygen ion incorporation across the ceria–gas electrochemical interface," *Nat Commun*, vol. 5, pp. 1–9, 2014.

[116] P. S. Lambrou, C. N. Costa, S. Y. Christou, and A. M. Efstathiou, "Dynamics of oxygen storage and release on commercial aged Pd-Rh three-way catalysts

and their characterization by transient experiments," *Appl. Catal. B Environ.*, vol. 54, no. 4, pp. 237–250, Dec. 2004.

[117] F. Esch, "Electron Localization Determines Defect Formation on Ceria Substrates," *Science*, vol. 309, no. 5735, pp. 752–755, 2005.

[118] H. Hirata, "Recent Research Progress in Automotive Exhaust Gas Purification Catalyst," *Catal. Surv. from Asia*, vol. 18, no. 4, pp. 128–133, 2014.

[119] E. Mamontov, T. Egami, R. Brezny, M. Koranne, and S. Tyagi, "Lattice Defects and Oxygen Storage Capacity of Nanocrystalline Ceria and Ceria-Zirconia," *J. Phys. Chem. B*, vol. 104, no. 47, pp. 11110–11116, Nov. 2000.

[120] J. Soria, A. Martínez-Arias, J. Coronado, and J. Conesa, "Chloride-induced modifications of the properties of rhodia/ceria catalysts," *Top. Catal.*, vol. 12, pp. 205–212, 2000.

[121] F. Fajardie, O. Tempere, J.-M. Manoli, G. Djega-Mariadassou, and G. Blanchard, "Ceria lattice oxygen ion substitution by Cl- during the reduction of Rh(Cl)/CeO_2 catalysts. Formation and stability of CeOCl," *J. Chem. Soc. Faraday Trans.*, vol. 94, no. 24, pp. 3727–3735, 1998.

[122] K. Ševčíková, T. Kolářová, T. Skála, N. Tsud, M. Václavů, Y. Lykhach, V. Matolín, and V. Nehasil, "Impact of Rh–CeOx interaction on CO oxidation mechanisms," *Appl. Surf. Sci.*, vol. 332, pp. 747–755, 2015.

[123] C. L. Perkins, M. A. Henderson, C. H. F. Peden, and G. S. Herman, "Self-diffusion in ceria," *J. Vac. Sci. Technol. A*, vol. 19, no. 4, pp. 1942–1946, 2001.

[124] V. Stetsovych, F. Pagliuca, F. Dvořák, T. Duchoň, M. Vorokhta, M. Aulická, J. Lachnitt, S. Schernich, I. Matolínová, K. Veltruská, T. Skála, D. Mazur, J. Mysliveček, J. Libuda, and V. Matolín, "Epitaxial cubic Ce_2O_3 films via Ce-CeO_2 interfacial reaction," *J. Phys. Chem. Lett.*, vol. 4, no. 1, pp. 866–871, 2013.

[125] J. W. Arblaster, "Crystallographic Properties of Rhodium," *Platium Met. Rev*, vol. 41, no. 4, pp. 184–189, 1997.

[126] S. Marchini, C. Sachs, and J. Wintterlin, "STM investigation of the (2 × 2)O and (2 × 1)O structures on Rh(1 1 1)," *Surf. Sci.*, vol. 592, no. 1–3, pp. 58–64, Nov. 2005.

[127] A. Migani, G. N. Vayssilov, S. T. Bromley, F. Illas, and K. M. Neyman, "Greatly facilitated oxygen vacancy formation in ceria nanocrystallites," *Chem. Commun.*, vol. 46, no. 32, p. 5936, 2010.

[128] R. S. Polizzotti and G. Ehrlich, "Chemisorption on perfect surfaces: Hydrogen and nitrogen on tungsten and rhodium," *J. Chem. Phys.*, vol. 71, no. 1, p. 259, 1979.

[129] F. Sadi, D. Duprez, F. Gérard, and A. Miloudi, "Hydrogen formation in the reaction of steam with Rh/CeO_2 catalysts: A tool for characterising reduced centres of ceria," *J. Catal.*, vol. 213, no. 2, pp. 226–234, Jan. 2003.

[130] K. T. Jacob, V. S. Saji, and Y. Waseda, "Lanthanum Oxyfluoride: Structure, Stability, and Ionic Conductivity," *Int. J. Appl. Ceram. Technol.*, vol. 3, no. 4, pp. 312–321, 2006.

[131] M. J. Wolf, J. Kullgren, P. Broqvist, and K. Hermansson, “Fluorine impurities at CeO_2(111): Effects on oxygen vacancy formation, molecular adsorption, and surface re-oxidation,” *J. Chem. Phys.*, vol. 146, no. 4, p. 44703, 2017.

[132] D. A. Andersson, S. I. Simak, N. V. Skorodumova, I. A. Abrikosov, and B. Johansson, “Optimization of ionic conductivity in doped ceria,” *Proc. Natl. Acad. Sci.*, vol. 103, no. 10, pp. 3518–3521, Mar. 2006.

[133] A. K. Lucid, P. R. L. Keating, J. P. Allen, and G. W. Watson, “Structure and Reducibility of CeO_2 Doped with Trivalent Cations,” *J. Phys. Chem. C*, vol. 120, no. 41, pp. 23430–23440, Oct. 2016.

[134] J. Wu, Y.-M. Wang, A. Drljevic, V. Rauniyar, R. J. Phipps, and F. D. Toste, “A combination of directing groups and chiral anion phase-transfer catalysis for enantioselective fluorination of alkenes,” *Proc. Natl. Acad. Sci.*, vol. 110, no. 34, pp. 13729–13733, Aug. 2013.

[135] R. J. Phipps, G. L. Hamilton, and F. D. Toste, “The progression of chiral anions from concepts to applications in asymmetric catalysis,” *Nat. Chem.*, vol. 4, no. 8, pp. 603–614, 2012.

[136] M. T. Greiner, M. G. Helander, W.-M. Tang, Z.-B. Wang, J. Qiu, and Z.-H. Lu, “Universal energy-level alignment of molecules on metal oxides,” *Nat. Mater.*, vol. 11, no. 1, pp. 76–81, 2012.

[137] L. Pauling, *The Nature of the Chemical Bond and the Structure of Molecules and Crystals: An Introduction to Modern Structural Chemistry*. Cornell University Press, 1960.

[138] E. P. O’Reilly, “Valence band engineering in strained-layer structures,” *Semicond. Sci. Technol.*, vol. 4, no. 3, pp. 121–137, 1999.

[139] S. M. Sze, “Physics of Semiconductor Devices,” *Electronics and Power*, vol. 16, no. 1. p. 811, 1969.

[140] F. E. Oropeza and R. G. Egdell, “Control of valence states in Rh-doped TiO_2 by Sb co-doping: A study by high resolution X-ray photoemission spectroscopy,” *Chem. Phys. Lett.*, vol. 515, no. 4–6, pp. 249–253, 2011.

[141] T. Montini, M. Melchionna, M. Monai, and P. Fornasiero, “Fundamentals and Catalytic Applications of CeO_2 -Based Materials,” *Chem. Rev.*, vol. 116, no. 10, pp. 5987–6041, May 2016.

[142] M. García-Melchor, L. Bellarosa, and N. López, “Unique Reaction Path in Heterogeneous Catalysis: The Concerted Semi-Hydrogenation of Propyne to Propene on CeO_2,” *ACS Catal.*, vol. 4, no. 11, pp. 4015–4020, Nov. 2014.

[143] G. Vilé, B. Bridier, J. Wichert, and J. Pérez-Ramírez, “Ceria in Hydrogenation Catalysis: High Selectivity in the Conversion of Alkynes to Olefins,” *Angew. Chemie Int. Ed.*, vol. 51, no. 34, pp. 8620–8623, Aug. 2012.

[144] R. Asahi, T. Morikawa, T. Ohwaki, and Y. Taga, “Visible-Light Photocatalysis in Nitrogen-Doped Titanium Oxides,” *Science*, vol. 293, no. 5528, pp. 269–271, 2001.

[145] S. Ahmad, K. Gopalaiah, S. N. Chandrudu, and R. Nagarajan, “Anion (Fluoride) -Doped Ceria Nanocrystals : Synthesis , Characterization , and Its Catalytic Application to Oxidative Coupling of Benzylamines,” *Inorg. Chem.*,

vol. 53, pp. 2030–2039, 2014.

[146] A. Popov and G. Knudson, “Preparation and Properties of tho Rare Earth Fluorides and Oxyfluorides,” *J. Am. Chem. Soc.*, vol. 76, no. 6, pp. 3921–3922, 1954.

[147] P. S. Bagus, C. J. Nelin, Y. Al-Salik, E. S. Ilton, and H. Idriss, “Multiplet splitting for the XPS of heavy elements: Dependence on oxidation state,” *Surf. Sci.*, vol. 643, pp. 142–149, 2016.

[148] G. E. Murgida and M. V. Ganduglia-Pirovano, “Evidence for subsurface ordering of oxygen vacancies on the reduced CeO_2(111) surface using density-functional and statistical calculations,” *Phys. Rev. Lett.*, vol. 110, no. 24, pp. 1–5, 2013.

[149] J. Paier, C. Penschke, and J. Sauer, “Oxygen defects and surface chemistry of ceria: Quantum chemical studies compared to experiment,” *Chem. Rev.*, vol. 113, no. 6, pp. 3949–3985, 2013.

[150] P. S. Bagus and C. J. Nelin, “Covalent interactions in oxides,” *J. Electron Spectros. Relat. Phenomena*, vol. 194, pp. 37–44, 2014.

[151] M. P. Casaletto, R. Zanoni, M. Carbone, M. N. Piancastelli, L. Aballe, K. Weiss, and K. Horn, “High-resolution photoemission study of ethanol on Si(100)2×1,” *Surf. Sci.*, vol. 447, no. 1, pp. 237–244, 2000.

[152] V. Matolín, J. Libra, M. Škoda, N. Tsud, K. C. Prince, and T. Skála, “Methanol adsorption on a CeO_2(1 1 1)/Cu(1 1 1) thin film model catalyst,” *Surf. Sci.*, vol. 603, no. 8, pp. 1087–1092, 2009.

[153] A. Neitzel, V. Johánek, Y. Lykhach, T. Skála, N. Tsud, M. Vorokhta, V. Matolín, and J. Libuda, “Reduction of Pt^{2+} species in model Pt–CeO_2 fuel cell catalysts upon reaction with methanol,” *Appl. Surf. Sci.*, vol. 387, pp. 674–681, Nov. 2016.

[154] J. Graciani, “Highly active copper-ceria and copper-ceria-titania catalysts for methanol synthesis from CO_2,” pp. 2–7, 2014.

[155] P. E. Blöchl, “Projector augmented-wave method,” *Phys. Rev. B*, vol. 50, no. 24, pp. 17953–17979, 1994.

[156] G. Kresse and J. Hafner, “Ab initio molecular dynamics for liquid metals,” *Phys. Rev. B*, vol. 47, no. 1, pp. 558–561, 1993.

[157] G. Kresse and J. Furthmüller, “Efficient iterative schemes for *ab initio* total-energy calculations using a plane-wave basis set,” *Phys. Rev. B*, vol. 54, no. 16, pp. 11169–11186, 1996.

[158] G. Kresse and D. Joubert, “From ultrasoft pseudopotentials to the projector augmented-wave method,” *Phys. Rev. B*, vol. 59, no. 3, pp. 1758–1775, 1999.

[159] A. V. Krukau, O. A. Vydrov, A. F. Izmaylov, and G. E. Scuseria, “Influence of the exchange screening parameter on the performance of screened hybrid functionals,” *J. Chem. Phys.*, vol. 125, no. 22, 2006.

[160] J. L. F. Da Silva, M. V. Ganduglia-Pirovano, J. Sauer, V. Bayer, and G. Kresse, “Hybrid functionals applied to rare-earth oxides: The example of ceria,” *Phys. Rev. B - Condens. Matter Mater. Phys.*, vol. 75, no. 4, pp. 19–24, 2007.

[161] J. D. Hunter, “Matplotlib: A 2D graphics environment,” *Comput. Sci. Eng.*, vol. 9, no. 3, pp. 99–104, 2007.

[162] Y. Jiang, J. B. Adams, and M. Van Schilfgaarde, “Density-functional calculation of CeO_2 surfaces and prediction of effects of oxygen partial pressure and temperature on stabilities,” *J. Chem. Phys.*, vol. 123, no. 6, 2005.

[163] S. Torbrügge, M. Cranney, and M. Reichling, “Morphology of step structures on CeO_2 (111),” *Appl. Phys. Lett.*, vol. 93, no. 7, pp. 10–13, 2008.

[164] T. Duchoň, F. Dvořák, M. Aulická, V. Stetsovych, M. Vorokhta, D. Mazur, K. Veltruská, T. Skála, J. Mysliveček, I. Matolínová, and V. Matolín, “Ordered Phases of Reduced Ceria As Epitaxial Films on Cu(111),” *J. Phys. Chem. C*, vol. 118, no. 1, pp. 357–365, Jan. 2014.

[165] D. Mullins, “Co Dissociation on Rh Deposited on Reduced Cerium Oxide Thin Films,” *J. Catal.*, vol. 188, no. 2, pp. 340–345, 1999.

[166] Y. Lykhach, A. Figueroba, M. F. Camellone, A. Neitzel, T. Skala, F. R. Negreiros, M. Vorokhta, N. Tsud, K. C. Prince, S. Fabris, K. M. Neyman, V. Matolin, and J. Libuda, “Reactivity of atomically dispersed Pt^{2+} species towards H_2: model Pt-CeO_2 fuel cell catalyst,” *Phys. Chem. Chem. Phys.*, vol. 18, no. 11, pp. 7672–7679, 2016.

[167] J. Höcker, T. Duchoň, K. Veltruská, V. Matolín, J. Falta, S. D. Senanayake, and J. I. Flege, “Controlling Heteroepitaxy by Oxygen Chemical Potential: Exclusive Growth of (100) Oriented Ceria Nanostructures on Cu(111),” *J. Phys. Chem. C*, vol. 120, no. 9, pp. 4895–4901, 2016.

[168] V. Perrichon, A. Laachir, G. Bergeret, R. Fréty, L. Tournayan, and O. Touret, “Reduction of cerias with different textures by hydrogen and their reoxidation by oxygen,” *J. Chem. Soc., Faraday Trans.*, vol. 90, no. 5, pp. 773–781, 1994.

[169] W. C. Conner and J. L. Falconer, “Spillover in Heterogeneous Catalysis,” *Chem. Rev.*, vol. 95, no. 3, pp. 759–788, 1995.

[170] S. M. F. Shahed, T. Hasegawa, Y. Sainoo, Y. Watanabe, N. Isomura, A. Beniya, H. Hirata, and T. Komeda, “STM and XPS study of CeO_2(111) reduction by atomic hydrogen,” *Surf. Sci.*, vol. 628, pp. 30–35, 2014.

List of Tables

List of Abbreviations

AFM – Atomic Force Microscopy
ARUPS – Angle Resolved Ultraviolet Photoelectron Spectroscopy
CAE – Constant Analyzer Energy
CRR – Constant Retard Ratio
EMSI – Electronic Metal Support Interaction
ESCA – Electron Spectroscopy for Chemical Analysis
FAT – Fixed Analyzer Transition
FRR – Fixed Retard Ratio
FWHM – Full Width at Half Maximum
IMFP – Inelastic Mean Free Path
L – Langmuir; a unit of exposure to gas (1 L = 1×10^{-6} Torr × s)
LEED – Low Energy Electron Diffraction
MB – Molecular Beams
MEBES – Micro Electron Bombardment Evaporation Source
ML – Monolayer
MLE – Monolayer Equivalent = Amount of deposited material, at which the LEED pattern from the substrate completely disappears and no CO adsorption or desorption from the substrate can be observed.
MSB – Material Science Beamline
NAP – Near-Ambient Pressure
NAP-XPS – Near-Ambient Pressure XPS - method or measuring system in Prague
NEXAFS – Near Edge X-ray Absorption Fine Structure
OSC – Oxygen Storage Capacity
PAW – Projector Augmented Wave
PBE – Perdrew-Burke-Ernzerhof
PDOS – Projected Densities of States
PEM – Proton Exchange membrane
PEMFC – Proton Exchange Membrane Fuel Cell
QMS – Quadrupole Mass Spectrometer
RPES – Resonant Photoelectron Spectroscopy
SRPES – Synchrotron Radiation Photoelectron Spectroscopy
TDS – Thermal Desorption Spectroscopy
TPD – Temperature Programmed Desorption
TPR - Temperature Programmed Reaction
TWC - Three-Way Catalysis
UHV – Ultrahigh Vacuum
VASP – Vienna Ab initio Simulation Package
XPD - X-ray Photoelectron Diffraction
XPS - X-ray Photoelectron Spectroscopy
XPS/TPR/LEED – Measuring system in Prague equipped with XPS, TPR and LEED methods.